Development and Function of Proprioceptive Dendrite Territories in *Drosophila* Larvae

Rebecca Danielle Vaadia

Submitted in partial fulfillment of the
requirements for the degree of
Doctor of Philosophy
under the Executive Committee
of the Graduate School of Arts and Sciences

COLUMBIA UNIVERSITY

2020

Abstract

Development and Function of Proprioceptive Dendrite Territories in *Drosophila* Larvae

Rebecca Danielle Vaadia

A neuron's function depends critically on the shape, size, and territory of its dendritic field. We have only recently begun to understand how diverse dendritic arbors are built and how the morphology and territory of these arbors support diverse neural functions. In this thesis, I use the *Drosophila* larval peripheral nervous system (PNS) as a model for studying these questions, as these neurons are very amenable to genetic manipulation and *in vivo* imaging.

First, I examined the relationship between dendritic fields and sensory activity in the proprioceptive neurons of the body wall. In collaboration with Elizabeth Hillman's lab, we used a high-speed volumetric microscopy technique, Swept Confocally Aligned Planar Excitation (SCAPE) microscopy, to simultaneously image the dendrite deformation dynamics and sensory activity of body wall neurons in crawling *Drosophila* larvae. We imaged a set of proprioceptive neurons with diverse dendrite morphologies and territories, revealing that each neuron subtype responds in sequence during crawling. These activities could conceivably provide a continuum of position encoding during locomotion. Activity timing is related to the dynamics of each neuron's dendritic arbors, suggesting arbor shape and targeting endow each proprioceptor with a specific role in monitoring body wall deformation. Furthermore, our results provide new insights into the body-wide activity dynamics of the proprioceptive system, which will inform models of sensory feedback during locomotion.

To investigate how dendritic arbors are built to support sensory function, I focused on proprioceptive (class I) and touch-sensing (class II-III) dendritic arborization (da) neurons. Proprioceptive and touch-sensing dendrite territories tend to target non-overlapping,

neighboring, areas of the body wall. How is territory coverage specified during development, and how does this coverage support a specific sensory function? Ablation studies indicate that repulsive interactions between heterotypic dendrites are not required for territory patterning. Instead, dendrite boundaries correlate with Anterior (A)-Posterior (P) compartment boundaries in the underlying epidermal substrate: proprioceptive class I dendrites target the P compartment, while touch-sensing dendrites tend to avoid that region. I found that genetic expansion of the P compartment leads to expansion of class I proprioceptive dendrites, suggesting compartmentalized epidermal cues instruct dendrite targeting. Furthermore, SCAPE imaging revealed that the P compartment coincides with a major body wall fold that occurs during crawling. These results support a model in which dendrite targeting by compartment cues reliably tunes neurons for predictable stimuli on the body wall: proprioceptive dendrites target areas that bend predictably during crawling, while touch-sensing dendrites could be avoiding those areas to be tuned for external mechanosensory stimuli.

To investigate the molecular identity of the substrate cues guiding the compartmental organization of dendrites, I tested candidate cues and sought new potential cues. I first tested cues that are known to be expressed in a compartmental fashion (Hedgehog and EGFR pathways). Interestingly, the overall dendrite territory footprint of class I proprioceptive cells is unaffected by known compartment cues. To reveal new candidates, I performed cell sorting and RNA sequencing. I identified 290 cell surface and secreted molecules with differential expression in the A and P compartments. I provide initial findings from a knockdown and misexpression screen testing the role of these candidates for class I and class III territory patterning. Taken together, these results provide new insights into how dendritic fields are patterned to support proper neural function.

Table of Contents

List of Figures and Tables

Acknowledgments

First and foremost, thank you to my research advisor, Wes Grueber. I couldn't have asked for a better advisor or lab environment for my PhD training. It's been a privilege to learn from such an exceptional scientist. I'm grateful for the many opportunities you've provided me to grow as both a scientist and communicator. From our many lab-wide practice talks and through collaborating on manuscript and grant writing, I've learned a tremendous amount about how to communicate science in a clear and engaging way. Finally, the good-natured and collaborative environment in the Grueber lab doesn't happen by accident and certainly comes from your leadership and example.

Thank you to the past and present members of the Grueber lab for all your support, scientifically and otherwise. Thank you to Grace, for your excellent example of how to be a creative, rigorous, and enthusiastic scientist, while also being a lovely and supportive human being. Thank you to the technicians of the Grueber lab who kept everything going over the years: Katie, Nate, Naureen, Taylor, and especially Rosa. Thank you to my elder students, Anita, Sam, and Sam for all of your advice and laughter, and your invaluable examples of how to have a successful and meaningful PhD. Thank you to Jenn, for your expertise at the beginning of my PhD and your pure enthusiasm for science. Rachel, it's been lovely to have you around the lab as I finish up. Thank you to Patricia and Shan—it was hard to see the older students leave, but your enthusiasm and talent for science and your good-natured and supportive presence made the transition much easier. Finally, thank you to the smart and dedicated undergrads who helped with my projects: Aisha Saleem, who investigated the function of proprioceptor subtypes, and Aomeng Cui, who helped with the knockdown screen of compartment cues.

Thank you to all the members of the Mann and Kohwi labs—our neighbors on the 9th floor of JLG. Natalia Molotkova, and Terry Hafer provided crucial training with the dissociation protocol, while Siqian Feng, Ryan Loker, and Judith Kribelbauer provided essential assistance with RNA-Sequencing. Clare has provided feedback throughout this project over teatime chats, and Davys, Gillie, and Tanguy have been an essential part of the 9th floor lunchtime crew.

Many people throughout Columbia have contributed to this project. Thank you to Elizabeth Hillman for a great collaboration and special thanks to her student Wenze Li for his work ethic and enthusiasm—Chapter 2 would not exist without them. I'm grateful to my thesis committee members, Ellen Lumpkin, Jane Dodd, and Richard Mann for their valuable time and feedback. Thanks also to Gary Struhl for his guidance on the compartment project. Thank you to Ira Schieren for his assistance with FAC sorting. Thank you to the co-directors of the NBB program: Darcey, Carol, and Ken, for their guidance in first-year and beyond. Thank you to Alla Kerzhner and Rozanna Yakub for their essential administrative help and for checking in on my progress. Finally, thank you to my wonderful NBB classmates for all their support and fun times over the years.

Importantly, thank you to my family and friends for all their moral support. Thank you to my partner Zach for his unwavering support and belief in me throughout the difficult years of my PhD, and for reminding me to think about things outside of science. Thank you to mom, Kim, and sister, Sara, for all of the love, dinners, laughs, and encouragement throughout my life. I am so happy to have worked on my PhD near my family. Finally, a special thank you to my late father Boaz, who passed away in year three of my PhD, for his effusive love and support throughout my life. I would not be where I am today without his example of a life led with curiosity, creativity, determination, and passion.

Chapter 1. Introduction

Neurons are polarized cells with a specialized axon and dendrites. Dendrites are complex structures that receive input from other neurons or from sensory stimuli. Across the diversity of neuronal types, dendritic fields vary considerably in their shape, size, territory, and branching pattern. Neural function depends critically on these features. In interneurons and motor neurons, the placement and density of dendrites determines the identity and number of presynaptic inputs (Lefebvre et al 2015). In sensory neurons, dendritic field size and density determines the size and sensitivity of the receptive field, and the placement of dendrites determines the sensory input that is sampled. To understand how a nervous system is built to support an animal's ability to feel, think, and move, it is essential to elucidate how different dendritic arbor morphologies are specified during development, and how these morphologies support diverse neural functions. This knowledge will also provide a basis for understanding how dendrite malformation in disease can lead to circuit dysfunction.

The majority of research on neurite patterning has focused on the axon (Kolodkin & Tessier-Lavigne 2011). Only relatively recently have we begun to understand how cell type-specific dendritic arbors are built. In this dissertation, I describe experiments performed with the *Drosophila* larva peripheral nervous system (PNS) to investigate 1) the relationship between dendritic arbor territories and neural function and 2) the developmental mechanisms that properly specify these arbors. In this chapter, I introduce the *Drosophila* larval PNS, with a special focus on the proprioceptive system. I also review the literature on mechanisms of tissue and dendrite pattering relevant to the current study.

The *Drosophila* larva peripheral nervous system

The *Drosophila* larva peripheral nervous system (PNS) is a useful model for studying the development and function of sensory neurons, including neuronal morphology. The anatomy of this system is very well characterized, and each sensory neuron can be uniquely identified by its morphology and position (Singhania & Grueber 2014). Because of the tools available in *Drosophila*, there are numerous cell-type specific markers, so PNS neurons are very amenable for genetic manipulation and in vivo imaging. Previous studies with this system have revealed important mechanisms of cell fate determination, dendritic field patterning, axon guidance, sensory function, and behavioral circuits (Kohsaka et al 2017, Ohyama et al 2015, Singhania & Grueber 2014).

The cell bodies of the larval PNS reside on the basal (inner) surface of the epidermis, and dendrites project along the body wall or to specific sensory end organs. The neurons are organized in a repeated pattern in each hemisegment of the larval body, with cells organized loosely into ventral (v), ventral prime (v ′), lateral (l), and dorsal (d) clusters (Fig. 1.1a-b) (Bodmer & Jan 1987b). The two major categories of cell types include type I neurons, which have single ciliated dendrites, and type II multidendritic (md) neurons. Mechanosensory type I neurons are associated with sensory end organs, including the external sensory (es) organs and the chordotonal (ch) organs. Md neurons have highly-branched dendrites that grow along the epidermis or on nearby internal structures. Md neurons show morphological diversity with three major subtypes: bipolar dendrite (bd) neurons, tracheal dendrite (td) neurons, and dendritic arborization (da) neurons. Td neuron dendrites grow along the trachea, and are potentially important for carbon dioxide sensing (Qian 2018, Qian et al 2018). Bd neurons have two

dendrite stalks that grow along internal connective tissues (Fig. 1.1c top) (Schrader & Merritt 2007). A similar md neuron, named dmd1, has a single dendrite bundle that projects to an internal nerve (Corty et al 2016). Da neurons show highly complex dendritic arbors that grow along the basal surface of the epidermis (Fig. 1.1c bottom). The name for each individual neuron within a hemisegment is depicted in Figure 1.1b. This name indicates the cell's location (e.g. v vs. d cluster), cell subtype (e.g da vs. bd), and includes an additional letter or number to give each neuron a unique identifier (Orgogozo & Grueber 2005).

Because of their morphological and functional diversity, bd and da neurons are the focus of this thesis. Da neurons can be characterized into four classes (classes I-IV) based on dendritic complexity and territory coverage (Fig. 1.2) (Grueber et al 2002). Class I (cI) neurons have the least complex arbors, class II (cII) neurons show intermediate arbor complexity, class III (cIII) dendrites are more complex with numerous short actin-containing protrusions, and class IV (cIV) neurons have large, complex space-filling arbors that innervate the entire epidermis. In contrast to cIV neurons, cI-cIII neuron body wall innervation is incomplete, with cI neurons showing the most selective territory coverage (Fig. 1.2b-e).

Suggesting distinct functions, each da neuron class shows a distinct axon projection pattern in the ventral nerve cord (VNC), which is analogous to the mammalian spinal cord (Grueber et al 2007). The dorsal neuropil of the VNC is associated with motor functions, while the ventral neuropil is associated with tactile responses. CI neurons project their axons to the dorsal neuropil, suggesting these neurons are proprioceptive. CII, cIII, and cIV axons project to three distinct layers of ventral neuropil, from lateral to medial, suggesting distinct mechanosensory functions.

Functional studies have confirmed that each class of da neuron is associated with a distinct sensory role. cIV neurons are multimodal sensors of noxious mechanical and temperature stimuli, and are essential for triggering escape behaviors (Hwang et al 2007). Calcium imaging and behavioral studies indicate that cIII neurons are touch-sensitive and are essential for behavioral responses to gentle touch (Tsubouchi et al 2012, Yan et al 2013). CII neurons also respond to touch, but their specific functional role is unknown (Tsubouchi et al 2012). Consistent with their axon projection patterns, cI neurons are involved in proprioceptive sensing, as suppression of these neurons leads to crawling defects (Hughes & Thomas 2007).

Bd neurons show a similar axon projection pattern and function to cI neurons. Like cI neurons, bd neurons project their axons to the dorsal neuropil (Corty et al 2016, Grueber et al 2007, Merritt & Whitington , Schrader & Merritt 2000). Furthermore, evidence indicates that bd neurons are proprioceptive: suppression of these neurons disrupts crawling (Hughes & Thomas 2007), and the dorsal bd neuron (dbd) shows electrophysiological responses to stretch (Suslak et al 2015).

The observed diversity in dendrite morphology, territory coverage, and function of md neurons provide a useful model for the study of the relationship between the form and function of dendritic fields.

Proprioceptive sensory feedback in *Drosophila* larvae

To explore the relationship between dendrite form and function, my studies initially focused on the proprioceptive system. Whether it is a running mammal, a swimming fish, or a crawling larva, coordinated movement requires continuous feedback from proprioceptive sensory systems to update the brain about position of body and limbs (Tuthill & Azim 2018). As

described above, cI and bd neurons have been characterized as important for larval proprioception based on their axon projections to dorsal neuropil regions and evidence from neuron silencing experiments (Hughes & Thomas 2007). Dmd1 also projects to the dorsal VNC neuropil, but its function hasn't been well studied. It is unknown if, how and when cI, bd, an dmd1 neurons are active during movement, and how their sensory function relates to their diverse dendrite morphologies.

The term proprioception was coined by Charles Sherrington, who was the first to demonstrate the influence of the sensory neurons of the muscles on posture and movement control (Burke 2007, Sherrington 1913). Nearly all animals that move require proprioceptive feedback to control their bodies (Tuthill & Azim 2018). In vertebrates, the two major proprioceptive organs are muscle spindles and Golgi tendon organs. Muscle spindles are located deep within muscles and contain specialized fibers targeted by sensory afferents that detect muscle length and contraction velocity. Golgi tendon organs reside at the interface between muscles and tendons and detect mechanical load: firing rates increase when muscle tension increases, such as during resisted movements (Proske & Gandevia 2012). Limbed insects, including adult *Drosophila,* have analogous proprioceptive organs to control their limbs: chordotonal neurons detect limb position and velocity while campaniform sensilla detect mechanical load [see (Tuthill & Azim 2018) for review].

As *Drosophila* larvae are soft bodied animals without limbs, their proprioceptors are associated with the body wall. Proprioceptive feedback is likely important for detecting a broad array of body motions but has been studied most extensively during crawling. Crawling involves a periodic motor pattern consisting of waves of segmental muscle contractions along the body (Heckscher et al 2012). Forward crawling involves waves from tail to head, while the backwards

crawling wave is reversed. Like most locomotor behaviors, crawling requires the coordination of neural circuits by central pattern generators (CPGs), which are microcircuits of excitatory and inhibitory neurons (Clark et al 2018). Without sensory feedback, the crawling CPG can still run but is severely distorted.

Silencing the entire PNS with UAS-Shibire^{ts}, a temperature-sensitive dynamin mutant that blocks neurotransmitter release at temperatures above 30 degrees Celsius (C°), causes wave progression to slow, with tight muscle contractions, leading to larval "toothpasting" (Hughes & Thomas 2007). Silencing only bd and cI da neurons is sufficient to produce this behavioral phenotype, while inhibiting es, chordotonal, or class II-IV neurons does not disrupt crawling, suggesting that bd and cI neurons provide essential sensory feedback during locomotion. The toothpasting phenotype suggests that bd and cI neurons might act as a "mission accomplished" signal, allowing for relaxation of one segment and propagation of contraction to the next segment to promote smooth locomotion. Dmd1 has not been well studied, but is also implicated in proprioceptive feedback based on its axon projections.

The diverse dendrite morphologies and positions of bd, cI, and dmd1 neurons suggest that each is likely to have distinct proprioceptive functions. However, it is unknown if and when these neurons are active during crawling, and how their sensory functions relate to their dendrite morphologies. Chapter 2 of this thesis, which is adapted from a published manuscript (Vaadia et al 2019), describes in vivo imaging experiments performed to address these questions. In collaboration with Elizabeth Hillman's lab and her student Wenzi Li, I used Swept-Confocally Aligned Planar Excitation (SCAPE) microscopy, a recently-developed high-speed volumetric imaging technique (Bouchard et al 2015, Hillman et al 2018, Voleti et al 2019), to monitor the

activity patterns of proprioceptive cells in freely moving animals, and how neuron activity relates to the dendrite distortion that occurs during crawling.

Revealing the body-wide neuronal dynamics of the proprioceptive system will inform models of sensory feedback during locomotion. Recently, a nearly complete reconstruction of the larval central nervous system (CNS) has been performed using serial section transmission electron microscopy (TEM) (Eichler et al 2017, Schneider-Mizell et al 2016), revealing a map of connections between sensory inputs, interneurons, and motor outputs. Furthermore, recent functional studies have revealed roles for different subsets of interneurons in controlling patterned intrasegmental and intersegmental motor activity of the crawling CPG [Reviewed in (Clark et al 2018)]. For example, Period-Positive Median Segmental Interneurons (PMSIs) promote segment relaxation and anterior wave propagation (Kohsaka et al 2014), while A27h interneurons act through GDL interneurons to inhibit contraction in neighboring anterior segments, thereby preventing premature wave propagation (Fushiki et al 2016). Our imaging of sensory activity dynamics will inform models of how sensory activity feeds into these mapped circuits.

Mechanisms of dendritic territory patterning

Dendritic field shape and location determines the input that a neuron samples. How do neurons develop their distinct dendrite morphologies to support proper sensory or neural function? A complex combination of intrinsic and extrinsic mechanisms pattern dendritic field size and shape and guide fields to the appropriate location (Lefebvre et al 2015). These mechanisms include intrinsic transcription factor expression, extrinsic guidance factors and substrate interactions, and dendrite-dendrite interactions.

Intrinsic mechanisms

Intrinsic genetic pathways that determine a neuron's cell fate can also regulate the size, shape, and targeting of its dendritic arbor. Transcription factors (TFs) activate target genes that modulate the cell's propensity for dendrite branching and affect expression of receptors that determine responsiveness to extrinsic cues. The role of cell-intrinsic pathways in regulating dendritic arbors has been best studied in *Drosophila* larval da neurons, as each of the four classes show different propensities for dendrite branching (Fig. 1.2). Simple class I neurons express the BTB zinc finger TF Abrupt, which is essential for limiting their dendritic branching (Sugimura et al 2004), while highly-branched class IV neurons express the TF Knot, which is required for their complex arbors (Jinushi-Nakao et al 2007).

The homeobox TF Cut is expressed at different levels in each da neuron class and is important for regulating cell-type specific dendritic morphology (Grueber et al 2003a). Class I neurons show no Cut expression, while Cut shows increasing levels of expression in class II, class IV, and class III neurons. High Cut expression is essential for the actin-rich dendritic spikes characteristic of cIII neurons, while overexpressing Cut is sufficient to cause overbranching and production of dendritic spikes in other classes. Similarly, the mouse homologs of Cut, Cux1/2, are also important for regulating dendrite arbor morphology. These TFs promote the branching of upper layer cortical dendrites, but not axons (Cubelos et al 2010).

Dendrite-dendrite repulsion for self-avoidance and tiling

Self-avoidance

Drosophila larval da neurons have also been a very useful model for revealing the importance of dendrite-dendrite interactions for territory patterning (Grueber & Sagasti 2010). Dendrite-dendrite interactions mediate dendritic self-avoidance, which refers to the tendency of

branches from the same dendritic arbor avoid overlap. Self-avoidance is an efficient strategy for non-redundant coverage of a receptive field from an individual cell. In order to properly self-avoid, dendrites must be able to recognize "self" from "non-self" dendrites. Self-recognition relies on Down syndrome cell adhesion molecule 1 (Dscam1), an immunoglobulin superfamily adhesion molecule with tens of thousands of isoforms generated by alternative splicing (Hughes et al 2007, Matthews et al 2007, Soba et al 2007). Dscam1 mediates repulsion upon homophilic binding between sister dendrites. If Dscam1 expression is lost, da dendrites no longer self-avoid and collapse on one another. Single isoforms can rescue full self-avoidance capacity. If the same Dscam1 splice isoform is ectopically expressed in neighboring neurons, their dendrites show ectopic heteroneuronal avoidance (Matthews et al 2007). Splicing is controlled probabilistically, so that each neuron expresses a different combination of Dscam1 splice isoforms from that of its neighbor (Miura et al 2013), thus allowing individual neurons to properly distinguish self from non-self.

In vertebrates, *Dscam1* does not show the same diversity of splice isoforms. Instead, a cluster of *protocadherin* (*Pcdh*) genes, which encode many different isoforms of cadherin superfamily adhesion molecules, have an analogous role to *Dscam1*. These Protocadherins mediate self-avoidance of starburst amacrine cells and cerebellar Purkinje cells in mice through utilizing the same strategy for self-recognition and repulsion of sister dendrites [Reviewed in (Dong et al 2015, Lefebvre et al 2015)].

Tiling

Some dendrites don't just avoid iso-neuronal ("self") dendrites, but also avoid dendrites from neighboring neurons of the same functional type. This organization, which is termed tiling, is an efficient strategy for arbors of a specific sensory modality to sample the entire sensory

space without redundancy. Tiling of dendrite or axon arbors is seen in a wide range of systems from class III-IV *Drosophila* larval da neurons, to mammalian retinal ganglion cells (RGC) and the somatosensory axon arbors of larval zebrafish (Grueber & Sagasti 2010) and mice (Kuehn et al 2019). Work in class IV da neurons indicates that tiling requires repulsive interactions between neighboring homotypic dendrites (Grueber et al 2003b). Ablation of cIV neurons during development leads to invasion of neighboring cIV dendrites into the ablated cell's usual territory, and specification of supernumerary neurons decreases the field coverage of neighboring cIV cells. Similarly, the axons arbors of somatosensory neurons that innervate the epidermis in zebra fish will grow until they encounter a like-type neighbor, while mammalian RGCs use a combination of repulsive interactions between neighboring dendrites and intrinsic determinants of arbor size (Grueber & Sagasti 2010).

The repulsive cell-surface molecules responsible for contact-mediated homotypic tiling have not yet been discovered. Some molecular pathways do affect proper tiling of cIV neurons, such as a kinase cascade including *Hippo*, *Tricornered* (*TRC*), and *Furry* (*FRY*), and integrin-laminin interactions. However, these genes have been found to affect the relationship between dendrites and the epidermal substrate, so that dendrites are no longer residing in the same 2D plane and contacted-mediated repulsion is less frequent (Dong et al 2015, Grueber & Sagasti 2010). The importance of integrin receptors for tiling and self-avoidance is explained in more detail in the following section on the role of dendrite-substrate interactions.

Role of dendrite-substrate interactions

Role of dendrite-ECM attachment

Interactions between dendrites and their substrates are essential for patterning the size, shape, and location of dendrite territories. *Drosophila* larval da dendrites arborize between the

basal surface of the epidermis and the extracellular matrix (ECM). Integrin receptors are required on the surface of da dendrites to maintain attachment to the ECM by interacting with laminin (Han et al 2012, Kim et al 2012). When integrins are lost, dendrites are more likely to be ensheathed within the epidermal cell. Since dendrites are no longer in a 2D plane, contact-mediated repulsion is decreased, leading to non-contacting crossings of sister-dendrites and defects in tiling and self-avoidance. Integrin expression is also essential for the maintenance of newly grown branches (Kim et al 2012). The epidermis-derived secreted ligand Semaphorin (Sema)-2b is also important for regulating dendrite adhesion to the ECM to maintain a 2D field for proper self-avoidance (Meltzer et al 2016). Sema-2b binds to the Plexin B receptor in neurons, and this complex interacts with integrins to regulate adhesion.

While most da dendrites contact the ECM, a subset of dendrites are normally ensheathed within the epidermis in wild type larvae. Dendrite enclosure is most commonly seen in complex cIV arbors, and rarely seen in simpler cI neurons. Recent studies have revealed that enclosure is not merely due to the loss of ECM attachment, but also an active process regulated by the epidermal expression of Coracle (Cora), Neuroglian (Nrg), and Phosphatidylinositol 4,5-bisphosphate (PIP2) (Jiang et al 2019, Tenenbaum et al 2017, Yang et al 2019). The knockdown of the septate junction protein Cora in the epidermis leads to less enclosure of dendrites. Furthermore, Cora knockdowns show decreased cI arbor growth, suggesting proper levels of cell-type specific dendrite enclosure helps different classes of neurons share a field (Tenenbaum et al 2017). Epidermal PIP2 is required for the initiation of neurite enclosure in both fly and zebrafish somatosensory neurons, and blocking enclosure reduced the sensitivity of cIV nociceptive neurons (Jiang et al 2019). Neuroglian isoform 167 (Nrg167) is expressed in the epidermis, while isoform 180 (Nrg180) is expressed on dendrite surfaces. Interactions between

these isoforms promote dendrite enclosure, and furthermore prevent dendrites from bundling via adhesive Nrg180-Nrg180 interactions (Yang et al 2019).

Dendrite-substrate interactions regulating dendritic field size and branch pattern

Dendrite-substrate interactions are also important for regulating proper arbor size. Well-studied neurotrophins are secreted growth factors that have been shown to affect arbor size. These cues often work retrogradely from the target tissue in sensory or motor neurons [reviewed in (da Silva & Wang 2011)], but have also been shown to work anterogradely from afferents to regulate Purkinje cell arbor size in the mouse cerebellum [Reviewed in (Ledda & Paratcha 2017)].

In *Drosophila* larvae, dendrite-substrate interactions in da neurons are important for the proper scaling of arbors as an animal grows. Class IV dendrites establish receptive field coverage during embryogenesis, and then dendrites grow in proportion with the epidermal substrate throughout larval stages. Proper scaling of dendrite arbors requires the miRNA *bantam* within the epidermal substrate but not within neurons (Parrish et al 2009). In another set of experiments, time-lapse live imaging revealed that signals from heparan sulfate proteoglycans (HSPGs) on epidermal cells are required for cIV dendrites to grow and maintain their space-filling arbors, via stabilizing microtubules of the dynamic high-order dendrite branches of these cells (Poe et al 2017). This signaling is cell-type specific, as the non-space filling arbors of cI-cIII neurons do not require this signaling.

Dendrite-substrate interactions can also be also important for guiding the branching pattern of dendrites. In *Drosophila* larvae, Teneurin-m (Ten-m) is a homophilic adhesion molecule expressed in a gradient within the epidermis. Selector genes *knot* and *abrupt* dictate different levels of Ten-m in cIV versus cI neurons respectively. The high levels of Ten-m in cI

cells help guide directional comb-like dendrites, while lower levels in cIV neurons allow for radial, space-filling growth of dendrites (Hattori et al 2013). In *C. elegans,* the PVD somatosensory neuron shows a highly stereotyped branch pattern along the body wall, and this pattern is guided by localized cues in the skin. Dendrite growth and branch points are determined by the precise expression of skin-derived cell adhesion molecules, SAX-7 (an L1-CAM homolog) and MNR-1 (a Fam151 homolog), detected by DMA-1 receptors (LRR-containing transmembrane proteins) on the neuron (Dong et al 2013, Salzberg et al 2013).

Repulsive cues from the substrate are also important for restricting sensory dendrite territories on the adult *Drosophila* body wall (Yasunaga et al 2015). Adult cIV da neurons cover most of the body wall, but avoid the ventral-most section of the abdominal epidermis. This avoidance is due to the expression of Wnt5, a well-conserved secreted patterning molecule, from the underlying substrate, which regulates dendrite growth through the Ryk receptor family kinase Derailed (Drl).

Dendritic field targeting by guidance cues and presynaptic partners

Dendrite targeting to the proper location is essential for determining proper neural connectivity and function. This importance is highlighted in a study of the *Drosophila* larvae motor system, which showed that minor shifts in dendritic field targeting can change the number of synapses received from different pre-motor neurons (Couton et al 2015). Therefore, precise dendritic location may be essential for determining a functional unit of premotor interneurons, motor neurons, and muscle target.

Classic studies have revealed long range cues that guide neurites, such as Slits, Netrins, Semaphorins, and ephrins (Kolodkin & Tessier-Lavigne 2011). While these cues have been studied extensively in the context of axon guidance, many of these cues are also important for

guiding dendrite orientation, growth, and the precise location of branch elaboration and targeting (Dong et al 2015). Sema-3a has been shown to attract cortical pyramidal neuron apical dendrites to the pial surface, while also repelling the axon (Polleux et al 2000). Further growth and branching are promoted by local Slit and neurotrophins (reviewed in (Ledda & Paratcha 2017)).

In *Drosophila* larvae, motor dendrites are organized in a myotopic map, and the formation of one axis of this map is due to a combination of repulsive Slit/Robo and attractive Netrin/Frazzled signaling from the VNC midline (Mauss et al 2009). Dendrites from motor neuron (MN) subtypes that project to more ventral muscles are targeted medially towards the midline due to higher Frazzled signaling, while dendrites from MNs that project to more dorsal muscles are targeted more laterally due to higher Robo signaling. Changing the proportion of Robo and Frazzled receptors is sufficient to convert dendrite field targeting to that of a different MN cell type. Netrin/Frazzled signaling is also important for attracting dorsal cIII da dendrites for correct territory coverage of the body wall (Matthews & Grueber 2011).

Semaphorins are important for the targeting of projection neuron (PN) dendrites in the *Drosophila* adult olfactory system [reviewed in (Dong et al 2015)]. In the antennal lobe, PN neuron dendrites must be targeted to the correct glomerulus to match up with the appropriate class of incoming olfactory rector neuron (ORN). Gradients of secreted Sema-2a and Sema-2b define the lobe's dorsolateral-ventromedial axis to guide individual classes of PNs, which express distinct levels of transmembrane Sema-1a. Dendrites with high levels of Sema-1a are targeted to areas with low Sema-2a/2b expression and vice versa. Selective adhesion between like-type PN dendrites, mediated by Leucine-Rich Repeat (LRR)-containing membrane receptors Capricious and Tartan, further sorts these arbors to the correct glomeruli.

Similarly, in mammals, repulsive Semaphorin-Plexin signaling is important for restricting the dendrites of retinal cells to the appropriate lamina of the Inner Plexiform Layer (IPL) (Reviewed in (Dong et al 2015, Lefebvre et al 2015)). ON cells, which respond to light increments, and OFF cells, which respond to light decrements, must target different layers of the IPL for appropriate function. Amacrine cells that target the OFF layer express Plexin receptors to restrict their dendrites from the ON layer, which expresses Sema-6a (Matsuoka et al 2011, Sun et al 2013).

Some dendritic fields are further refined and targeted by matching with a presynaptic partner via transmembrane adhesion molecules with specific binding interactions. For example, in the PNs of the *Drosophila* adult olfactory system, two different homophilic adhesion molecules, Ten-a and Ten-m, are expressed in complementary areas of the antennal lobe, and PN dendrites connect with ORN afferents that express the same Teneurin. This organization is disrupted with loss of Ten-a or Ten-m (Hong et al 2012).

The above evidence implicates extrinsic cell surface and secreted (CSS) proteins, such as secreted guidance cues or cell surface adhesion molecules, as important for targeting dendrites in a wide variety of systems. Therefore, we predict that CSS molecules in the epidermal substrate may have a role in the targeting of larval sensory dendrite territories to the appropriate areas of the body wall.

Compartment organization of dendrites

In *Drosophila* larvae, dendrites from some neuron types have been found to be targeted to specific, molecularly defined, compartments. Larval MN dendrites from different subtypes are targeted to non-overlapping areas of the neuropil to form a central myotopic map of body wall muscle position (Landgraf et al 2003). Dendrites of MNs that project to internal muscles arborize

within the *engrailed (en)* domain of the neuropil, while dendrites of MNs that project to external muscles avoid this region. Expression of the En transcription factor is important for subdividing each segment of the body wall and CNS into a posterior compartment, defined by En expression, and an anterior compartment that lacks En expression (Bhat 1999, Sanson 2001). However, known secreted effectors of this compartment patterning (e.g. Hedgehog, discussed in detail in the following section) were not found to be essential for proper MN dendrite targeting (Landgraf et al 2003). Furthermore, compartmental organization of MN dendrites does not require repulsive interactions between neighboring dendrites and is maintained without the presence of target muscles. Therefore, the molecular mechanism underlying this organization of dendrites is unknown, and likely represents a robust strategy for ensuring proper targeting of a system that is essential for hatching and survival.

In Chapter 3 of this thesis, I describe a similar compartmental organization of sensory dendrites on the body wall: proprioceptive class I da neurons target the *engrailed* domain, while touch-sensing cII-cIII da neurons tend to avoid this region. In Chapter 3-4, I describe experiments performed to test the molecular mechanisms and functional importance of this compartmental organization.

Compartments and nervous system development

Mechanisms of compartment specification

During early patterning, many tissues are subdivided into lineage-restricted compartments, a process that has been well studied in *Drosophila* imaginal discs and the embryonic body wall [reviewed in (DiNardo et al 1994, Lawrence & Struhl 1996, Payre 2004, Sanson 2001)]. Compartment boundaries prevent the mixing of cells fated for different

structures, and provide positional information to neighboring cell populations via a signaling center, as described in more detail below (Kiecker & Lumsden 2005).

In the *Drosophila* embryo, a cascade of maternal morphogen gradients, gap genes, and pair rule genes define successively smaller subdivisions of the embryo. Pair rule genes lead to expression of segment polarity genes (*engrailed*, *wingless*), dividing each segment of the embryo into an Anterior (A) and Posterior (P) compartment (Fig. 1.3). The P compartment is defined by the expression of the Engrailed (En) transcription factor. The morphogen Hedgehog (Hh) is secreted from Engrailed-expressing cells. Hh binds the Patched (Ptc) receptor, expressed in a narrow domain of the A compartment just near the A-P compartment boundary, which leads to the secretion of Wingless (Wg) protein (Fig. 1.3b). In stage 9-10 embryos, Wg maintains En/Hh expression and Hh maintains Wg expression in a positive feedback loop to stabilize the A-P compartment boundary. By the end of stage 10, En expression is independent of Wg signaling, and the morphogen gradients are used for further patterning of epidermal cells within a segment. En expression is maintained in the P compartment of the epidermis throughout larval stages (Fig. 1.3a).

Similar compartments are formed during the development of vertebrate tissues, including the limb bud and hindbrain (Blair 1997, Kiecker & Lumsden 2005). While the exact molecules vary, evidence suggests that compartments across animals and tissues are patterned by a similar mechanism of selector genes and interacting morphogens as outlined for the *Drosophila* embryonic body wall (Kiecker & Lumsden 2005, Lawrence & Struhl 1996).

Role of compartments and patterning genes for nervous system development

Compartments have an important role in nervous system patterning. Similar to the *Drosophila* embryonic body wall, the *Drosophila* CNS is also organized into P and A

compartments via segment polarity genes (e.g. *engrailed/hedgehog, wingless*) (Bhat 1999). Loss of function of these genes can lead to the failure to form certain neuroblasts or aberrant specification of neuroblast identity. Similarly, in vertebrates, the hindbrain is segmented into seven lineage-restricted compartments along the AP axis, known as a rhombomeres, which express specific molecular markers (Kiecker & Lumsden 2005). While *engrailed* is not involved in the segmented organization of this brain region, Wnt signaling (vertebrate homolog of Wg) plays a role in hindbrain segmentation in zebrafish (Riley et al 2004). Additionally, Hox genes are important for patterning both the vertebrate hindbrain and the *Drosophila* embryo body plan, further exemplifying the similarities between the two structures (Kiecker & Lumsden 2005).

Engrailed is a highly-conserved homeodomain TF and is important in the vertebrate nervous system for patterning, neurogenesis, and axon guidance [reviewed in (Prochiantz & Di Nardo 2015)]. Opposing domains of En and Pax6 expression define the Diencephalic–midbrain boundary (DMB) [reviewed in (Kiecker & Lumsden 2005)]. In mice, Engrailed-1 (En-1) is also expressed in one large stripe at the midbrain-hindbrain boundary and is considered a developmental gap gene, as a null mutation of *en-1* leads to the loss of mid-hindbrain tissues (Wurst et al 1994). Furthermore, maintenance of En-1 expression in this region relies on Wnt-1(Danielian & McMahon 1996), similar to how Wg-signaling maintains En expression in *Drosophila* embryo segmentation. In the chick and frog visual system, graded expression of En-1 and En-2 regulates the transcription of the guidance cue EphrinA5 to form a gradient along the AP axis of tectum, directing the appropriate guidance of retinal cell axons [reviewed in (Prochiantz & Di Nardo 2015)]. Interestingly, evidence suggests that En also regulates axon guidance in the tectum via transcription-independent mechanisms. En can cross plasma membranes and bind to cytoplasmic receptors to regulate protein translation in growing axons.

Blocking extracellular En1/2 disrupts axon targeting in vivo, and in vitro assays show that En1/2 is sufficient to affect axon guidance (Brunet et al 2005, Wizenmann et al 2009).

Other patterning molecules, including Hedgehog or Wnt family proteins, also participate in aspects of neural circuit assembly in both invertebrates and vertebrates [reviewed in (Salie et al 2005)]. For example, Sonic Hedgehog (Shh, vertebrate homolog of Hh) and Wnt are both important for axon guidance in the developing vertebrate spinal cord. Wnts also control dendrite morphogenesis [reviewed in (Salinas & Zou 2008)], including in adult *Drosophila* sensory neurons of the body wall, as described above (Yasunaga et al 2015).

Since compartment specification by segment polarity genes is important for both body wall and nervous system patterning in *Drosophila,* an appealing model is one in which these molecular pathways are used to coordinate the patterning of the body wall, PNS, and CNS. However, not much is known about if and how compartment cues regulate neurite targeting to specific regions of the body wall or CNS. In Chapters 3-4 of this thesis, I describe experiments performed to test the molecular mechanisms underlying the compartmental organization of sensory dendrites on the body wall. Mechanisms of compartment organization in *Drosophila* could be relevant to a wide range of systems for linking the nervous system patterning with the body plan.

Overview of aims

In this thesis work, I examine the relationship of dendritic arbor shape and territory to sensory function, and I investigate the developmental mechanisms that properly specify these arbors. In the following chapters, I describe work to:

1. Characterize the relationship between proprioceptive arbor morphology/territory and sensory activity, using high-speed volumetric imaging of freely crawling animals (Chapter 2)
2. Investigate the patterning mechanisms and functional role of proprioceptive and touch-sensing dendrite territory boundaries, which correlate with compartment boundaries (Chapter 3)
3. Identify potential substrate cues and provide initial insights into their role in regulating this compartmental organization of sensory dendrites (Chapter 4)

Chapter 1 Figures

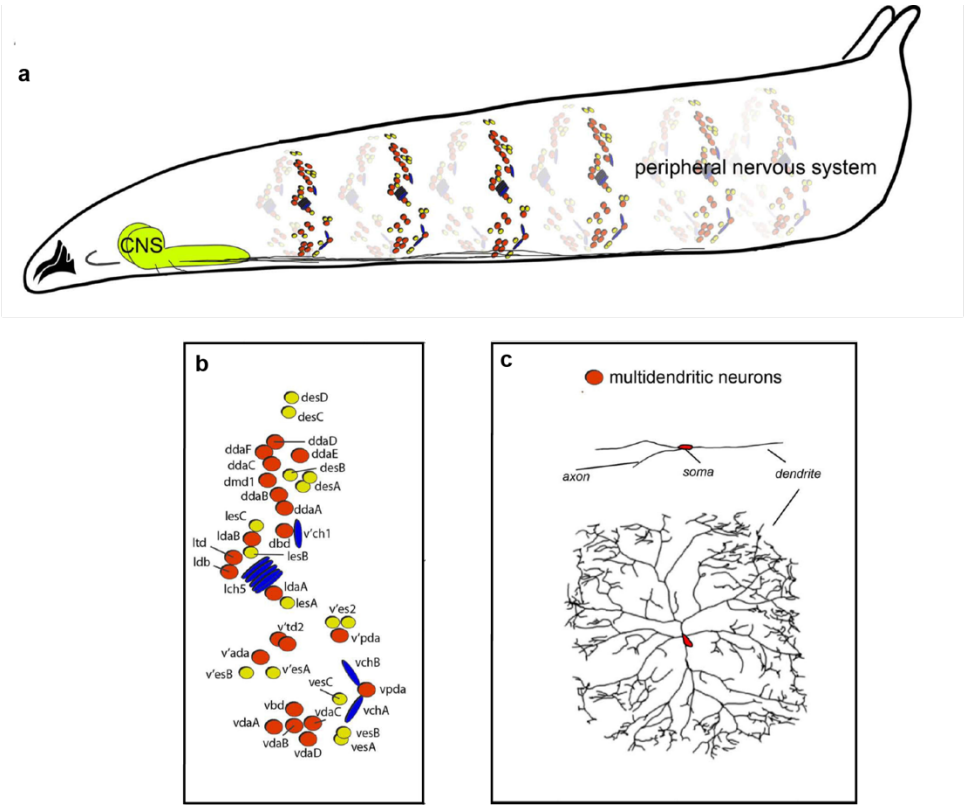

Figure 1.1. The peripheral nervous system (PNS) of the *Drosophila* larva
Figure is adapted from (Singhania and Grueber, 2014) with permission
(a) Schematic of nervous system of the *Drosophila* larva. The neurons of the PNS form a stereotyped organization and are repeated in each hemisegment of the animal (blue, red, yellow). Axons from the PNS project up to the Central Nervous System (CNS, green). Anterior is to the left, dorsal is to the top.
(b) Schematic of one hemisegment of the PNS. Each neuron is uniquely identified by its position and morphology, with an accompanying unique identifier. Yellow circles represent external sensory (es) neurons, blue ovals represent chordotonal (ch) neurons, and red circles represent multidendritic (md) neurons. Anterior is to the left, dorsal is to the top.
(c) Close up schematic of two different types of multidendritic neurons. Bipolar dendrite neuron (top) and dendritic arborization neuron (bottom).

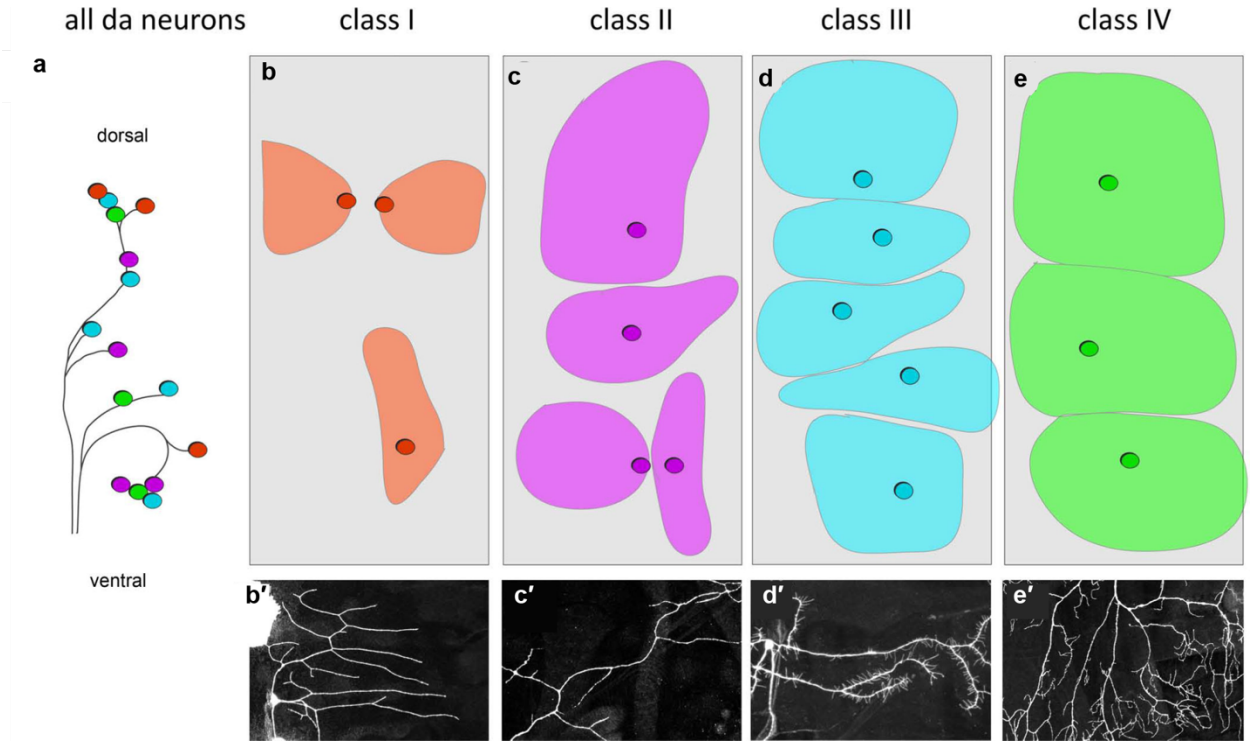

Figure 1.2. Dendritic arborization neurons can be subdivided into four distinct classes (class I-IV) based on dendritic arbor morphology and territory coverage
Figure is adapted from (Singhania and Grueber, 2014) with permission
(a) Schematic of locations of dendritic arborization (da) neurons within one hemisegment. Class I=red, class II=purple, class III=blue, and class IV=green.
(b-e) Schematic of dendritic territory coverage within a hemisegment for each class of da neuron. Class I dendrites show the sparsest coverage, while class IV dendrites tile the entire body wall
(b′-e′) Confocal image showing the dendrite morphology of each neuron class. Class I (b′) show the simplest arbors, class II (c′) show increased arbor complexity, class III (d′) dendrites are more complex with dendritic spikes, and class IV (d′) dendrites show very complex space-filing arbors.

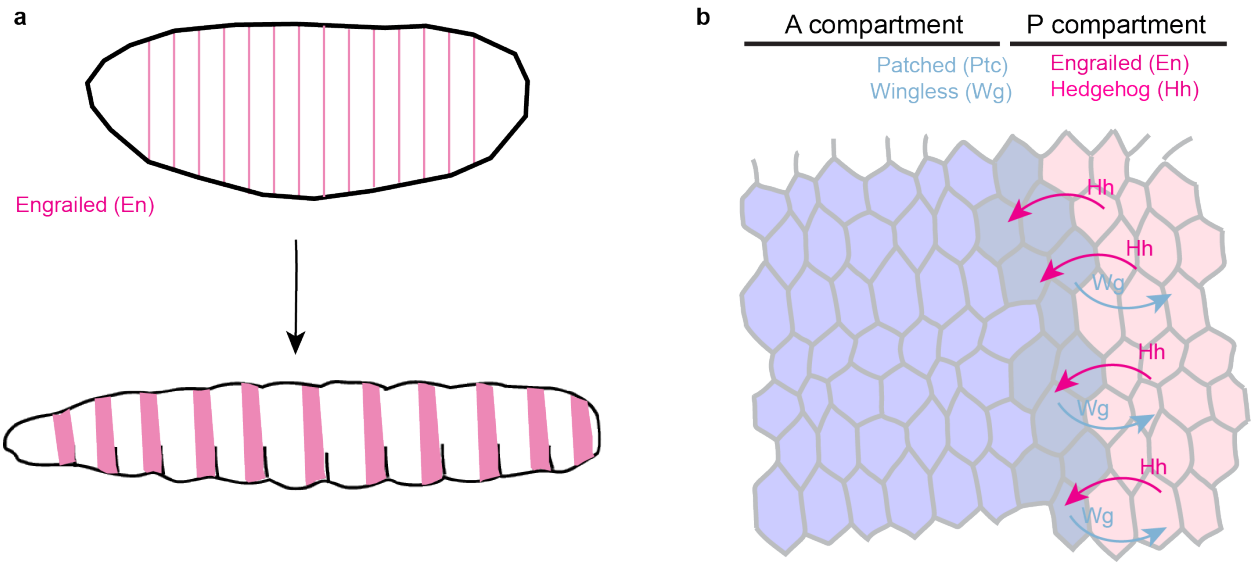

Figure 1.3. Each body wall segment is specified into an Anterior (A) and Posterior (P) compartment
(a) The transcription factor Engrailed (En) specifies the Posterior (P) compartment of each body wall segment starting in early embryogenesis. Engrailed expression is maintained throughout larval stages.
(b) Schematic showing the molecular pathways that set up the Anterior-Posterior compartment boundary at embryonic stage 9-10. Engrailed cells secrete Hedgehog, which binds to the Patched receptor expressed in a small stripe of the A compartment (darker blue). This domain then secretes Wingless, which in turn promotes Hedgehog release, working in a positive feedback loop to maintain the compartment boundary. Engrailed/Hedgehog expression become independent of Wingless at later stages.

Chapter 2. Characterization of proprioceptive system dynamics in behaving *Drosophila* larvae using high-speed volumetric microscopy

This chapter is adapted from a published manuscript (Vaadia et al 2019). I am grateful to many collaborators for their valuable contributions to the data and text of this chapter. This chapter is the result of a close collaboration with Elizabeth Hillman's lab. Wenze Li, Venkatakaushik Voleti, and Elizabeth Hillman optimized the SCAPE system for larval imaging. All larval SCAPE imaging was performed in close collaboration with Wenze Li. Wenze Li developed the image processing software and the analysis software for larval crawling. Elizabeth Hillman developed the analysis for larval head turning/retraction.

Summary

Proprioceptors provide feedback about body position that is essential for coordinated movement. Proprioceptive sensing of the position of rigid joints has been described in detail in several systems, however it is not known how animals with an elastic skeleton encode their body positions. Understanding how diverse larval body positions are dynamically encoded requires knowledge of proprioceptor activity patterns *in vivo* during natural movement. Here we used high-speed volumetric SCAPE microscopy in crawling *Drosophila* larvae, to simultaneously track the position, deformation, and intracellular calcium activity of their multidendritic proprioceptors. Most proprioceptive neurons were found to activate during segment contraction although one subtype was activated by extension. During cycles of segment contraction and extension, different proprioceptor types exhibited sequential activity, providing a continuum of position encoding during all phases of crawling. This sequential activity was related to the dynamics of each neuron's terminal processes, and could endow each proprioceptor with a specific role in monitoring different aspects of body wall deformation. We demonstrate this deformation encoding both during progression of contraction waves during locomotion, as well as during less stereotyped, asymmetric exploration behavior. Our results provide powerful new insights into the body-wide neuronal dynamics of the proprioceptive system in crawling

Drosophila, and demonstrate the utility of our SCAPE microscopy approach for characterization of neural encoding throughout the nervous system of a freely behaving animal.

Introduction

Monitoring neural activity in freely behaving animals is a key step towards understanding how sensory activity is transformed into action (Alivisatos et al , Calhoun & Murthy , Kerr & Nimmerjahn). Small invertebrate model systems with well-described sensory systems and complete or near-complete connectomes, such as *C. elegans* and *Drosophila* larvae, are ideal systems in which to uncover fundamental principles of sensorimotor integration. Light sheet, confocal, and two-photon microscopy can capture neuronal calcium activity in isolated *Drosophila* brains or immobilized preparations (Chhetri et al 2015, Ghannad-Rezaie et al 2012, Lemon et al 2015, Pulver et al 2015, Royer et al 2016). However, these methods have been unable to provide volumetric imaging at sufficient speeds, in unrestrained samples, to enable extended imaging of body-wide neural activity in behaving animals.

Multi-spectral, high-speed, volumetric Swept Confocally Aligned Planar Excitation (SCAPE) microscopy is capable of characterizing tissue and cellular dynamics in live behaving animals (Bouchard et al 2015, Hillman et al 2018). We have applied this imaging technology to characterize the dynamics of multidendritic (md) neuron activity in crawling *Drosophila* larvae. Multifunctional md neurons are located just under the larval body wall and extend sensory dendrites along internal structures and the epidermis (Bodmer & Jan 1987a, Corty et al 2016, Finlayson & Lowenstein 1958, Grueber et al 2002, Hughes & Thomas 2007, Schrader & Merritt 2007). A subset of six of these md neurons (Fig. 2.1a) extend axons to more dorsal neuropil regions important for motor control, suggesting that they are proprioceptors that provide

feedback on body position (Corty et al , Grueber et al 2007, Merritt & Whitington 1995, Schrader & Merritt 2000). This feedback is thought to be particularly important during crawling, which involves periodic strides driven by peristaltic waves of muscle contractions along the body (Heckscher et al 2012). However, studies investigating the activity of these sensors have been limited to dissected preparations: imaging of axon terminals in an isolated central nervous system (CNS) suggests that at least some of these neurons are active during muscle contraction (Cheng et al 2010), while an electrophysiology study has shown activity in one cell type in response to stretch in a dissected preparation (Suslak et al 2015). Studies that disabled all or some of these six neurons observed significantly slowed crawling, suggesting that these cells are proprioceptors that provide a segment contraction "mission accomplished" signal that promotes progression of the peristaltic wave (Hughes & Thomas 2007). These behavioral studies concluded that these neurons have partially redundant functions during crawling, because silencing different subsets caused similar behavioral deficits, whereas silencing both subsets had a more severe effect. However, the diverse dendrite morphologies and positions of these proprioceptor neurons (Corty et al 2016, Grueber et al 2002) suggest that each is likely to have distinct sensitivities and functions. Identifying the specific roles of each cell type is not possible without measuring the system's dynamic activity patterns during natural movements to examine the synergies and dynamic encoding properties of the larval proprioceptive circuit.

Here, we characterized the spatiotemporal and functional dynamics of this set of *Drosophila* md proprioceptors by imaging neurons co-expressing GCaMP and tdTomato using SCAPE microscopy, with subsequent dynamic tracking and ratiometric calcium signal extraction. Characterization of the real-time dynamics of segment contraction and extension during crawling and exploratory head movements revealed that proprioceptors increased their

calcium levels in synchrony with deformation of their dendrites. These cells provide a striking sequence of signaling during stereotyped forward crawling, suggesting an elegant continuum of sensing during movement. Furthermore, analysis of sensory responses during non-stereotyped exploration revealed a consistent relationship between activity patterns and more complex, asymmetric segment deformations. These activity patterns were found to be interpretable, via a simple linear combinatorial code, as separable representations of simultaneous turning and retracting movements. Our results provide valuable new input for models of how movements are controlled via feedback in the context of the larval connectome, and also demonstrate a new approach for characterization of body-wide neuronal dynamics in behaving *Drosophila*.

Results

SCAPE microscopy allows 3D imaging of dendritic deformations in behaving larvae

To begin to characterize proprioceptor dynamics as larvae crawl, we focused on the ventral class I neuron vpda (Fig. 2.1a). Class I neurons spread sensory dendrites along the body wall epidermis, suggesting that these cells may detect cuticle folding. To investigate how vpda sensory terminals deform during crawling, we first characterized dendrite dynamics using high-speed volumetric SCAPE microscopy (Bouchard et al 2015, Hillman et al 2018) at 10 volumes per second (VPS) as a larva crawled within a linear channel (Fig. 2.1b-c). To achieve this imaging, we made numerous improvements to our original SCAPE microscopy system including substantially improving spatial resolution to permit individual dendrites to be clearly resolved in 3D at high speed in the freely moving larva. We also increased the field of view to over 1mm and made it sufficiently uniform to capture the entire crawling larva (see methods).

During forward crawling, peristaltic muscle contractions move from posterior to anterior

along the animal (Heckscher et al 2012). vpda proprioceptors expressing GFP as a static marker showed repeated folding and extension; folding as a peristaltic wave entered a segment, and extending as the wave moved to anterior segments (Fig. 2.1c-c´´´, Movie 2.1). Viewed in cross section, vpda dendrite tips flexed from distal to proximal, eventually angling at approximately 90˚ during each peristaltic contraction (Fig. 2.1c´´). Since class I dendrites are positioned along the basal surface of the epidermis (Kim et al 2012), vpda dendrite dynamics likely reflect body wall dynamics. Therefore, our data indicate that vpda dendrites are positioned to respond to repeated contraction and extension of the body wall that occurs during crawling.

SCAPE microscopy of neuronal calcium activity dynamics in behaving larvae

Next, we sought to reveal if and how the activity of these neurons changes as the dendrites fold during segment contraction. If vpda neurons indeed function as proprioceptors, we should be able to detect activity in these cells during locomotion. We built a dual-expression line of larvae to label targeted proprioceptive cells with both calcium-sensitive GCaMP (green) and static tdTomato (red). To acquire SCAPE microscopy data in this model, we optimized parallel dual color imaging and developed a tracking algorithm that localizes the cell bodies via their static red fluorescence. These tracked cells were then used as fiducials for quantification of movement and behavior, as well as to extract and ratiometrically correct simultaneously recorded GCaMP fluorescence from the same cells.

We used the inter-cell distance between the measured neuron and a homologous neuron in the posterior or anterior segment as our measure of segment contraction and extension. We observed consistent rises in GCaMP fluorescence in vpda neurons during each segment contraction (Fig. 2.2a-d). Calcium signals subsided as the peristaltic wave progressed to adjacent

anterior segments (Fig. 2.2b, d; Movie 2.2-2.3). Dynamic calcium responses were also visible in dendritic arbors and axons (Fig. 2.2c-c´, arrowheads and arrows). Note that because of variability in calcium signal amplitude across contraction events (Fig. 2.2b), signals were normalized for the averages shown in Fig. 2d (see methods).

As a control, an additional larva line co-expressing GFP and tdTomato in vpda neurons was imaged using SCAPE during crawling. Applying the same tracking and ratiometric correction as for GCaMP, we observed insignificant changes in ratiometrically corrected GFP signal during crawling (Fig. 2.3). Taken together, our data indicate that vpda neurons respond to body wall folding during segment contraction.

Monitoring of different proprioceptive cell types reveals distinct activity patterns

Having established this pipeline for cell characterization, SCAPE was then used to monitor the physical and functional dynamics of the remaining proprioceptive cell types, each of which has unique dendrite morphologies and positions (Fig. 2.1a). Two additional class I neurons besides vpda project secondary dendrites along the dorsal side of the body wall (ddaD anteriorly and ddaE posteriorly; Fig. 2.1a) (Grueber et al 2002). These neurons are poised to detect cuticle folding on the dorsal side of the animal. In addition, dorsal and ventral bipolar dendrite md neurons (dbd and vbd, respectively) extend in an anterior-posterior direction and it is known that at least dbd extends along internal connective tissue (Schrader & Merritt 2007). By contrast, neuron dmd1 extends an atypical thick dendrite from the body wall to the internal intersegmental nerve (ISN; (Corty et al 2016)), which lies along the muscle layer, suggesting that this proprioceptor could be poised to detect muscle dynamics.

Imaging of dorsal class I neurons revealed that ddaE and ddaD dendrites deform as the peristaltic wave enters each segment, and flatten as the wave passes (Fig. 2.4a-a´´´; Movie 2.4

first section). While there is some variability in the degree of dendrite deformation, we consistently see folding in both cell types, with ddaE folding before ddaD (Fig. 2.4a´´-b) in synchrony with the posterior to anterior progression of peristaltic waves. Like vpda, calcium dynamics revealed increases in dorsal class I activity during segment contraction (Fig. 2.4c-d, Fig. 2.6, Movie 2.5 first section). When comparing paired ddaE and ddaD cells within the same segment, responses of posterior ddaE and anterior ddaD neurons occurred in succession during segment contraction, with ddaE responding just before ddaD (Fig. 2.5a, c), corresponding to the lag in dendrite folding. These data suggest that cellular calcium activity is a result of dendritic folding in all class I neurons. As a control, larvae were imaged under compression with a glass coverslip that prevented physical folding of the ddaD dendrites (Fig. 2.7). In this case, no increases in ddaD calcium activity were seen during forward crawling, consistent with dendritic folding driving calcium activity. This same compression did not prevent dendritic folding in ddaE neurons, and accordingly this cell type continued to show activity during crawling. This result further highlights the importance of imaging freely crawling larvae for characterization of locomotion, since physical restraint itself appears to influence proprioceptive signaling.

The remaining three proprioceptor types have relatively internal locations, and complex 3D motion paths during crawling. We leveraged SCAPE's high-speed volumetric imaging capabilities to capture the distinct 3D movements and activity dynamics of these dmd1, dbd, and vbd proprioceptors during crawling. dmd1 dendrites were slack and coiled prior to the contraction wave, then as the segment contracted, the dendrite bundle stretched anteriorly and was then pulled deeper into the animal (Fig. 2.4e´-e´´, Movie 2.4 second section). As the segment extended, the bundle swung posteriorly and then returned to the coiled position. GCaMP imaging revealed increases in calcium activity in dmd1 during segment contraction, as

the dendrite bundle stretched (Fig. 2.4g, Fig. 2.6, Movie 2.5 second section).

Dbd and vbd dendrites folded as the segment contracted (Fig. 2.4e′ arrowhead, Fig. 2.4i-i′′, Movie 2.4). For dbd, GCaMP fluorescence peaked during segment stretch (Fig. 2.4h, Fig. 2.6, Movie 2.5 second section), consistent with previous electrophysiology results in a dissected prep (Suslak et al 2015). However, in contrast to dbd, GCaMP fluorescence in vbd peaked during segment contraction (Fig. 2.4j, Fig. 2.6, Movie 2.5 third section). Thus, two proprioceptors with similar morphologies and dendrite dynamics can show distinct responses during crawling.

We next tracked groups of co-labeled dorsal proprioceptors to directly compare the timing of their activity during forward crawling. We found that each cell type is active sequentially during segment contraction (Fig. 2.5). dbd is most active in a stretched or relaxed segment. Then as the segment contracts, dmd1 activity increases first, followed by the class I neurons (ddaE and ddaD) as the cuticle folds during segment shortening (Fig. 2.5a). Comparison of the time at half-maximum calcium activity confirmed that ddaD activity was significantly delayed relative to ddaE during forward crawling (Fig. 2.5c; $p=0.01$ by single tail paired t-test) and that ddaE activity occurs significantly later than dmd1 activity during forward crawling (Fig. 2.5b, $p=0.0078$ by single tail paired t-test).These data suggest that the unique dendrite morphology of each dorsal proprioceptor tunes each cell to respond at different times during a peristaltic wave. These activities could provide a continuum of cell-type specific encoding during movement.

Proprioceptor activity can simultaneously code for head turning and retraction

In addition to imaging simple forward crawling, our SCAPE imaging experiments captured a wide range of movements during exploration. To examine how proprioceptive activity might provide feedback during more complex body movements, we mounted the larvae in a

small arena bounded by agarose. With this setup, we were able to track and extract dorsal sensory activity during exploratory head movements.

In many cases, we observed typical exploration behavior, in which larvae bend their bodies asymmetrically to turn left or right, while concurrently retracting the head (Fig. 2.8a-a′′′; Movie 2.6). These behaviors are not always synchronized, which can lead to a complex motion path for each neuron and segment compared to locomotion. However, SCAPE recordings confirmed that even for this less-stereotyped motion, class I activity increases continue to be associated with segment contraction. In the dataset shown in Fig. 2.8, we focused on ddaD and ddaE within thoracic segment T3 (termed D1 and E1), and ddaD within abdominal segment A1 (termed D2), since these cells were deformed by the observed exploratory movements. Calcium activity in these cells correlated with the distance between ipsilateral D1 and D2 neurons (termed inter-cell distance) (Fig. 2.8b, Movie 2.6, see Table 2.1 for correlation coefficients and further discussion of ddaE). Calcium signal changes in ddaD neurons were greater than those in ddaE, consistent with greater measured changes in dendrite length for ddaD than for ddaE neurons during these turning and retraction events (ddaD=32% ± 25% s.d.; ddaE=10% ± 6.6% s.d.).

We next examined whether the seemingly complex inter-cell distances and calcium signals could be interpreted in terms of the larva's combined turning and head retracting behavior. Examining the physical properties of the larva's motion (see geometric model in methods), we note that head retraction and turning are distinct in that retraction is symmetric and head turning is asymmetric. Subtracting the D1-D2 inter-cell distance on the left side of the larva from the D1-D2 inter-cell distance on the right-side neuron pair should thus cancel out the effect of symmetric head retraction. This differential distance was found to closely match the calculated angle of the segment (providing a turning metric). Furthermore, assuming rigid coupling between

the left and right cells, we found that adding the left D1-D2 inter-cell distance to the right D1-D2 inter-cell distance cancelled out the effect of turning (which has a reciprocal effect on left and right inter-cell distance) providing a measure consistent with the timing of the larva's head retractions (a retraction metric).

Following the same logic, we computed the difference and summation of GCaMP6f signals extracted from proprioceptors on the left and right sides of the body. Remarkably, we found that the difference between calcium signals on the left versus right side correlates well with turning angle, especially for ddaD cells (Fig. 2.8c, Table 2.1). Similarly, the sum of the calcium signals from the left and the right sides correlates strongly with our retraction metric for each cell type (D1, E1, D2) (Fig. 2.8d, Table 2.1). Correlation values are even stronger when delays between movement and calcium transients are incorporated into comparisons (Table 2.1).

These data indicate that proprioceptor activity during exploration can represent simultaneous head turning and retraction. Furthermore, our data suggest that linear combinations of calcium signals from left and right neuron pairs can provide independent metrics of turning and head retraction.

Discussion

This study demonstrates a new approach for live volumetric imaging of sensory activity in behaving animals, leveraging an optimized form of high-speed SCAPE microscopy (Bouchard et al 2015, Hillman et al 2018). We used this methodology to examine the activity patterns of a heterogeneous collection of proprioceptive neurons during crawling, as well as during more complex movements such as head turning and retraction, to determine how larvae sense body shape dynamics. Imaging revealed 3D distortion of proprioceptive dendrites during movement,

and GCaMP activity that occurred coincident with dendritic deformations. We note that our results are consistent with a complementary study by He et al., which examined ddaD and ddaE dorsal proprioceptors and also demonstrated increased activity during dendrite folding (He et al 2019). Their study elucidated that this deformation-dependent signaling is reliant on the mechanosensory channel TMC.

Our survey of the full set of proprioceptors in behaving larvae revealed that most neurons (all class I neurons, dmd1, and vbd) increase activity during segment contraction. By contrast, dbd neurons showed increased activity during segment stretch, which is consistent with previous electrophysiological recordings of dbd in a dissected preparation (Suslak et al 2015). The temporal precision afforded by high-speed SCAPE microscopy further revealed that different proprioceptors exhibit sequential onset of activity during forward crawling. Timing of activity was associated with distinct dendrite morphologies and movement dynamics, suggesting that proprioceptors monitor different features of segment deformation. The complementary sensing of segment contraction versus stretch in class I/dmd1/vbd versus dbd neurons provides an additional measure of movement that is conceptually similar to the responses of Golgi tendon organs versus muscle spindles in mammals (Proske & Gandevia 2012). Combined, these results indicate that this set of proprioceptors function together to provide a continuum of sensory feedback describing the diverse 3D dynamics of the larval body.

Prior work suggested that the proprioceptors studied here have partially redundant functions during forward crawling because silencing different subsets caused similar behavioral deficits, namely slower crawling, whereas silencing both subsets had a more severe effect (Hughes & Thomas 2007). Slow locomotion may be a common outcome in a larva that is lacking in part of its sensory feedback circuit, yet our results suggest that each cell type has a unique

role. Our demonstration of the varying activity dynamics of proprioceptors during crawling and more complex movements indicates that diverse sensory information is available to the larva, and suggests that feedback from a combination of these sensors could be used to infer aspects of speed, angle, restraint and overall body deformation. This feedback system is likely to be important for a wide range of complex behaviors, such as body bending and nociceptive escape.

How can an understanding of proprioceptor activity patterns inform models of sensory feedback during locomotion? Electron microscopic reconstruction has shown that ddaD, vbd, and dmd1 proprioceptors synapse onto inhibitory PMSI pre-motor neurons (A02b) (Schneider-Mizell et al 2016), which promote segment relaxation and anterior wave propagation (Kohsaka et al 2014). Thus, activity of these sensory neurons may signal successful segment contraction and promote forward locomotion, in part by promoting segment relaxation. Furthermore, vpda neurons provide input onto excitatory premotor neurons A27h, which acts through GDL interneurons to inhibit contraction in neighboring anterior segments, thereby preventing premature wave propagation (Fushiki et al 2016). In this way, vpda feedback could contribute to proper timing of contraction in anterior segments during forward crawling. In contrast to other proprioceptors, dbd neurons are active during segment stretch. Their connectivity also tends to segregate from contraction sensing neurons (Heckscher et al 2015, Schneider-Mizell et al 2016) and understanding how the timing of this input promotes wave propagation is an important future question. Our dynamic recordings of the function of these neurons during not just crawling, but also exploration behavior provides essential new boundary data for testing putative network models derived from this anatomical roadmap.

SCAPE's high-speed 3D imaging capabilities enabled 10 VPS imaging of larvae during rapid locomotion. Fast volumetric imaging not only prevented motion artifacts, but it also

revealed both the 3D motion dynamics and cellular activity associated with crawling behavior. SCAPE's large, 1 mm wide field of view allowed multiple cells along the larva to be monitored at once, while providing sufficient resolution to identify individual dendrite branches. Because SCAPE data is truly 3D, dynamics could be examined in any section or view. Additionally, fast two-color imaging enabled simultaneous 3D tracking of cells, monitoring of GCaMP activity, and correction for motion-related intensity effects. Our demonstration that larvae that are compressed during crawling exhibit altered dendrite deformation, and thus altered proprioceptive signaling (Fig. 2.7) underscores the benefit of being able to image unconstrained larvae, volumetrically in real-time. Furthermore, rapid volumetric imaging allowed for the analysis of sensory responses during non-stereotyped, exploratory head movements in 3-dimensions, revealing activity patterns that could be utilized for encoding of complex, simultaneous movements. This finding also demonstrates the quantitative nature of SCAPE data and its high signal to noise, which enabled real-time imaging of neural responses without averaging from multiple neurons.

Here, we provide an example of how high-resolution, high-speed volumetric imaging enabled investigation of the previously intractable question of how different types of proprioceptive neurons encode forward locomotion and exploration behavior during naturalistic movement. Imaging could readily be extended to explore a wider range of locomotor behaviors such as escape behavior, in addition to other sensory modalities such as gustation and olfaction. Detectable signals reveal rich details including the firing dynamics of dendrites and axonal projections during crawling. Waves of activity in central neurons within the ventral nerve cord can also be observed. We expect that the *in vivo* SCAPE microscopy platform utilized here could ultimately allow complete activity mapping of sensory activity during naturalistic behaviors

throughout the larval CNS. Using SCAPE, it is conceivable to assess how activity from proprioceptive neurons modulates central circuits that execute motor outputs, which will provide critical information for a dissection of the neural control of behavior with whole animal resolution.

Methods

Animals

Drosophila melanogaster strains were maintained on standard molasses food (agar, cornmeal, yeast, molasses, methylparaben, ethanol, propionic acid, penicillin, streptomycin) at 25° C, 60% humidity. Fly lines were obtained from the Bloomington (BL) Drosophila Stock Center or published sources as noted below. To image class I da neurons we used 221-Gal4 (Grueber et al 2003a), UAS CD4-tdGFP (BL#35839) and IT.410-Gal4 (BL#63298), 20XUAS-IVS-GCaMP6f (2 copies, BL#52869 and BL#42747), UAS-CD4-tdTomato (BL#35841). To image GFP dynamics as a control, we used IT.410-Gal4, 20XUAS mCD8::GFP (BL#32194), UAS-CD4-tdTomato. To image all dorsal proprioceptors, we used GMR10D05-Gal4 (BL#48438), 20XUAS mCD8::GFP or GMR10D05-Gal4, 20XUAS-IVS-GCaMP6f (2 copies), UAS-CD4-tdTomato. To image vbd we used IT.1129-Gal4 (BL#65461), 20XUAS-IVS-GCaMP6f (2 copies), UAS-CD4-tdTomato. Animals of either sex were used. 2nd instar larvae were used for all imaging experiments, except 3rd instar larvae were used for imaging of compressed animals.

SCAPE Image acquisition

High-speed volumetric imaging of crawling larvae was performed using a custom swept confocally aligned planar excitation (SCAPE) microscope extended from designs described in (Bouchard et al 2015, Hillman et al 2018). Briefly, high speed 3D imaging is achieved by illuminating the sample with an oblique light sheet through a high NA objective lens (Dunsby 2008). Fluorescence light excited by this sheet (extending in y-z') is collected by the same objective lens (in this case an Olympus XLUMPLFLN 20XW 1.0 NA water immersion objective with a 2mm working distance). A galvanometer mirror in the system is positioned to both cause the oblique light sheet to scan from side to side across the sample (in the x direction, without a change in the angle of the sheet) but also to descan returning fluorescence light. This optical path results in an intermediate, descanned oblique image plane which is stationary yet always co-aligned with the plane in the sample that is being illuminated by the scanning light sheet. Image rotation optics and a fast sCMOS camera (Andor Zyla 4.2) are then focused to capture these y-z' images at over 1000 frames per second as the sheet is scanned in the sample in the x direction. Data is then reshaped into a 3D volume by stacking successive y-z' planes according to the scanning mirror's x-position. All other system parts including the objective and sample stage are stationary during high speed 3D image acquisition, including the primary objective lens and sample stage. No image reconstruction procedures besides correction for the sheet's oblique angle were used for data shown in this study.

For SCAPE imaging in this study, numerous refinements to our original SCAPE design were made to improve resolution and field of view, including optimization of light sheet formation to achieve uniformity over the field of view. The scanning system was optimized to ensure that the light sheet angle at the sample did not tilt during scanning, while optimized

alignment of the detection system reduced aberrations and increased numerical aperture to yield higher diffraction limited resolution and light throughput. The new system's stationary objective was configured in an inverted arrangement for the ventral side imaging and an upright arrangement for the dorsal side imaging. Dual-color imaging was achieved using a custom-built dual color image splitter in front of the sCMOS camera. 488 nm excitation (<5 mW at the sample, Coherent OBIS) was used to excite fluorescence in both channels, with 525/45 nm and 600/50 nm emission filters in the green and red emission channels respectively. The system's camera frame rate to read 150-200 rows (corresponding to oblique depths along z') was 1000-1300Hz, with an x-scanning step size of 2~3μm to achieve 10 volumes per second imaging over a field of view of 1000 × 250 × 195 μm (y-x-z)(scan parameters varied for different trials, based on the size difference of each larva).

To image forward crawling, 2nd instar larvae were chosen to image multiple segments at once. Larvae were imaged at room temperature while positioned within a 300μm wide water-filled channel bounded by FEP spacers and covered by a 40mm × 24mm cover glass. When imaging the ventral side, the channel was positioned on a 50mm × 24mm cover glass, when imaging the dorsal side, the channel was positioned on a glass slide. Each trial acquired data for up to 120 seconds or was terminated earlier if the larva crawled to the end of the channel. A manual translation stage aligned along the FEP channel axis was used to keep the larva in the field of view during the acquisition as needed.

To image compressed animals, we reproduced typical conditions for confocal microscopy imaging of larvae. As such, 3rd instar larvae were positioned in a 50:50 mixture of halocarbon oils 27 and 700 to enhance compression with an overlying coverslip. We ensured that cross sections of the animal showed body compression during imaging (Fig. 2.7).

To image complex head movements (turns and retractions) during exploration behavior, we constrained 2nd instar larvae in a small water-filled arena bounded by 10% agarose, with a coverslip on top. The size of the arena is about 1000μm by 500μm and it was made on a ~200μm thick agarose pad.

All the functional calcium signal analysis used signals extracted from raw, linear-scale imaging data. However, for the visualizations of SCAPE images shown in the figures and movies, raw camera 16bit data was square root scaled to enhance the visible dynamic range to avoid display saturation and to make all components (soma and dendrites) more visible. Resulting pixel values are then shown on a linear gray, red or green colorscale without further adjustment. SCAPE data was interpolated to uniform voxels with spline smoothing for all the figures and movies, and sharpened using the imageJ function 'unsharp mask' (radius:1.5, weight:0.4) to enhance dendrite visualization except for Fig. 2.2a-a′ and Movies 2.2, 2.3, 2.4 fourth section, 2.5 first and second sections. None of the raw SCAPE imaging data was saturated during acquisition. Images and movies were generated using Matlab and ImageJ.

Cell tracking and ratiometric GCaMP analysis

For SCAPE imaging quantification, vpda, vbd, and dbd neurons were first manually selected and then automatically tracked in 3D space for the duration of the run that the neuron was within the field of view, using Matlab. For other neuron types (ddaD, ddaE, dmd1), since the distance between neighboring neurons is small, automatic tracking was performed under supervision and manually corrected when needed. Tracked neurons are from segments A1-A6. This 3D tracking provided behavioral information related to the animal's physical movements, as well as fiducials for extraction of GCaMP fluorescence from the cells during movement.

We chose GCaMP6f because it has a fast decay time (~400 ms (Chen et al 2013)), which is faster than the decay seen in our data (see real time traces Figures 2.2, 2.3, 2.6, decay happens over seconds).

For fluorescence extraction, tracking regions of interest (ROIs) were defined as the smallest rectangular 3D cube around the tracked cell that encompassed the entire cell body. Average fluorescence intensity values of GCaMP6f and tdTomato were then extracted from these ROIs for each time point. A ratio between GCaMP6f and tdTomato was calculated after subtraction of background signal to account for the motion induced intensity change for each frame (yielding the green-to-red ratio R). The average of the lowest 10% ratio values was used as the baseline (R_0) for each ROI. The GCaMP signal reported as neural activity at each time point then corresponds to the change in this ratio from baseline ($\Delta R/R_0$). To demonstrate this process, raw red, green and ratiometric signals are shown in Fig. 2.3. In addition, control measurements are shown that applied the same analysis to larvae co-expressing tdTomato and static GFP. In the GFP case, dynamic changes in $\Delta R/R_0$ were insignificant, confirming the sensitivity of our ($\Delta R/R_0$) measure to the intracellular calcium-dependent fluorescence of GCaMP.

Calculating segment and dendrite dynamics

To relate calcium dynamics to segmental contraction and extension phases, changes in inter-cell distances were calculated from the tracked cell coordinates – defined as the distance between the measured neuron and a homologous neuron in the posterior or anterior segment over time. For vpda and vbd, we plotted posterior-intercell distance between the measured neuron and a homologous neuron in the posterior segment. For dbd, dmd1, ddaE, and ddaD we plotted the posterior inter-cell distance between the ddaE neuron in the same segment as the cell of interest

and the homologous neuron in the next posterior segment. This allowed us to directly compare the timing of dorsal neuron activity. For some plots of ddaD activity (Fig. 2.4d, Fig. 2.7), we plotted anterior inter-cell distance between the measured neuron and the homologous ddaD neuron in the anterior segment, since this was a better proxy for dendrite folding.

To directly measure dendrite dynamics in ddaD and ddaE neurons during crawling (Fig. 2.4b) and turning (Fig. 2.8), dendrite length was measured as a 180 degree line from the cell body to the furthest visible dendrite. In crawling animals (Fig. 2.4b), 2-3 cells of each type from segments A1-A6 were analyzed from 4 different animals, and each cell was analyzed during a different peristaltic wave.

Averaging dynamics across larvae

Real-time traces of inter-cell distance and $\Delta R/R_0$ shown in Figures 2.2, 2.3, and 2.6, demonstrate the high signal to noise and repeatability of our observations. However, these traces also demonstrate that the speed of crawling can vary quite significantly between animals, in addition to the relative amplitude of ($\Delta R/R_0$). To provide the aggregate, average properties of neural activity against segment contraction, it was thus necessary to normalize these differences between animals. To calculate mean calcium responses ($\Delta R/R_0$) in relation to segment contraction, we normalized amplitude of responses across events to 1, so as not to bias the average values to cells that responded more strongly (Fig. 2.2d, Fig. 2.4). To plot mean calcium activity ($\Delta R/R_0$), inter-cell distance, or dendrite measurements across animals with different crawling speeds, normalization was applied in time based on the full width at half maximum (FWHM) of the mean inter-cell distance of every contraction for each animal (Fig. 2.4c, d, g, h, j). 1 A.U. ranges from 0.7-2.5 seconds. We excluded the contraction events which inter-cell

distance did not return back to the resting length, and we did not include more than two events per neuron for the averaging analysis. To test the activity timing lag between neuron types (Fig. 2.5b-c), we compared the normalized time at half-maximum calcium activity.

To characterize the resting and contraction phase activity in Fig. 2.3c, we defined the contraction phase as 2×FWHM window centered at the maximum contraction point and resting phase as the 0.5×FWHM window prior to the contraction phase. The resting phase GFP-tdTomato or GCaMP6f-tdTomato ratio value was calculated by taking the mean $\Delta R/R_0$ along the resting phase window. And the contraction phase GFP-tdTomato or GCaMP6f-tdTomato ratio value was calculated by taking the maximum $\Delta R/R_0$ over the contraction phase window.

Motion model for exploring larva

We made the following assumptions based on the properties of motion of the tracked neurons D1L (left anterior ddaD), D1R (right anterior ddaD), D2L (left posterior ddaD) and D2R (right posterior ddaD) that:

1. The lava's right and left neurons are positioned either side of a rigid bar of length ~2p
2. Turning motion is given by a time-varying rotation θ (t) of the anterior bar about the midpoint of the posterior bar.
3. The retraction motion of the larva was approximated as a time-varying distance S(t) between the midpoints of each bar.

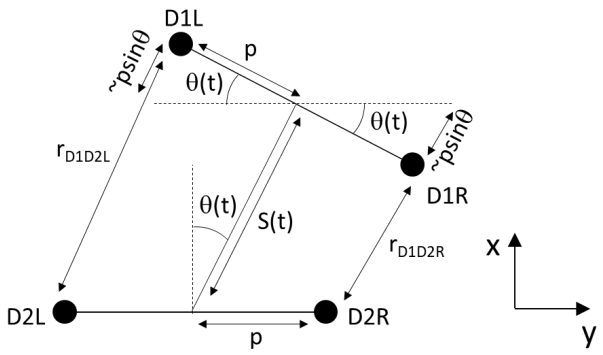

From this construction, we can see that good approximations to the distance between D1R and D2R (r_{D1D2R}) and D1L and D2L (r_{D1D2L}) are simply:

$$r_{D1D2L} = S_2(t) + p.\sin(\theta(t))$$

$$r_{D1D2R} = S_2(t) - p.\sin(\theta(t)) \quad \text{Eq 1}$$

From this relationship, it is simple to see that the subtraction or summation of these two inter-cell differences are going to yield:

$$r_{D1D2L} - r_{D1D2R} = 2p\sin\theta(t) \quad \text{Eq 2}$$

which is a pure function of turning angle, and

$$r_{D1D2L} + r_{D1D2R} = 2S_2(t) \quad \text{Eq 3}$$

which is a pure function of time-varying head retraction.

This 'common mode rejection' property holds true for the positional data of the larva's neurons, as well as the subtraction and summation of the left and right GCaMP signal extracted from neurons innervating the inter-cell space.

A more rigorous derivation notes that the precise value of the inter-cell distance is given by:

$$r_{D1D2L} = S_2(t) + p.\sin(\theta(t)) + ((p-p.\cos(\theta(t))^2+(S_2(t)+p.\sin(\theta(t)))^2)^{1/2}$$

$$r_{D1D2R} = S_2(t) - p.\sin(\theta(t)) + ((p-p.\cos(\theta(t))^2+(S_2(t)-p.\sin(\theta(t)))^2)^{1/2} \quad \text{Eq 4}$$

however, the difference between this and our approximation is <0.12% for the motion parameters of the larva observed.

Quantification and Statistical Analysis

Statistical tests were performed using Matlab. We evaluated the lag between dmd1 vs. ddaE and ddaE vs. ddaD activity by single tailed paired t-test, alpha level 0.05. We evaluated the difference between the resting and contraction phases for the GFP-tdTomato and GCaMP6f-tdTomato ratios with two-tailed paired t-test. No optimal sample-size estimation was calculated. Statistical parameters reported in figure legends. All p values are represented as: * < 0.05, ** < 0.01, and *** < 0.001.

Chapter 2 Figures and Tables

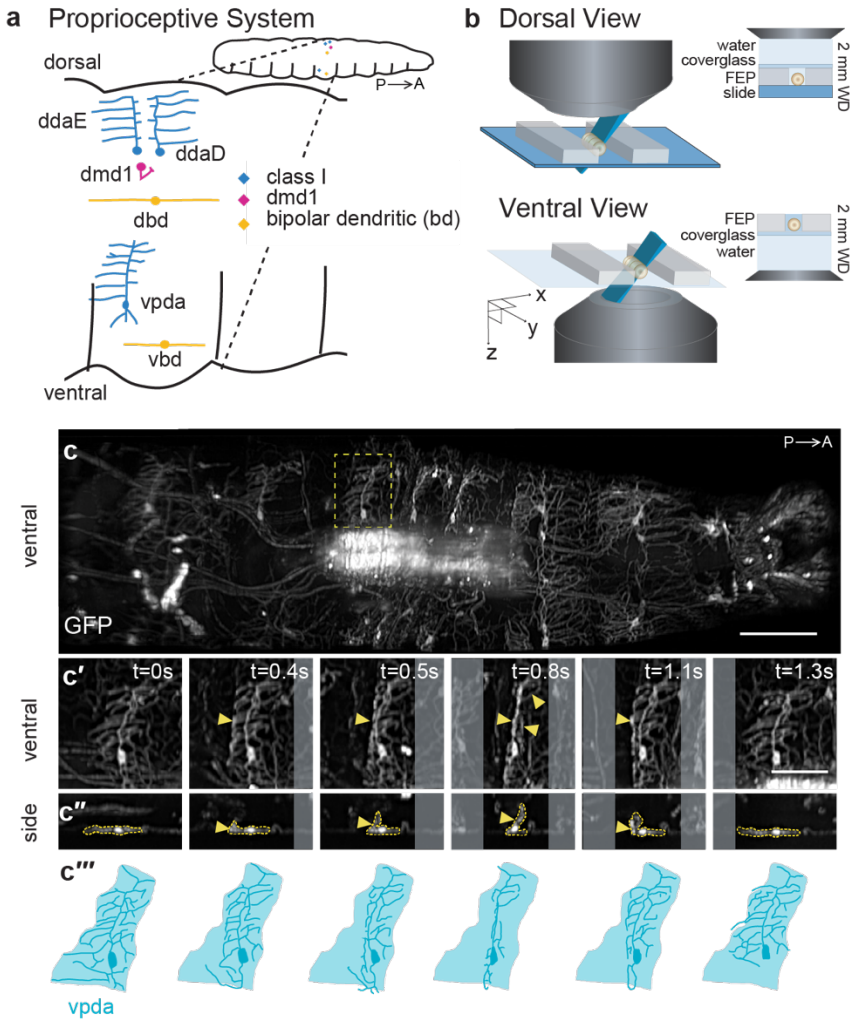

Figure 2.1. SCAPE imaging of proprioceptor dendrite motion dynamics in crawling larvae
(a) Schematic of the larval proprioceptive system. P=posterior, A=anterior.
(b-b´) Schematic of larval imaging platform for SCAPE microscopy (see methods).
(**c**) SCAPE imaging of *221-Gal4*, *UAS-CD4tdGFP* larva ventral side during crawling, Maximum Intensity Projection (MIP) over a 95 µm depth range from a 160µm deep volume (to exclude gut autofluorescence, square root grayscale – see methods). See Movie 2.1. Yellow box indicates neuron examined in **c´-c´´´. (c´-c´´)** vpda in ventral view **(c´)** and side view **(c´´)** in successive time lapse frames during forward crawling. vpda dendritic arbors and cell body are outlined in yellow. Other arbors are from class IV neurons. **(c´´´)** Tracing of neurons in **c´**. Shaded areas represent dendritic field territory before folding.
Posterior is to the left for all images.
Scale bar=100 µm in **c**. Scale bars=50 µm in **c´-c´´.**

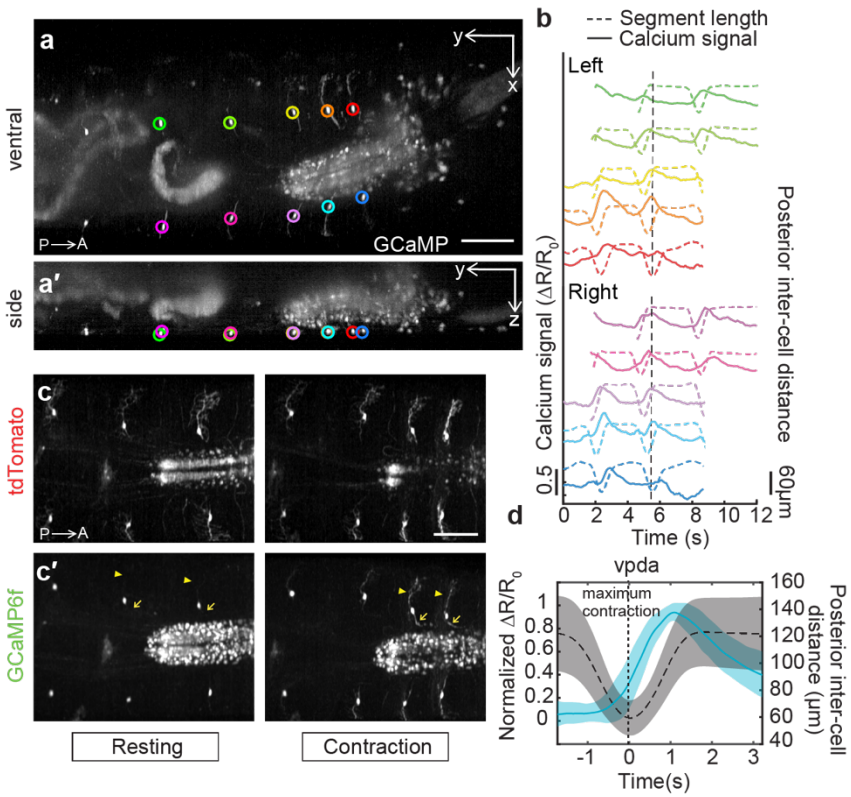

Figure 2.2. Dual-color SCAPE imaging of proprioceptor activity dynamics in crawling larvae
(a-a´) SCAPE imaging of a *410-Gal4, 20XUAS-IVS-GCaMP6f* (x2), *UAS-CD4tdTomato* larva, ventral side, during forward crawling. Images are MIP of a full 168µm deep imaging volume (square root grayscale). **(a)** shows a ventral view (x-y) and (**a´**) shows side view (y-z). GCaMP signal was extracted from the segmentally repeated vpda neurons indicated by circles. See Movie 2.2.
(b) vpda soma response for the neurons tracked in **(a)**. The distance between the measured neuron and the posterior neuron (posterior inter-cell distance) is plotted in dashed lines and the GCaMP6f response is plotted in solid lines (quantified as the fractional change in the green / red fluorescence ratio $\Delta R/R_0$ – see methods and Figure 2.3). Dotted vertical line refers to time point shown in **a**.
(c) Representative tdTomato and **(c´)** GCaMP6f images showing increased activity in dendrites (arrowhead) and axons (arrow) during contraction. Images cropped to show region of interest and are MIP of a 70 µm depth range from a 160 µm deep volume (square root grayscale). See Movie 2.3.
(d) Mean calcium response (solid line) ± standard deviation (s.d., ribbon) of vpda soma (3 animals, n=22 cells (8, 10, and 4), 26 events (9, 13, and 4 respectively)) during segment contraction, represented by mean posterior inter-cell distance (dashed line) ± s.d. (ribbon). Maximal segment contraction is set at 't=0s' for each event. $\Delta R/R_0$ amplitude was normalized for each event.
Posterior is to the left for all images.
Scale bars=100 µm.

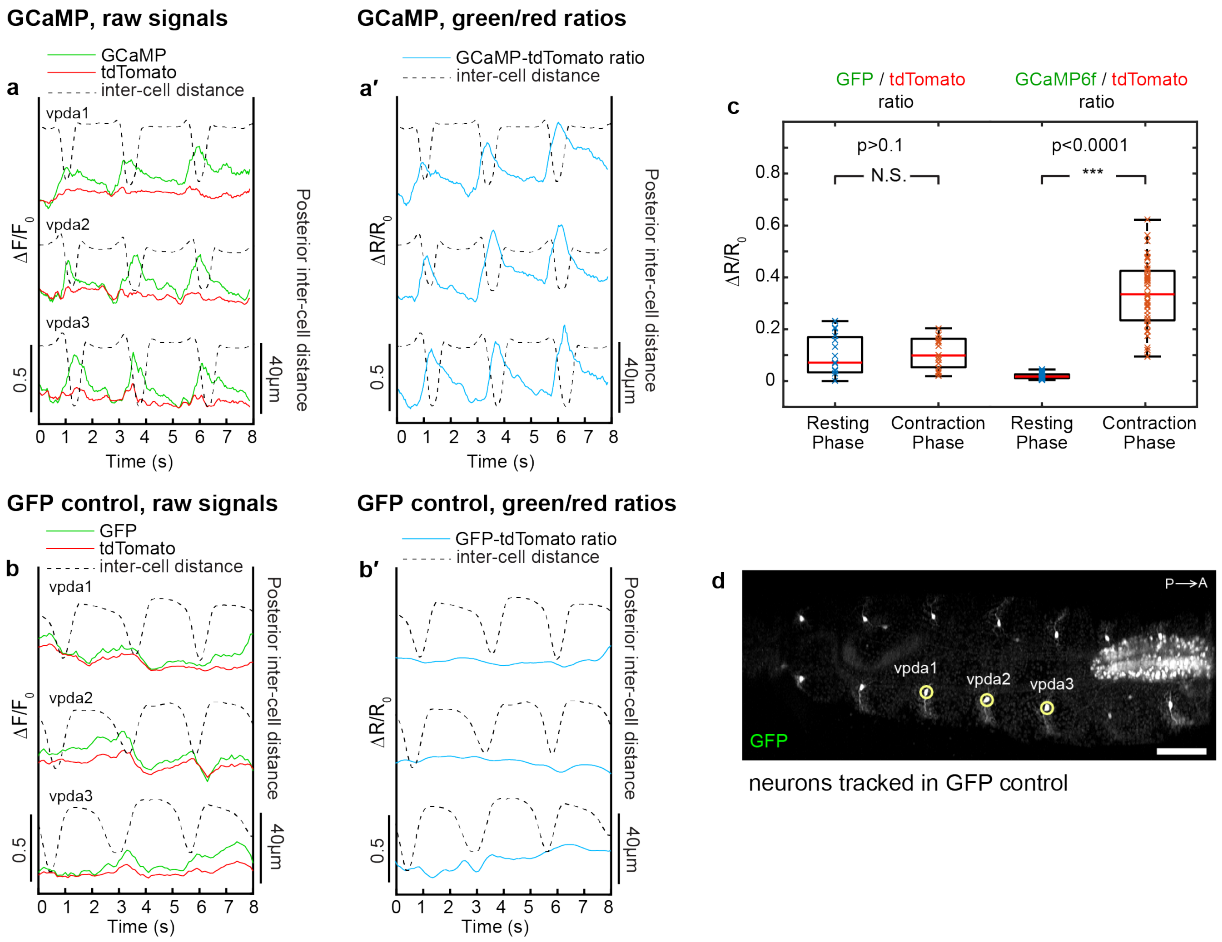

Figure 2.3. Ratiometrically measured calcium dynamics properly control for motion artifacts
(a) Change in fluorescence from baseline ($\Delta F/F_0$) in GCaMP6f (green) and tdTomato (red) during crawling in vpda neuron somas. Segment contraction is depicted with inter-cell distance (dashed lines). **(a´)** Change in ratio of GCaMP6f to tdTomato fluorescence ($\Delta R/R_0$, blue). Increases can be seen during segment contraction.
(b) Change in fluorescence from baseline ($\Delta F/F_0$) in GFP (green) and tdTomato (red) during crawling in vpda neuron somas. Segment contraction is depicted with inter-cell distance (dashed lines). (**b´**) Change in ratio of GFP to tdTomato fluorescence ($\Delta R/R_0$, blue). No increase is associated with segment contraction.
(c) Comparison of GFP-tdTomato and GCaMP6f-tdtomato ratios between resting and contraction phases (see methods). For GFP-tdTomato analysis, n= 2 animals, 7 cells, 14 events, for GCaMP6f-tdtomato analysis, n=3 animals, 22 cells, 26 events. Note that there is no difference between GFP-tdTomato ratios in the resting versus contraction phases, while there is a significant increase in GCaMP6f-tdTomato ratios during contraction ($p<0.001$, as measured by two-tailed t-test).
(d) SCAPE imaging of *410-Gal4, 20XUAS mCD8::GFP*, *UAS-CD4-tdTomato* animals during forward crawling, Ventral side. Imaging shows vpda neurons. GFP channel is shown. Posterior is to the left. Images are shown on a square root grayscale to reduce dynamic range for visualization of both cell bodies and dendrites.
Scale bar=100µm.

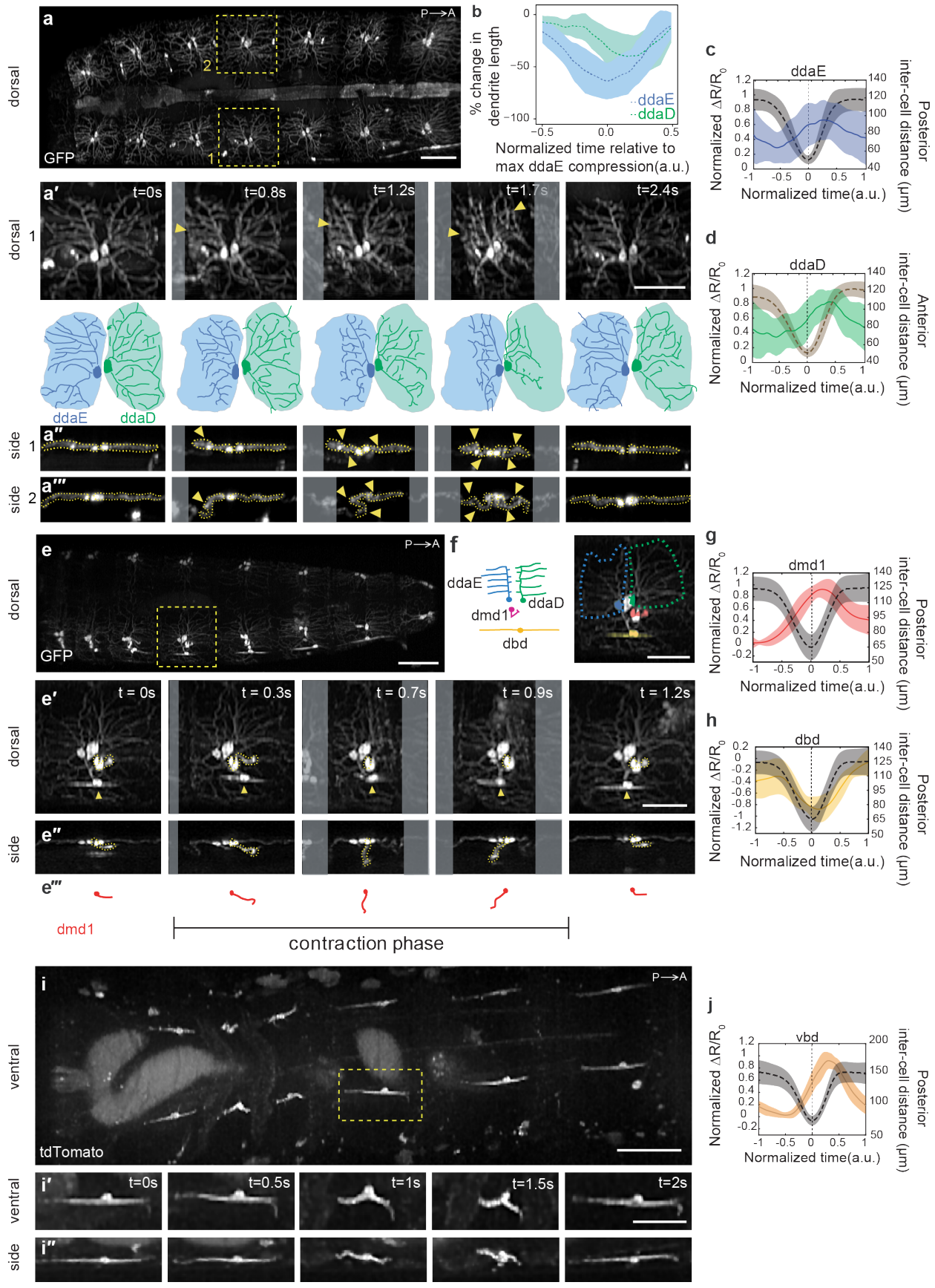
a
P→A
dorsal
GFP
2
1
b
% change in dendrite length
0
−50
−100
−0.5
0.0
0.5
ddaE
ddaD
Normalized time relative to max ddaE compression(a.u.)
c
ddaE
Normalized ΔR/R0
Normalized time(a.u.)
Posterior inter-cell distance (μm)
d
ddaD
Anterior inter-cell distance (μm)
a′
t=0s
t=0.8s
t=1.2s
t=1.7s
t=2.4s
1
ddaE
ddaD
side
a″
a‴
2
e
e′
t = 0s
t = 0.3s
t = 0.7s
t = 0.9s
t = 1.2s
e″
e‴
dmd1
contraction phase
f
dbd
g
dmd1
h
dbd
i
ventral
tdTomato
i′
t=0s
t=0.5s
t=1s
t=1.5s
t=2s
i″
j
vbd

Figure 2.4. Proprioceptors with diverse morphologies show distinct activity patterns during forward crawling
(a) Single frame from SCAPE movie of larva during crawling with ddaD and ddaE neurons visible on the dorsal side. Neurons were labeled using *221-Gal4*, *UAS-CD4tdGFP*. Yellow box indicates neurons examined in time lapse sequences below. (**a´)** Top: enlarged dorsal view of right side neurons (1). Arrowheads indicate regions of dendrite folding. Bottom: tracing of neurons in **a´**. Shaded areas represent dendritic field territory before folding. **(a´´- a´´´)** Side view of right side neuron (1), and left side neuron (2) during segment contraction.
(**b)** Mean (± s.d.) percent change in dendritic length along the anteroposterior axis (a measure of dendritic folding) of ddaD (green; n= 10 cells) and ddaE (blue; n= 10 cells) from *221-Gal4, UAS-CD4tdGFP* (2 animals) and *410-Gal4, UAS-CD4tdtomato* (2 animals) during forward crawling. (See Figure 2.7 for changes to dendrite folding and activity in compressed conditions).
(**c**,**d**) Mean (± s.d.) calcium response (solid line) of ddaE and ddaD soma during segment contraction (quantified as the fractional change in the GCaMP / tdTomato fluorescence ratio $\Delta R/R_0$ – see methods). Mean (± s.d.) inter-cell distance is plotted with a dashed line. Maximal contraction is set at 't=0s' for each event. In (**d**), we plotted anterior inter-cell distance between the measured neuron and the homologous neuron in the anterior segment, since this was a better proxy for ddaD dendrite folding. To compare neurons in animals crawling at different speeds, the time window and the amplitude of each trace were normalized and interpolated across events (see methods). (**e)** SCAPE imaging of *GMR10D05-Gal4*, *UAS-CD4tdGFP* larva during crawling showing dorsal cluster dendrite dynamics. **(e´-e´´)** dorsal and side views in which dmd1 soma and dendrite bundle are traced with a dashed yellow line – tracing shown in **e´´´.** dbd noted with arrowhead.
(f) Schematic and inset image showing neurons imaged together in **e**. Inset image shows pseudo-colored neurons. ddaE (blue), ddaD (green), dbd (yellow), dmd1 (pink). Dashed line represents outline of ddaE and ddaD dendritic fields.
(**g**,**h)** Mean (± s.d.) calcium response (solid line) of dmd1 and dbd soma during segment contraction (quantification and representation is same as in **C** above.
(i) SCAPE imaging of *1129-Gal4*, *20XUAS-IVS-GCaMP6f* (x2), *UAS-CD4-tdTomato* larva ventral side during crawling. Yellow box indicates neuron examined in **(i´-i´´)** dorsal and side views.
(j) Mean (± s.d.) calcium response (solid line) of vbd soma during segment contraction (quantification and representation is same as in **C** above).
For (**a, e** and **i**), images show representative SCAPE MIPs over an 80-95 μm depth range from a 160-165μm deep volume (to exclude gut autofluorescence, square root grayscale). See Movie 2.4 for dendrite motion dynamics and Movie 2.5 for GCaMP dynamics related to A, E, and I.
Sample sizes: **c)** 3 animals, n=10 cells, 17 events **d)** 3 animals, n=7 cells, 11 events, (**g&h**) n=4 animals. n=8 cells, 16 events, **j)** n=4 animals. n=14 cells, 14 events.
Figure 2.6 shows GCaMP and tdTomato images and single-neuron GCaMP activity from all genotypes. All ribbons represent s.d.
Posterior is to the left for all images.
Scale bar=100 μm in **a, e, i**, scale bar=50 μm in **a´-a´´, e´-e´´, f, i´-i´´**.

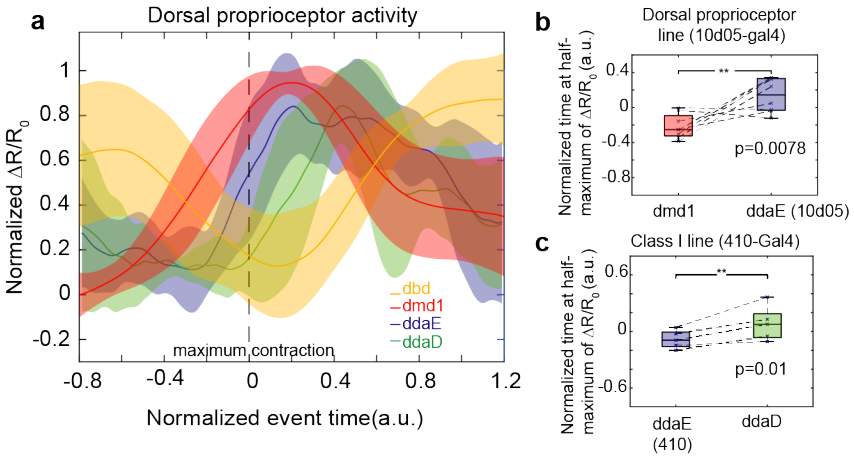

Figure 2.5. Each dorsal proprioceptor type is activated sequentially during segment contraction
(a) Mean calcium response (± s.d.) of dbd, dmd1, ddaE, and ddaD during segment contraction. Dmd1 and dbd data is same as shown in Figure 2.4g-h**.** This plot includes a subset of ddaE and ddaD activity data shown in Figure 2.4c-d from paired cells within a segment (n= 4 animals, 5 cells, 5 events). Data is aligned using time at maximum contraction (as measured by distance between ddaE and homologous ddaE in posterior segment), which is set at 't=0s' for each event. The time window and the amplitude of $\Delta R/R_0$ of each trace were normalized and interpolated across events (see methods).
(b) To test the lag between dmd1 and ddaE activity, we compared the time at half-maximum calcium activity from paired cells within a segment in GMR*10D05-Gal4, 20XUAS-IVS-GCaMP6f* (x2), *UAS-CD4-tdTomato* larva (n=4 animals, n=8 cells, 8 events). ddaE activity occurs significantly later than dmd1 activity (p=.0078) by single-tailed paired t-test.
(c) To test the lag between ddaE and ddaD, we compared the time at half-maximum calcium activity from *410-Gal4, 20XUAS-IVS-GCaMP6f* (x2), *UAS-CD4-tdTomato* animals (n=4 animals, n=5 cells, 5 events). Data are the from the same cell pairs as analyzed in panel **a.** ddaD activity occurs significantly later than ddaE activity (p=0.01) by single-tailed paired t-test.

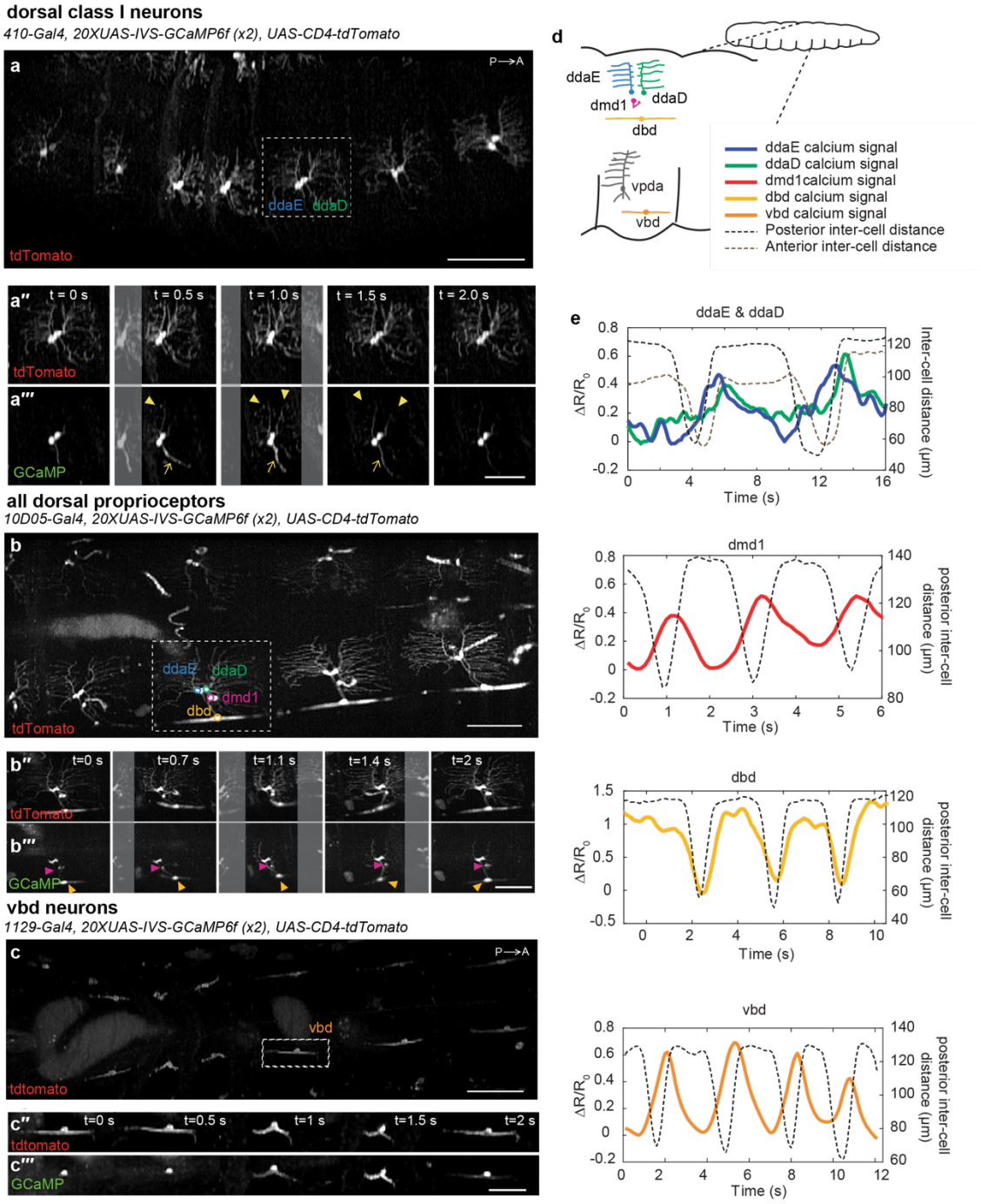

Figure 2.6. Examples of SCAPE imaging of GCaMP dynamics
Posterior is to the left for all images. For (**a-c**), images show representative SCAPE MIPs over a 35-90 μm depth range from a 160-200 deep volume (to exclude gut autofluorescence, square root grayscale). Dashed box indicates neurons examined in time lapse sequences below, shown for both tdTomato and GCaMP channels.
(a-a´´´) SCAPE imaging of *410-Gal4, 20XUAS-IVS-GCaMP6f* (x2), *UAS-CD4-tdTomato* larva. See Movie 2.5, first section. Arrowheads indicate increases in dendritic GCaMP6f, arrows indicate increases in axon bundle (containing both ddaD and ddaE axons). Note ddaE dendrites are active before ddaD.

(b-b´´´) SCAPE imaging of *GMR10D05-Gal4, 20XUAS-IVS-GCaMP6f* (x2), *UAS-CD4-tdTomato* larva. See Movie 2.5, second section. Orange arrowhead marks dbd cell body, pink arrowhead marks dmd1 cell body.
(c-c´´´) SCAPE imaging of *1129-Gal4, 20XUAS-IVS-GCaMP6f* (x2), *UAS-CD4-tdTomato* larva. See Movie 2.5, third section.
(d) Schematic of larval proprioceptive system.
(e) Examples of single cell calcium activity dynamics during forward crawling. The calcium response is plotted in solid lines (quantified as $\Delta R/R_0$). The distance between the measured neuron and the posterior neuron (posterior inter-cell distance) is plotted in black dashed lines. The distance between the measured neuron and the anterior neuron (anterior inter-cell distance) is also plotted in brown dashed lines on the ddaD plot, since this is a better proxy for dendrite folding.

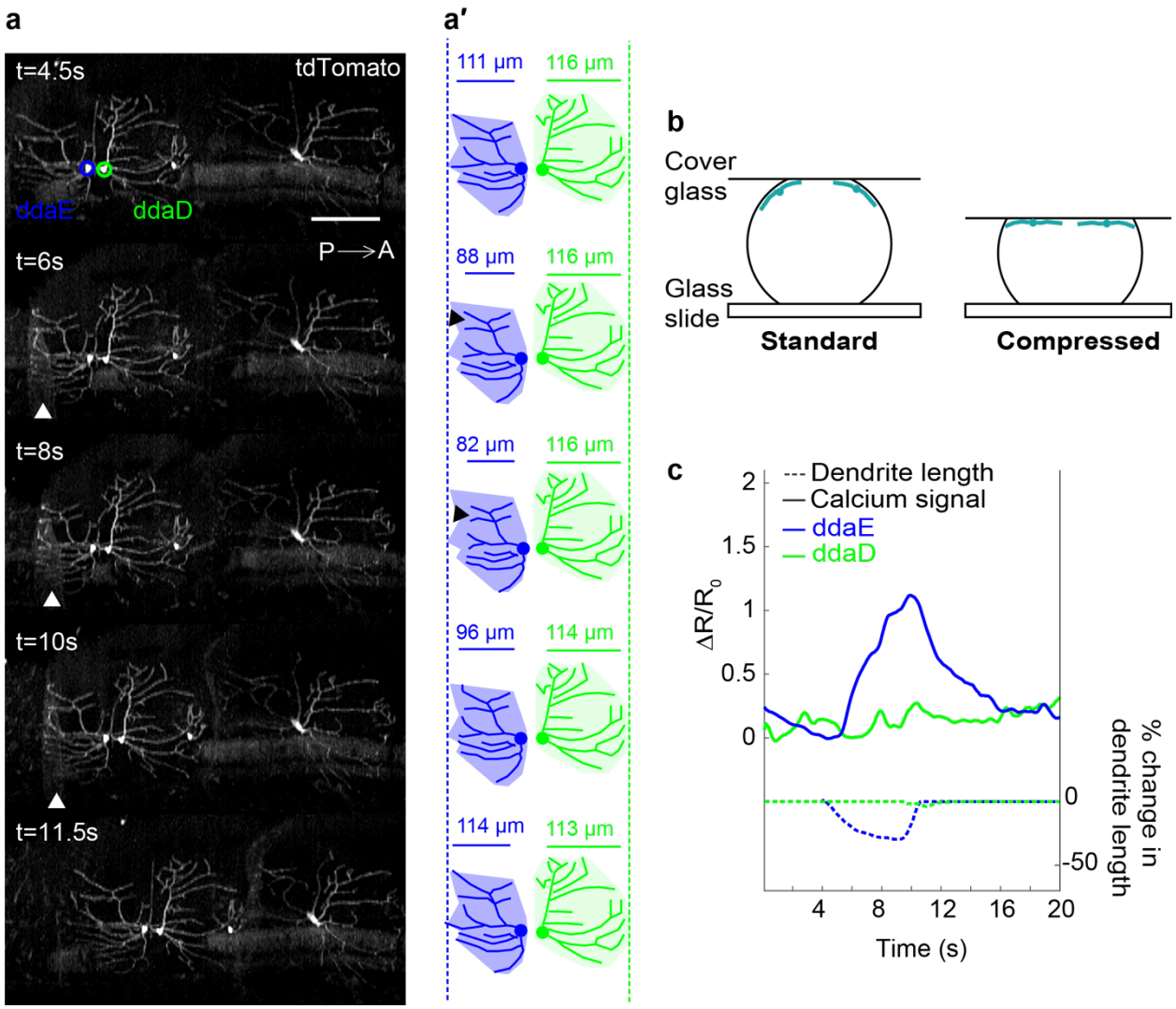

Figure 2.7. Sensory activity does not occur in the absence of dendritic folding
(a) Time lapse of SCAPE imaging of dorsal class I neurons labeled with *410-Gal4, 20XUAS-IVS-GCaMP6f (x2),* UAS-CD4-tdTomato, in a compressed preparation, which prevents dendritic folding in ddaD (see (b) and methods). TdTomato channel is shown to depict dendrite dynamics. Larva is 3rd instar. Posterior is to the left. (MIP) over a 50µm depth range from a 160µm deep volume. (a′) Tracing of time lapse data shown in (a), posterior cells. ddaE is blue and ddaD is green. Dotted lines and shaded areas represent extent of arbor in a relaxed segment. Measurements represent dendrite length (µm), a measure of dendrite folding. Arrows denote frames with dendrite folding. Note that ddaE dendrites fold, but not ddaD.
(b) Schematic of compressed preparation.
(c) Calcium responses (ΔR/R0, solid lines) and % change in dendrite length (dotted lines) in a compressed preparation of ddaE (blue) and ddaD (green) during segment contraction. Activity correlates with dendrite folding. Scale bar=100µm.

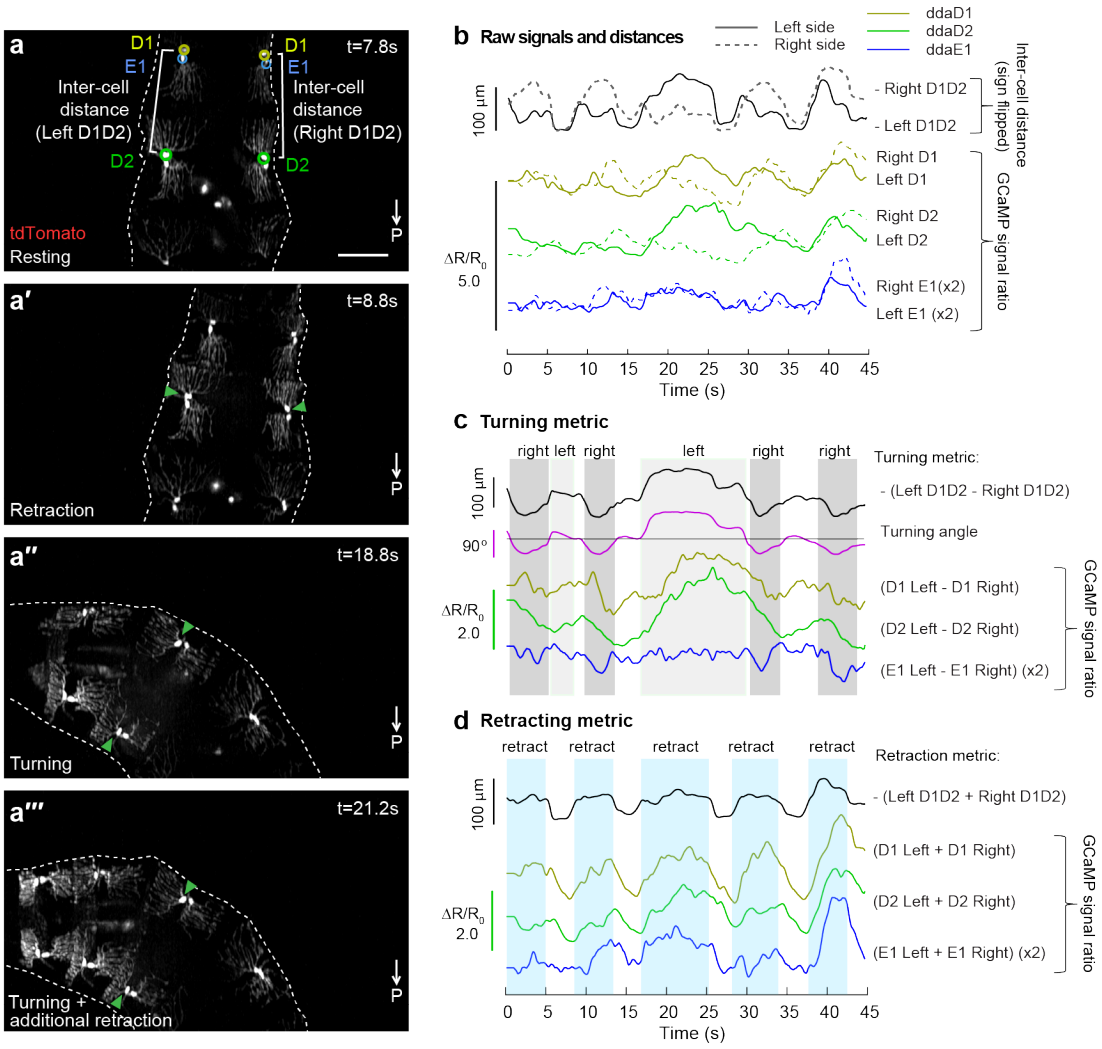

Figure 2.8. Dorsal proprioceptor activity can simultaneously code for head turning and retraction
(a- a´´´) SCAPE imaging of dorsal class I neurons labeled with *410-Gal4, 20XUAS-IVS-GCaMP6f* (x2)*, UAS-CD4-tdTomato*, during exploratory behavior. Posterior is to the bottom of all images. TdTomato channel shown. MIP over an 80µm depth range from a 140µm deep volume (square root grayscale). GCaMP fluorescence was quantified from circled neurons, ddaD (D1, yellow-green) and ddaE (E1, blue) in segment T3, and ddaD (D2, green) in segment A1. Inter-cell distance (white brackets) is quantified as distance between ipsilateral D1 and D2. Representative behaviors are shown including resting **(a)**, retraction only **(a´),** and turning **(a´´- a´´´).** Turning showed different levels of retraction (e.g. **(a´´´)** shows more retraction than **(a´´)**).
(b) Calcium activity (measured as the ratio of GCaMP to tdTomato fluorescence) in left (solid) and right (dashed) D1, D2 and E1 neurons are compared to inter-cell distance (black). The sign is flipped on inter-cell distance measurements, so larger values represent shorter distances. ddaE activity was smaller than ddaD activity, so E1 data is shown at 2X. See Table 2.1 for correlation values.
(c) Plots of the difference in calcium activity between contralateral cells compared to the difference in contralateral inter-cell distances (our turning metric) and the calculated angle of the D1 segment.
(d) Plots of the sum of calcium activity between contralateral cells and the sum of contralateral inter-cell distances (our retraction metric). Movie 2.6 shows this dataset.
Scale bar=100 µm.

Table 2.1. Correlation coefficient values for data in Figure 2.8b-d, time-aligned and with a time-shift
Shifting the neuronal calcium responses in time accounts for the phase lag in signaling compared to maximal contraction, consistent with results shown in Figure 2.5. Lower correlation coefficient values relating to the Right E1 neuron may relate to the more minimal compression of ddaE dendrites (mean dendrite length change during turning or retraction event from resting dendritic length: ddaE=10% ± 6.6% s.d.; ddaD=32% ± 25% s.d.) and the generally smaller amplitude of right-hand turns. The ddaE neuron pair generally appears to be more sensitive to retraction than turning, which explains the relatively similar correlation levels between Right E1 and left and right D1-D2 distances.

	Figure 2.8B					
$\Delta R/R_0$ signal changes:	**Left D1**	**Left D2**	**Left E1**	**Right D1**	**Right D2**	**Right E1**
Left D1D2 inter-cell distance	0.64	0.67	0.6	0.1	-0.08	0.35
Right D1D2 inter-cell distance	0.31	-0.02	0.24	0.66	0.45	0.48
With time-shift (1.2 sec for D1 and 0.45 sec for E):						
Left D1D2 inter-cell distance	0.85	0.86	0.67	0.21	0.09	0.43
Right D1D2 inter-cell distance	0.26	-0.03	0.33	0.86	0.79	0.55
	Figure 2.8C-D					
$\Delta R/R_0$ signal changes:	**D1 Left-Right**	**D2 Left-Right**	**E1 Left-Right**	**D1 Left + Right**	**D2 Left + Right**	**E1 Left + Right**
(Turning metric) Left D1D2 - Right D1D2	0.59	0.64	0.45	-0.2	0.13	0.02
(Retraction metric) Left D1D2 + Right D1D2	-0.01	0.14	-0.28	0.69	0.5	0.57
With time-shift (1.2 sec for D1 and 0.45sec for E):						
(Turning metric) Left D1D2 - Right D1D2	0.82	0.84	0.44	-0.15	0.16	0.01
(Retraction metric) Left D1D2 + Right D1D2	-0.12	0.02	-0.31	0.88	0.81	0.68

Chapter 2 Movie Legends

Movie 2.1. Ventral class I dendrite dynamics during crawling, GFP only, related to Figure 2.1. Class I dendrites (and class IV weakly) are labeled by *221-Gal4, UAS-mCD8::GFP*. Top is ventral view MIP over a 95 µm depth range from a 160µm deep volume, bottom is orthogonal view of ventral class I neuron vpda. Note that dendrites of vpda fold with each peristaltic wave. SCAPE images are shown on a square root grayscale to reduce dynamic range for visualization of both cell bodies and dendrites. Following the real-time movie, the data is played at 4X slower speed. Posterior is to the left. Scale bar=100µm.

Movie 2.2. Tracking of neurons and quantification of GCaMP6f fluorescence during crawling using SCAPE microscopy, related to Figure 2.2. Class I neurons are labeled with *410-Gal4, 20XUAS-IVS-GCaMP6f* (x2), *UAS-CD4-tdTomato*. Top panels show five tracked vpda neurons each on left and right of larva. Solid line indicates GCaMP fluorescence (measured as $\Delta R/R_0$) and dashed lines indicate distance between tracked cell and posterior cell (inter-cell distance). Middle panels depict dual channel SCAPE imaging of a crawling larva (ventral MIP from full 168µm deep imaging volume and an orthogonal MIP view, square root colorscale). CNS is observed at right margin of the movie. Bottom panel is the positions of 12 tracked neurons in 3D space. Posterior is to the left. Scale bar=100µm.

Movie 2.3. Ventral class I (vpda) GCaMP dynamics during crawling, related to Figure 2.2. Vpda neurons are labeled with *410-Gal4, 20XUAS-IVS-GCaMP6f* (x2), *UAS-CD4-tdTomato*. Ventral view MIP over a 85 µm depth range of a 153µm deep volume to exclude gut autofluorescence (square root colorscale). Top panel is tdTomato fluorescence, middle panel is green GCaMP6f fluorescence and the bottom panel is the channel merge. Posterior is to the left. Scale bar=100µm.

Movie 2.4. Dendrite dynamics of dorsal class I (ddaE, ddaD), dbd, dmd1 and vbd during crawling, GFP/tdTomato only, related to Figure 2.4. Three different imaging acquisitions are shown in sequence. In the first movie, class I dendrites (and class IV weakly) are labeled by *221-Gal4, UAS-mCD8::GFP*. In the second movie, dbd, dmd1, ddaE, and ddaD neurons are labeled by *GMR10D05-Gal4, 20XUAS-mCD8::GFP*. In the third movie, the previous real-time movie is played at 4X slower speed. In the fourth movie, vbd neurons are labeled by *1129-Gal4, UAS-CD4-tdTomato.* For all movies, top is dorsal view MIP over a 80-95µm range from a 160-165µm deep volume to exclude gut autofluorescence and bottom is side view (square root grayscale). Posterior is to the left. - Scale bar=100µm.

Movie 2.5. GCaMP dynamics of dorsal class I (ddaE, ddaD), dbd, dmd1 and vbd during crawling, related to Figure 2.4 and Figure 2.6. Three different imaging acquisitions are shown in sequence. In the first movie, class I neurons are labeled with *410-Gal4, 20XUAS-IVS-GCaMP6f (x2), UAS-CD4-tdTomato*. In the second movie, dorsal cluster proprioceptors are labeled with *GMR10D05-Gal4, 20XUAS-IVS-GCaMP6f (x2), UAS-CD4-tdTomato*. In the third movie, vbd neurons are labeled by *1129-Gal4, 20XUAS-IVS-GCaMP6f (x2), UAS-CD4-tdTomato*. All movies show a dorsal view MIP over a 35µm, 100µm, or 80 µm depth range (respectively) of a 160-200µm deep volume to exclude gut autofluorescence (square root colorscale). Top panel is tdTomato fluorescence, middle panel is GCaMP6f fluorescence and the bottom panel is the channel merge. Posterior is to the left. Scale bar=100µm.

Movie 2.6. Dorsal class I GCaMP dynamics during head exploration behavior, related to Figure 2.8. Class I neurons are labeled with *410-Gal4, 20XUAS-IVS-GCaMP6f (x2), UAS-CD4-tdTomato*. Dorsal view MIP over an 80µm depth range of a 140 µm deep volume to exclude gut autofluorescence (square root colorscale). Top panel is tdTomato fluorescence, middle panel is GCaMP6f fluorescence and the bottom panel is the channel merge. In the second movie, both ddaD and ddaE neurons from T3 and A1 segment are marked as dots and their GCaMP-tdTomato ratio is color coded to indicate the neuron activity. The distance between two ddaD neurons in each side is also color coded as (red = compression, blue = rest). The trailing spots show prior positions of each neurons and their GCaMP levels. For all movies, posterior is to the bottom. Scale bars=100µm.

Chapter 3. Investigating the patterning and function of sensory dendrite boundaries

This chapter is partially adapted from a manuscript in progress. I am grateful to many lab members for their valuable contributions to the data and text of this chapter. Aditi Singhania contributed to anatomical and ablation studies. Samantha Galindo, Katherine L Lee, and Nathan Carpenter contributed to the ablation studies. Ya-Ting Lei contributed to the compartment expansion experiments, and Wenze Li contributed to the SCAPE imaging.

Introduction

Sensory neuron function depends critically on the shape, size, and territory of dendritic fields. The *Drosophila* somatosensory system is a good model for studying dendritic development and sensory function, because the neurons are easily genetically manipulated and assessable for in vivo imaging, and each sensory neuron can be uniquely identified by its morphology and position. The dendritic arborization (da) neurons have been an especially useful model for revealing important mechanisms of dendrite territory patterning (Grueber & Sagasti 2010, Singhania & Grueber 2014). Da neurons form a stereotyped arrangement of dendritic arbors across the larval body wall, and are divided into four classes (class I-IV) based on dendritic branching patterns (Fig. 3.1a) (Grueber et al 2002). Dendrites from like-type neurons cover the body wall without overlap, which is termed tiling (Grueber et al 2002, Grueber et al 2003b). Tiling allows for non-redundant coverage of cells with the same function. Furthermore, dendrites from heterotypic neurons generally co-exist freely, facilitating multimodal sensing from the same body wall region (Grueber & Sagasti 2010).

Each of the four classes of da neurons has a different function, and the dendrites of each neuron type show distinct patterns of body wall coverage (Fig. 3.1a-d). Class I (cI) neurons are proprioceptive and cover specific, limited portions of the body wall (Fig. 3.1c), class III (and likely class II) neurons are touch-sensing and show intermediate coverage (Fig. 3.1d), and class

IV (cIV) neurons are nociceptive and cover the entire body wall (Fig. 3.1b) (Grueber et al 2002, Singhania & Grueber 2014).

Previous work has shown that cIV dendrite tiling across the entire body wall is due to homotypic dendrite-dendrite interactions, as ablation of a cIV neuron during development causes growth of neighboring neuron dendrites (Grueber et al 2003b). This is an efficient method to guarantee complete and non-redundant coverage of cIV dendrites. This complete coverage is likely to support cIV function as nociceptors, as it is likely beneficial to sense pain on every part of the body. By contrast, dendrite coverage of cI and cII neurons is quite selective (Fig. 3.1c), and cIII neurons do show homotypic tiling, but body wall coverage is incomplete and stereotyped regions lack coverage (Fig. 3.1d) (Grueber et al 2002, Grueber et al 2003b). It is largely unknown how sensory dendrite territories establish coverage in selective locations on the body, and how this coverage supports their sensory function.

To explore potential mechanisms that pattern selective dendrite coverage, previous members of the Grueber lab analyzed the frequency of tiling and co-existence between each class of da neuron, using a FLP-out system to resolve different arbors simultaneously (Fig. 3.1e-i). They showed that homotypic dendrites show avoidance, while heterotypic arbors usually overlap (Fig. 3.1e, h), which is consistent with earlier results (Grueber & Sagasti 2010). Notably, they also revealed that select pairs of heterotypic neurons did not show dendrite crossing, even though their arbors were in neighboring territories (Fig. 3.1i) [subset of this data also previously reported in (Singhania 2014)]. Most cI-cII pairs showed dendrite avoidance (Fig. 3.1f, i), as did the ventral cI-cIII pair vpda and vdaD (Fig. 3.1g, i), indicating heterotypic tiling between proprioceptive (cI) and many touch-sensing (cII-cIII) neurons.

How are these tiling boundaries formed between heterotypic neurons? One possibility is that there are repulsive interactions between proprioceptive and specific touch-sensing dendrites. To explore this idea, a previous student examined cIII vdaD arbors in animals with genetic ablation of cI vpda cells due to a mutation in the *atonal (ato)* transcription factor (Singhania 2014). Class III vdaD dendrites did not grow into the territory usually occupied by vpda, suggesting that dendrite interactions are not required for setting the boundaries of cIII territories in the ventral cluster. However, these experiments did not confirm the loss of vpda, which could confound the results. Furthermore, these experiments did not evaluate the effect of vpda ablation on cII dendrite boundaries, or the effect of cII/cIII ablation on vpda territories, leaving open the possibility that repulsive interactions between dendrites are important.

Alternatively, dendrites could have class-specific responses to cues within the epidermal substrate. Da dendrites are closely associated with the epidermis and the extracellular matrix (ECM), suggesting dendrites could respond to epidermal cues (Han et al 2012, Kim et al 2012). To explore this idea, previous members of the Grueber lab looked at the relationship between ventral cI-cIII dendrites and major epidermal compartmental cues (Singhania 2014). Early in development, before sensory dendrite patterning, each segment of the body wall is divided into a Posterior (P) compartment and an Anterior (A) compartment. The P compartment is defined by expression of the Engrailed (En) transcription factor and secretes Hedgehog (Hh). Hh then binds to the Patched receptor (Ptc) in the A compartment, causing the release of Wingless (Wg), which works in a loop to maintain Engrailed expression and the A-P compartment boundary (see Chapter 1, Fig. 1.3) [reviewed in (Sanson 2001)].

Interestingly, ventral dendrite boundaries correlate with these compartments [data initially reported in (Singhania 2014), reproduced here in Fig. 3.2a-d]. Ventral cII (vdaC) and

cIII vdaD touch-sensing dendrites avoid the P compartment (Fig. 3.2a-b, d). In contrast, the primary dendrite of the cI vpda proprioceptive neuron grows along the A-P compartment boundary, while the secondary dendrites are biased to grow within the P compartment (Fig. 3.2c). Furthermore, the anterior-oriented secondary dendrites are contained within the sub-domain of the A compartment expressing *ptc* (Fig. 3.2e). These correlations (summarized Fig. 3.2f) suggest that ventral dendrite boundaries could be patterned by compartmental epidermal cues.

In this chapter, we investigate the contribution of dendrite-dendrite repulsion and epidermal compartment cues to the patterning of proprioceptive and touch-sensing dendrite boundaries. Furthermore, we use live imaging techniques to investigate the possible relevance of this organization for proprioceptive and touch-sensing function.

Results

Major dendrite boundaries are not patterned by dendrite-dendrite interactions

To test whether interactions between neighboring dendrites are responsible for the heterotypic tiling between proprioceptive and touch-sensing neurons, we expanded upon previous results and performed a series of cell ablation experiments (Fig. 3.3). We performed laser ablations of cII vdaC and cIII vdaD neurons, and then quantified changes in cI vpda dendrite territory coverage (quantification method depicted in Fig. 3.3b). Figure 3.3c depicts alternative outcomes for vpda after cII-cIII ablation: if there is dendrite-dendrite repulsion, vpda dendrites should grow into the territory previously occupied by cII-cIII cells (Fig. 3.3ci), while if there is no repulsion (or a redundant mechanism), there will be no expansion of vpda territories (Fig. 3.3cii). Our results suggest dendritic interactions are not required for vpda territory

patterning, as there was no significant expansion of vpda territories after cII-cIII ablations (Fig. 3.3d).

Conversely, we genetically ablated vpda with *ato* mutants and examined cIII vdaD and cII vdaC territories (see Fig. 3.3e for model of alternative outcomes). As an improvement on previous experiments (Singhania 2014), lack of vpda was confirmed with HRP staining for all analyzed segments. We analyzed cIII dendrites (labeled with *NompC-Gal4, UAS-CD4::tdTomato)* in *ato* mutant animals and controls, and found no significant expansion of vdaD territories into the region normally containing vpda (Fig. 3.3f-h). Occasionally, single vdaD dendrites extended into the vpda region (Fig. 3.3g′), but overall the boundary was maintained, as assessed by a modified Sholl analysis (Fig. 3.3h). These results are consistent with what was previously reported (Singhania 2014). To examine cII (vdaC) territories in *ato* mutant animals and controls, we labeled cII dendrites with *1112-Gal4, UAS-CD4::tdGFP*. Similarly, we found no expansion of vdaC territories into the region normally containing vpda (Fig. 3.3i-k, $p>0.30$ at all intervals after the compartment boundary). These results indicate that dendrite-dendrite interactions are not required for setting the boundaries of cII and cIII territories in the ventral cluster.

Altogether, our results suggest that, unlike homotypic tiling, heterotypic tiling does not require repulsive interactions between neighboring dendrites, suggesting that major dendrite boundaries of cI, cII, and cIII neurons are patterned by other cues.

Compartmentalized epidermal cues instruct proprioceptive dendrite targeting

As an alternative to repulsive dendrite-dendrite interactions, cues in the epidermal substrate could instruct sensory dendrite boundaries. Supporting this idea, dendrite boundaries

correlate with A and P compartment boundaries in the epidermis: ventral touch-sensing cII/cIII neurons avoid the P compartment, while ventral cI proprioceptive dendrites are biased to grow within the P compartment (Fig 3.2). This correlation suggests that dendrite boundaries could be patterned by compartmental epidermal cues.

To test whether compartmentalized cues in the epidermis are instructive for dendrite targeting, we used a genetic method to artificially expand the P compartment in the posterior direction (Fig. 3.4). If compartment cues are instructive, expanding the P compartment could lead to expansion of the posterior-oriented vpda dendrites. Since the P compartment is expanding in the posterior direction with our manipulation, we would not expect a change to the cII or cIII dendrites at the A-P boundary. The P compartment can be expanded by overexpressing Wg in the *engrailed* domain, as Wg helps to maintain Engrailed expression [reviewed in (Sanson 2001)}. Indeed, *en-Gal4, UAS-mCD8::GFP > UAS-wg^{741}* leads to a significant expansion of P compartment length (Fig. 3.4c; ***p<0.001) and a significant expansion of the average length of vpda posterior-oriented dendrites (Fig. 3.4d; **p=0.006). These results support a model in which there are instructive cues within the P compartment that target cI dendrites.

Exploring the potential functional relevance of selective dendrite coverage

What is the functional relevance of the targeting of ventral cI proprioceptive dendrites to the P compartment? Is there also a functional role for cII/cIII touch-sensing neurons to avoid this region? To begin to investigate these questions, we used Swept, Confocally-Aligned Planar Excitation (SCAPE) microscopy (Bouchard et al 2015, Voleti et al 2019) to image the dynamics of the body wall during crawling. Since cI proprioceptive neurons respond to segment contraction [see Chapter 2 and (Vaadia et al 2019)], we predicted that we would see cuticle

folding in the P compartment during crawling. Indeed, we found that the ventral P compartment is a robust marker for where the cuticle folds during crawling (Fig. 3.5). The dynamics are most easily discerned in the orthogonal view (Fig. 3.5c-c′). In relaxed segments, the P compartment is flat (Fig. 3.5c). In contracted segments, the P compartment folds up into the animal at a 90-degree angle (Fig. 3.5c′), indicating a major fold at the A-P compartment boundary. These dynamics were consistent across animals (quantified in Fig. 3.5d) and are consistent with the vpda dendrite dynamics described in Chapter 2 (reproduced again here in Fig. 3.5b). These results suggest that class I proprioceptor targeting to the P compartment positions cells to detect major cuticle folding during locomotion.

Furthermore, the restriction of touch-sensing cII-cIII neurons from the P compartment could tune these cells for external mechanosensory stimuli rather than self-generated movement. To test this idea, we used dual-color SCAPE imaging to monitor dynamics of both the P compartment (magenta) and A compartment (green) simultaneously (Fig. 3.5g-h″). While the P compartment folds severely at a 90-degree angle (Fig. 3.5h′, arrowheads), the A compartment is more stable, showing accordion-like compression a few microns from the A-P compartment boundary (Fig. 3.5h′, arrows). Altogether, these results support the idea that dendrite targeting by compartmental substrate cues reliably tunes neurons for predictable stimuli on the body wall. cI dendrites target areas that bend severely and predictably during crawling, and cII and cII could be avoiding those areas to be tuned for external mechanosensory stimuli instead.

Examining the sensory organization and dynamics of the dorsal body wall

So far, the described work has focused on the ventral body wall. How generalizable are compartmental dendrite organization and body wall dynamics to other areas of the larval body?

To explore this question, we characterized the relationship between dorsal cI, cII, cIII dendrites and the epidermal compartments (Fig. 3.6). Class II neurons show the most consistent organization, as all dorsal and ventral cII neurons avoid the P compartment (Fig. 3.6b), suggesting a general principle for cII organization. For cI neurons, most (2/3) are targeted to the P compartment. For the two cI neurons (ddaE, ddaD) on the dorsal side of the body wall, ddaE looks very similar to vpda, as its dendrites mainly grow within the P compartment, while ddaD dendrites are contained within the A compartment (Fig. 3.6a). For class III neurons, only the ventral neuron vdaD avoids the P compartment. The dorsal neurons ddaF and ddaA grow freely within the P compartment (Fig. 3.6c), as does the ventral prime cIII cell v′pda.

The differences between ventral and dorsal dendrite organization could potentially be related to differences in body wall dynamics. When we imaged the P compartment of the dorsal body wall (Fig. 3.5e-f), contracted segments showed the domain compressed along the AP axis, in contrast with the major 90-degree fold at the A-P compartment boundary seen on the ventral side. We can speculate that these different body wall dynamics do not require avoidance of the cIII neurons for their sensory tuning. Future work could follow up on these ideas with more extensive live imaging of the entire dorsal body wall and cIII dendrite dynamics.

Discussion

In this chapter, I explore how cI-cIII dendrite territories establish coverage in the proper location on the larval body, and how this coverage supports their sensory function. Previous work in the Grueber lab revealed that cI proprioceptive neurons often tile with cII or cIII touch-sensing neurons, most notably in the ventral cluster. In contrast to prior studies of homotypic tiling of cIV da neurons (Grueber et al 2003b), our ablation studies indicate that these heterotypic

dendrite boundaries do not rely on repulsive interactions between neighboring dendrites. Instead, our evidence suggests that compartmentalized epidermal cues instruct dendrite targeting. In the ventral cluster, cII-III dendrites avoid the P compartment, while cI dendrites are biased to grow within the P compartment. Genetic expansion of the P compartment leads to expansion of the ventral cI dendrites, suggesting that cues within the compartment are instructive for proprioceptor targeting.

A similar compartmental organization is observed for the dendrites of larval motor neurons in the CNS (Landgraf et al 2003). Dendrites of motor neurons that project to internal muscles are restricted to in the *engrailed* domain of the CNS, whereas dendrites of motor neurons that project to external muscles arborize in a complementary region. Similar to what we observed with da neurons, this organization is not due to repulsive interactions between neighboring dendrites (Landgraf et al 2003). The identity of the cues that drive motor and sensory dendrite boundary formation are unknown. Compartments are also an important feature of vertebrate tissues, including the limb bud and hindbrain (Blair 1997, Kiecker & Lumsden 2005). Therefore, mechanisms of compartment organization of the nervous system in *Drosophila* could be relevant to a wide range of systems for linking nervous system patterning with the body plan. In Chapter 4 of this thesis, I discuss experiments performed to dissect the role of various substrate cues in regulating the compartmental organization of sensory dendrites.

What is the functional relevance of this compartment organization? SCAPE imaging revealed that on the ventral side, the P compartment is a robust marker for a major cuticle fold that occurs during crawling, consistent with the idea that proprioceptive cI dendrites are targeted to this region to be tuned for proprioceptive stimuli. Specifically, a major fold occurs right at the A-P compartment boundary during segment contraction. Vpda primary dendrites grow along the

A-P boundary and secondary dendrites span this fold, which precisely positions these cells to respond to contraction during locomotion, as observed in Chapter 2.

Altogether, our data supports a model in which dendrite targeting by compartmental substrate cues might reliably tune neurons for predictable stimuli on the body wall. CI dendrites target areas that bend predictably during crawling, and we can speculate that the avoidance of cII and cIII dendrites from these areas is important for tuning these cells for external mechanosensory stimuli instead. In the future, if we find genetic manipulations that can expand proprioceptive or touch-sensing dendrites into inappropriate regions, we could evaluate if and how these changes in dendrite territories affect sensory function.

While this study focused on testing the contribution of dendrite-dendrite and dendrite-substrate interactions for sensory dendrite patterning, future experiments should evaluate the contribution of activity-dependent mechanisms. Late stage *Drosophila* embryos show peristaltic movements at ~18 hours after egg lay (AEL), which is about 3-4 hours before hatching (Crisp et al 2008). Therefore, we cannot exclude the possibility that cII and cIII dendrites grow into the P compartment at earlier stages, and then are pruned to avoid the compartment via activity-dependent mechanisms in response to body wall movements. To test this model, future experiments should prevent embryo movement and evaluate the boundary of cII and cIII dendrites.

While the preferential bending of the P compartment is likely controlled at least partially by muscle anatomy and activity, the composition of the cuticle could also be a major determinant. The epidermis secretes a cuticle that functions as an exoskeleton, and different cuticle areas have different protein compositions and physical properties (Moussian 2010, Wong et al 2012). Preferential distortion of the P compartment could be due to a specialized protein

composition that modulates the physical properties of the cuticle. Future work could investigate compartmental differences in cuticle protein expression and the effect of these proteins on cuticle physical properties. Compartmental organization of both dendrites and cuticle composition could be an efficient mechanism to coordinate the patterning of sensory dendrite territories with the development of the appropriate properties of the underlying substrate that modulate sensory responses.

Methods

Animals

All stocks were obtained from the Bloomington Drosophila Stock Center unless otherwise noted. For visualizing and manipulating da neurons we used *109(2)80 Gal4, UAS-mCD8::GFP* as a pan-da neuron marker; *221-Gal4>20XUAS-mCD8::GFP* to label class I neurons; *1112-Gal4, UAS-CD4::tdGFP* to label cII neurons; and *NompC-Gal4>UAS-CD4::tdTomato* or *>20XUAS-mCD8::GFP* to label cIII neurons. We used *hsFlp; 109(2)80-Gal4, en-lacZ, UAS<CD2<CD8::GFP* to mark individual da neurons together with the P compartment. To perform genetic ablations of cI neurons we used $ato^{1/}$ $ato^{[y+]}$. For the compartment expansion experiments, we used *en-gal4>UAS-mCD8::GFP* crossed with *UAS-wg-741* (Gift from Dr. Gary Struhl) or with w^{1118} for controls. To label the epidermal compartments during SCAPE imaging, we used *en-Gal4, UAS-mCD8::GFP* or *en-Gal4, UAS-mCD8::mcherry; 871-QF, QUAS-mCD8::GFP*.

Immunohistochemistry

Third instar larvae were pinned at their anterior and posterior ends in Sylgard dishes filled with 1X PBS and cut along the dorsal midline. For analysis of *ato* larvae size matched third-instar larvae were used to compare experimental and control animals. Larvae were pinned flat, fixed in 4% paraformaldehyde (Electron Microscopy Sciences) in PBS for 15 minutes with gentle shaking, and transferred to 5 ml rounded tubes and rinsed for 3x5 minutes in PBS + 0.3% Triton X-100 (PBS-TX). Tissue was blocked for 1 hour at 4°C in 5% normal donkey serum (Jackson ImmunoResearch, West Grove, PA), then incubated overnight in primary antibodies in PBS-TX. The following primary antibodies were used: Rabbit anti-dsRed (1:200, Clontech), goat anti-HRP (1:200 and 1:1000, Jackson ImmunoResearch 123-005-021 and 123-001-021, respectively), chicken anti-GFP (1:1000-1:2000, Abcam, Cambridge, MA), mouse anti-GFP (1:250, Molecular Probes/Invitrogen, Carlsbad, CA), mouse anti-22C10 (1:100, developed by S. Benzer and distributed by Developmental Studies Hybridoma Bank [DSHB], Iowa City, IA), mouse anti-CD2 (1:250, abD Serotec), rat anti-CD8 (1:100, Cappel), mouse anti-βgal (1:10, DSHB) and rabbit anti-βgal (1:1000, Cappel). Tissue was rinsed at least for at least 1 hour with 3 changes of PBS-TX and incubated in secondary antibodies for 24-48 hours at 4°C. Rhodamine Red-X, FITC, Alexa Fluor 647, Alexa Fluor 488, Cy2, and Cy5-conjugated secondary antibodies were used against the appropriate species (1:200; Jackson ImmunoResearch). Tissue was mounted on poly-L-lysine coated coverslips and dehydrated in ethanol series (30%, 50%, 70%, 95%, 100%, 100%), each for 3-5 minutes, cleared in xylenes (2 x 10 minutes), and mounted in DPX (Fluka, Sigma-Aldrich).

Cell ablations

To perform laser ablations of cII and cIII neurons we used *109(2)80 Gal4, UAS mCD8::GFP*. Embryos were grown to stage 16-17 at 25°C, and dechorionated in 50% bleach for 2 minutes. They were aligned on grape agar dorsal side up, and then transferred and affixed to a coverslip with double-sided tape. The embryos were mounted in halocarbon oil 700. The coverslip was secured to a slide using a drop of halocarbon oil 700, and a #0 coverslip was placed on top of the embryos. Cell ablation experiments were performed using the MicroPoint Laser Illumination & Ablation system (Photonic). The power was adjusted in order to ablate the cell with approximately 30-60 seconds of pulses. The slide was placed in a petri dish and submerged in halocarbon oil 27. The #0 coverslip was removed. The animals recovered at room temperature, were transferred to a vial of food, grown to the third instar stage at 25°C and then dissected and labeled.

Confocal image acquisition and processing

Static images were acquired on a Zeiss 510 Meta confocal microscope using 40X Plan Neofluar 1.3 N.A., or on a Zeiss LSM 700 confocal microscope using a 25X glycerol-immersion lens. Confocal images were processed in Photoshop CS3 or CS6, Illustrator 6 (Adobe Systems), Zeiss confocal software (Carl Zeiss, Germany), or Fiji.

Heterotypic tiling ablation experiment image analysis

Quantification was performed using Adobe Illustrator and Fiji, and sometimes with Neurolucida and Neurolucida Explorer (MBF Bioscience). To analyze cII and cIII dendrite boundaries in *ato* and control larvae, the absence of vpda in *ato* mutant larvae was confirmed with HRP and/or

22C10 labeling. For cIII neurons, 15 control and 15 experimental vdaD neurons were selected from segments A2-A6. For cII neurons, 7 control and 7 experimental vdaC neurons were selected from segments A2-A6 from at least 6 different animals. The region between the first proximal branch point and the anterior-most edge of the denticle belt was selected for analysis. This region was divided into 10 equal intervals, with 1 being the first interval after the proximal dendrite branch and 10 being the start of the denticle belt. If dendrites extended past the denticle belt, additional intervals were added as needed. Intervals were examined rather than absolute distance to control for any differences in animal size. Dendrite crossings at each interval were counted. For each interval, crossings were divided by total # of dendrite crossings of posteriorly-oriented dendrites to give % of total branch crossings (of posteriorly-oriented dendrites) at each interval. To analyze cI dendrites in cII/cIII laser ablated animals and controls, we used the method as outlined in (Singhania 2014), method quoted below:

> *The primary dendrite was traced using Photoshop CS3. This tracing was placed at 10 µm distances from the primary dendrite across the entire dendritic field anterior and posterior to the primary dendrite was covered. Dendrite crossings at each of the 10 µm tracings were recorded. The sum of dendrite crossing was computed and the ratio of the number of dendrite crossings at each of the 10 µm distance to the total number of dendrites was calculated.*

Compartment expansion image analysis

12 vpda neurons from *en-Gal4, UAS-mCD8::GFP x UAS-wg-741* animals and 10 neurons from controls (*en-Gal4, UAS-mCD8::GFP x* w^{1118}*)* were selected from segments A2-A5. Each analyzed neuron was from a different individual larva. Genotype was blinded during quantification. Quantification was performed using Fiji. Estimated P compartment length was measured by drawing a rectangle around the P compartment, approximately the width of the

primary dendrite length. The area of this rectangle was divided by the width of the rectangle to acquire an estimated length of the P compartment in the vpda region. This length was normalized by the estimated length of the entire segment (which was measured in the same manner as the estimated P compartment length) to control for variably in animal size. Each vpda dendrite was traced in Fiji using the ROI tool and then measured. Average posterior dendrite length was calculated as the sum of all posterior-oriented secondary dendrites, divided by the total number of posterior-oriented secondary dendrites.

SCAPE Image acquisition and analysis

High-speed volumetric imaging of crawling larvae was performed using a custom swept confocally aligned planar excitation (SCAPE) microscope extended from designs described in (Bouchard et al 2015, Voleti et al 2019). The system's stationary objective was configured in an inverted arrangement for the ventral side imaging and an upright arrangement for the dorsal side imaging. Dual-color imaging was achieved using a custom-built or Photometric DV2 dual color image splitter in front of the sCMOS camera. 488 nm excitation (<5 mW at the sample) was used to excited fluorescence in both channels, with 525/45 nm and 630/50 nm emission filters in the green and red emission channels respectively. The system's camera frame rate to read 150-200 rows (corresponding to oblique depths along z') was 1000-1300Hz, with an x- scanning step size of ~2μm to achieve 10 volumes per second imaging over a field of view of 1000 x 250 x 195 μm (y-x-z)(scan parameters varied for different trials, based on the size difference of each larva).

1st and 2nd instar larvae were chosen to image multiple segments at once. Larvae were imaged while positioned within a 300 μm channel made from two 150 μm thick FEP sheets. Each trial

acquired data for up to 120 seconds or was terminated earlier if the larva crawled to the end of the channel. A translation stage along the FEP channel axis was used to keep the larva in the field of view during the acquisition as needed.

For SCAPE imaging visualization, the raw camera 16bit data was square root scaled for visualization to enhance the visible dynamic range for both figures and movies, in order to avoid display saturation and have all the components visible. Resulting pixel values are then shown on a linear gray, red or green colorscale without further adjustment. Images and movies were generated using Matlab and ImageJ.

Statistical methods

Statistical tests and data plotting were performed using Microsoft Excel, RStudio, and Prism 7. Compartment expansion experiments were evaluated by a two-tailed Student's t-Test with two-sample unequal variance. Modified Sholl analysis for cII dendrites in *ato* mutatns was evaluated by a Repeated-Measured ANOVA with post-hoc Sidak's multiple comparisons test for each interval. P-values are represented as: * < 0.05, ** < 0.01, and *** < 0.001.

Chapter 3 Figures

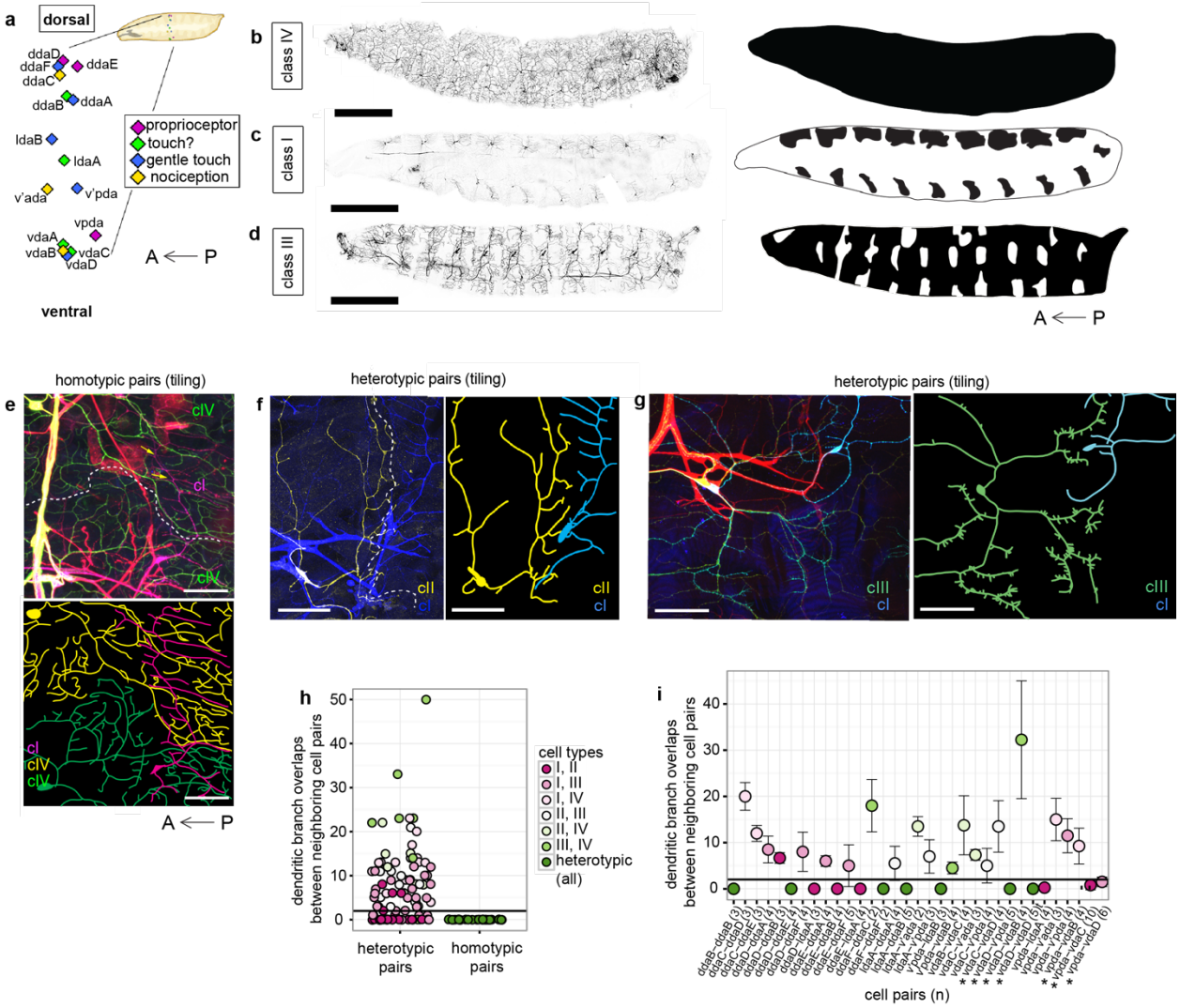

Figure 3.1. Analysis of dendritic tiling and co-existence in da neurons
(a) Schematic of the dendritic arborization (da) neuron cell body positions in the PNS of Drosophila embryos and larvae. Neurons belonging to the same class are shaded the same color.
(b) Whole animal confocal montage of cIV dendrite fields in second instar larva (left). Shading of regions of the body wall that are covered by dendrite of class IV neurons (right). cIV dendrites together cover all of the larval surface.
(c) Whole animal confocal montage of cI dendrite fields labeled by *221-Gal4, UAS-mCD8::GFP* in second instar larva (left). Shading of regions of the body wall that are covered by dendrites of class I neurons (right). cI dendrites collectively cover very selective regions of the body wall.
(d) Whole animal confocal montage of cIII dendrite fields labeled by *NompC-QF, QUAS-CD4:tdTomato* in second instar larva (left). Shading of regions of the body wall that are covered by dendrite of class III neurons (right). cIII dendrites together cover most of the larval surface, but specific regions lack coverage (white regions).
(e) FLP-out labeling of da neurons with cIV neurons labeled by anti-GFP and other neurons labeled by anti-CD2. cIV dendrites show tiling (homotypic avoidance; dashed line) but overlap with cI dendrites (co-existence). Tracing

(bottom) shows cIV neurons in green and yellow and cI neuron in magenta.
(f) FLP-out labeling (right) and tracing (left) of heterotypic tiling pair vdaC (cII, yellow) and vpda (cI, blue) showing heterotypic tiling.
(g) FLP-out labeling (right) and tracing (left) of heterotypic tiling pair vdaD (cIII, green) and vpda (cI, blue).
(h) Quantification of overlaps between different classes of da neurons, separated by heterotypic and homotypic identity. Cell pairs are color coded according to legend at right. Homotypic pairs include class I (cI), cII, and cIII pairs. Horizontal line indicates cell pairs that show fewer than two dendritic overlaps.
(i) Quantification of overlaps between specific neuron pairs. Shown are mean ± S.D. for each cell pair examined. The specific neuron pair is indicated on the x-axis and the number of observations is in parentheses. Identity of cell pairs is color coded according to legend at left. All homotypic pairs and select pairs of cI-cII and cI-cIII neurons show few overlaps. A subset of this data marked by asterisks was initially reported in (Singhania, 2014).
Anterior is to the left and dorsal is to the top in all images.
Scale bars = 500 μm (b-d); 50 μm (e-g)

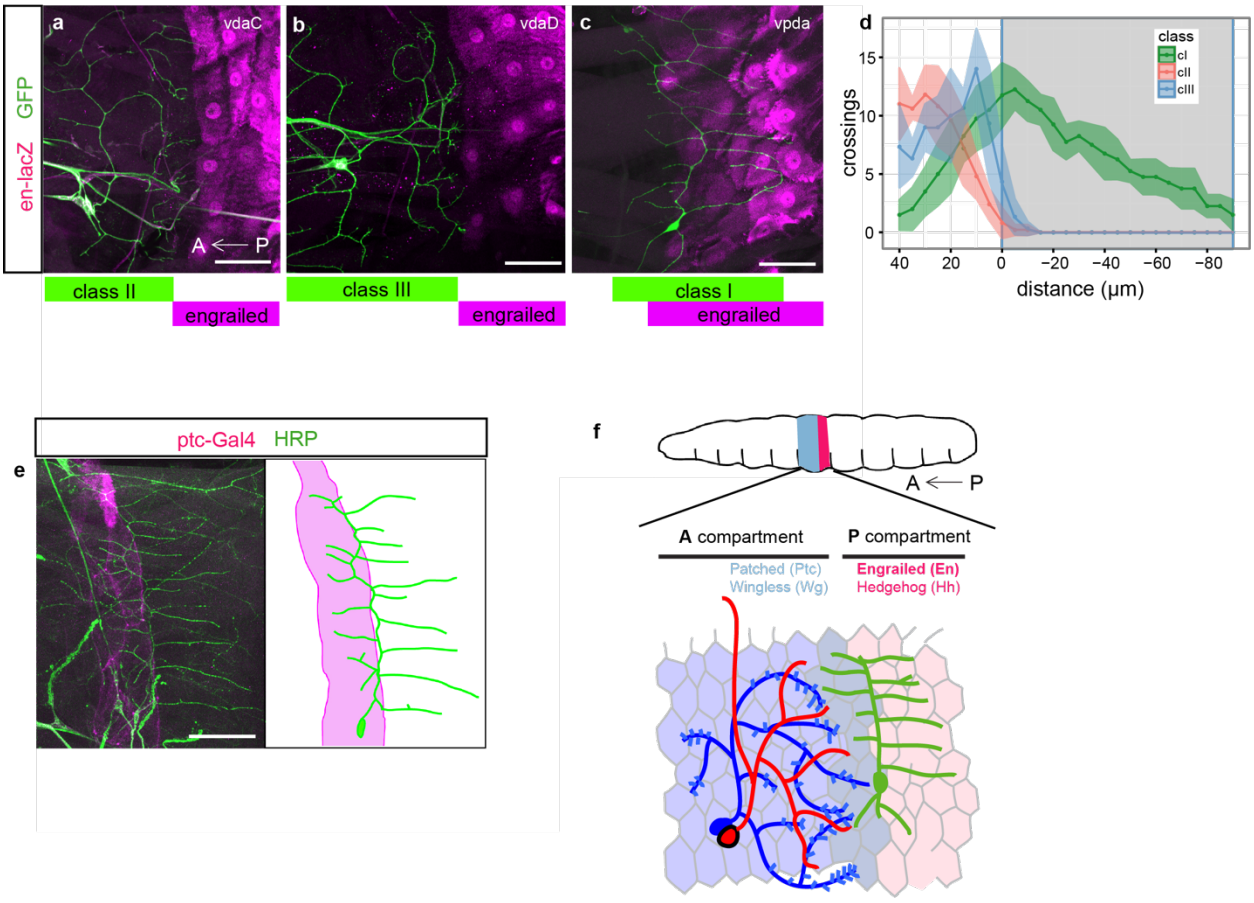

Figure 3.2. Dendritic boundaries correlate with segment compartments
(a) FLP-out labeling of cII neuron vdaC with the posterior (P) compartment labeled by *en-lacZ* (magenta). Note that dendrites terminate growth or turn before crossing into the *en-lacZ*-positive region. Figure reproduced from (Singhania, 2014) with permission.
(b) FLP-out labeling of cIII neuron vdaD with the P compartment labeled by *en-lacZ* (magenta). Note that dendrites terminate growth or turn before crossing into the *en-lacZ*-positive region. Figure reproduced from (Singhania, 2014) with permission.
(c) FLP-out labeling of cI neuron vpda with the P compartment labeled by *en-lacZ* (magenta). Note that dendrites grow primarily in the *en-lacZ*-positive region. Figure reproduced from (Singhania, 2014) with permission.
(d) Quantification of different growth patterns of cI (N=4), II (N=5), and III (N=3) neurons relative to the A-P compartment boundary. A-P compartment boundary represents 0 on the x-axis and the P compartment is shaded gray. Plots represent mean ± s.d (colored ribbons). Figure adapted from (Singhania, 2014) with permission.
(e) Co-labeling of cI neurons (using anti-HRP) and *ptc-Gal4* reporter expression (magenta) shows that anterior cI dendrites extend within the Ptc-expressing domain of the epidermis.
(f) Schematic diagram of the relationships between compartmental boundaries and dendritic territories of class I-III neurons in the ventral cluster.
Anterior is to the left in all images.
Scale bars = 50 μm

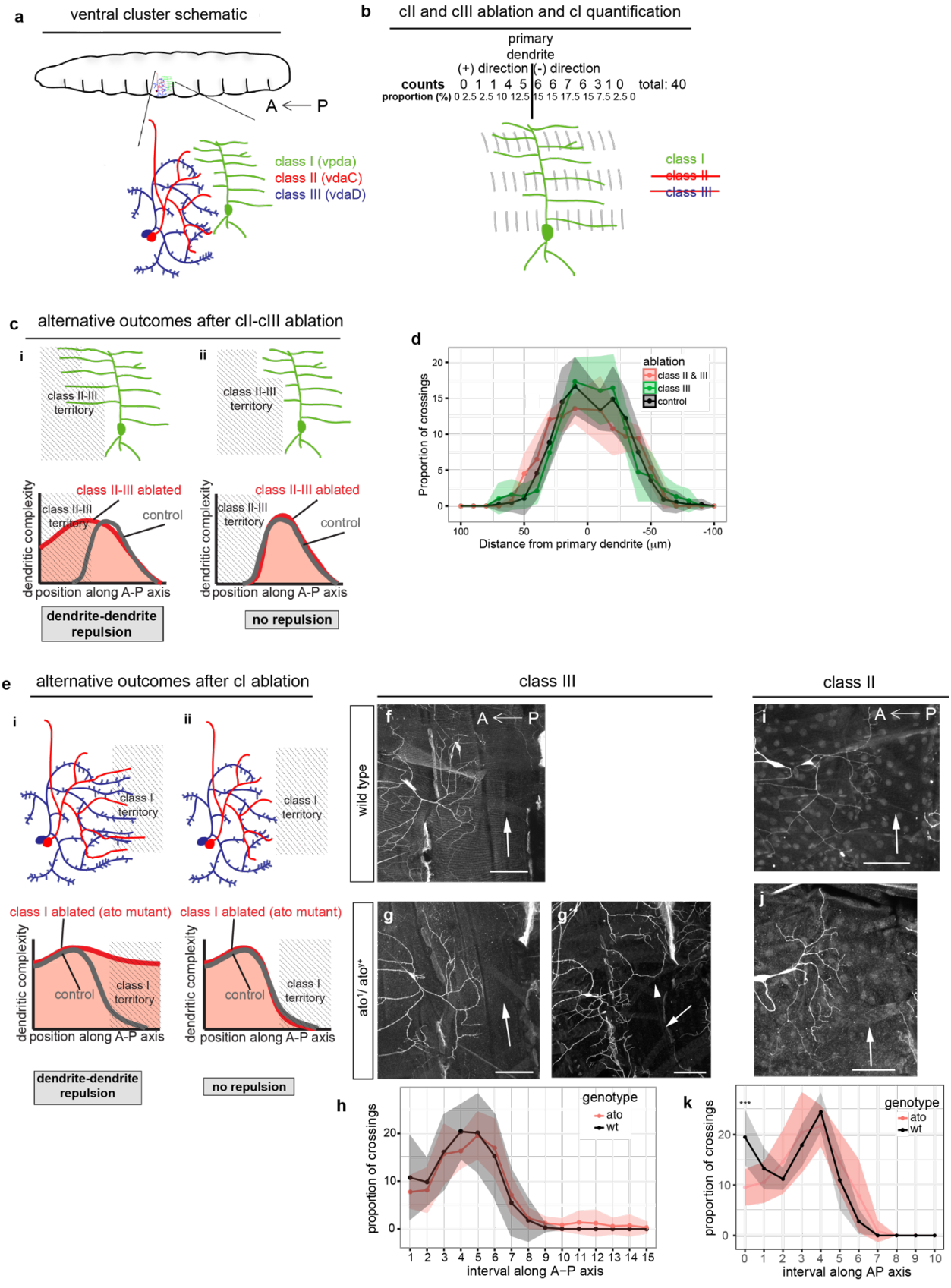
a
ventral cluster schematic
A ← P
class I (vpda)
class II (vdaC)
class III (vdaD)
b
cII and cIII ablation and cI quantification
primary dendrite
(+) direction
(-) direction
counts 0 1 1 4 5 6 6 7 6 3 1 0 total: 40
proportion (%) 0 2.5 2.5 10 12.5 15 15 17.5 15 7.5 2.5 0
class I
class II
class III
c
alternative outcomes after cII-cIII ablation
i
ii
class II-III territory
class II-III ablated
control
dendritic complexity
position along A-P axis
dendrite-dendrite repulsion
no repulsion
d
ablation
class II & III
class III
control
Proportion of crossings
Distance from primary dendrite (μm)
e
alternative outcomes after cI ablation
class I territory
class I ablated (ato mutant)
control
dendrite-dendrite repulsion
no repulsion
class III
class II
wild type
ato1/ ato1+
f
g
g'
i
j
h
genotype
ato
wt
proportion of crossings
interval along A–P axis
k
***
interval along AP axis

Figure 3.3. Ablations suggest that dendrite territories are not patterned by dendrite-dendrite interactions
(a) Schematic of cell body and dendritic fields of cI (green), cII (red) and cIII (blue) neurons in ventral cluster.
(b) Schematic of analysis used to quantify extent of anterior vs. posterior growth of vpda dendrites. A line is drawn along the primary dendrite, parallel contours are stacked at 10 μm intervals in anterior and posterior directions, and dendrite crossings at each line are tallied. The proportions of total crossings at each line are then calculated. Figure adapted from (Singhania, 2014) with permission.
(c) Schematic of alternative scenarios for responses of cI arbors upon ablation of cII/cIII neurons. (ci) If cI territories shift into the cII/cIII domain upon ablation this would provide evidence for dendrite-dendrite interactions. (cii) If cI arbors do not shift along the A-P axis then dendrite-dendrite interactions are unlikely to explain territory boundaries.
(d) Quantification of the branch intersections at evenly spaced intervals from primary branch of the vpda arbor in wild-type (black), upon cIII ablation (green) and upon cII/cIII ablation (red). Plots represent mean ± s.d. wild-type N=12, cIII ablation N=6 and cII/cIII ablation N=6. Results fit with scenario depicted in cii.
(e) Schematic of alternative scenarios for responses of cIII or cII arbors upon ablation of cI neurons. (ei) If cIII and/or cII territories shift along the A-P axis upon cI ablation then dendrite-dendrite interactions likely impact territory boundaries. (eii) Lack of shifting of cIII and/or cII arbors into the cI domain would provide evidence against heterotypic dendrite-dendrite interactions.
(f) Dendritic field of ventral cIII neuron vdaD showing posterior boundary relative to denticle band from the adjacent segment and vpda (arrow) in wild-type animals.
(g-g´) Dendritic field of ventral cIII neuron vdaD showing posterior boundary when the cI neuron vpda is genetically ablated in *ato*- animals (the absence of vpda is indicated by arrow). Some neurons show occasional growth into vpda region (g´, arrowhead) but boundary is mostly maintained.
(h) Quantification of the branch intersections at evenly spaced intervals from the first proximal branch point of the vdaD arbor in wild-type (black) and *ato*-/- (red) animals. Results fit with scenario depicted in eii. Plots represent mean ± s.d. wild-type and *ato* N=15.
(i) Dendritic field of ventral cII neuron vdaC showing posterior boundary relative to denticle band from the adjacent segment and vpda (arrow) in wild-type animals.
(j) Dendritic field of ventral cII neuron vdaC showing posterior boundary when the cI neuron vpda is genetically ablated in *ato*- animals (the absence of vpda is indicated by arrow).
(k) Quantification of the branch intersections at evenly spaced intervals from the first proximal branch point of the vdaC arbor in wild-type (black) and *ato*-/- (red) animals. Results fit with scenario depicted in eii. Plots represent mean ± s.d. wild-type and *ato* N=7. Statistical significance was evaluated with a Repeated Measured ANOVA with post-hoc Sidak's multiple comparisons test for each interval. *** represents intervals with $p<0.001$, all other intervals $p>0.30$.
Anterior is to the left in all images.
Scale bars = 50 μm.

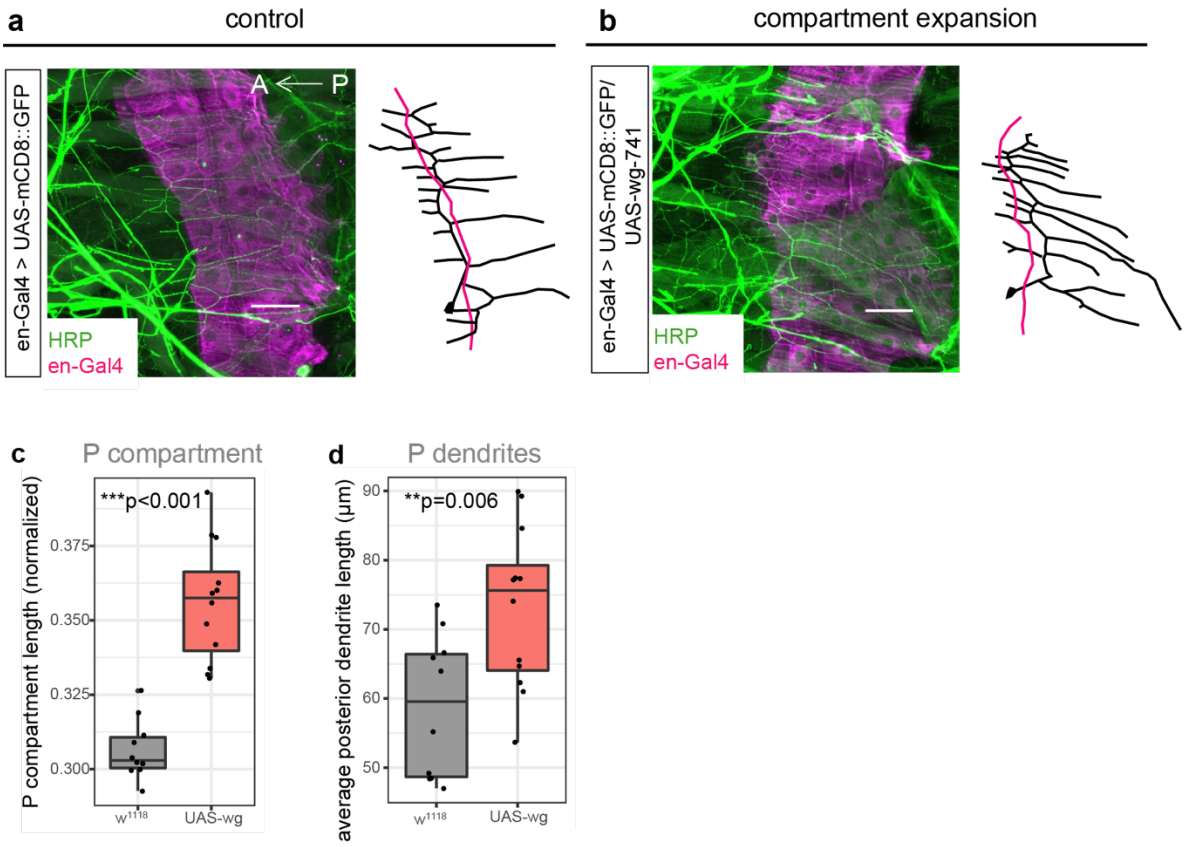

Figure 3.4. Evidence that compartmental cues regulate class I territories
(a) Co-labeling of vpda neurons (using anti-HRP) and *en-gal4 >UAS-mCD8::GFP*. Class I tracing shown at right, magenta line represents anterior-posterior compartment boundary.
(b) Co-labeling of vpda neurons (using anti-HRP) and *en-gal4>UAS-mCD8::GFP/UAS-wg-741*, leading to a larger *en-Gal4* domain. Class I tracing shown at right, magenta line represents anterior-posterior compartment boundary.
(c) Quantification of *en-gal4* domain length in w^{1118} control (n=10) and *en-Gal4> UAS-wg-741* (n=10) larvae. Horizontal line represents median, whiskers represent data range, and points represent outliers > 1.5 times the interquartile range. ***p<0.001 by two-tailed, unpaired Student's t-Test.
(d) Quantification of posterior dendrite length in w^{1118} controls (n=10) and *en-Gal4>UAS-wg-741* (n=12) larvae. Plotted as in (c). **p=0.006 by two-tailed, unpaired Student's t-Test.
Anterior is to the left in all images.
Scale bars = 50 µm.

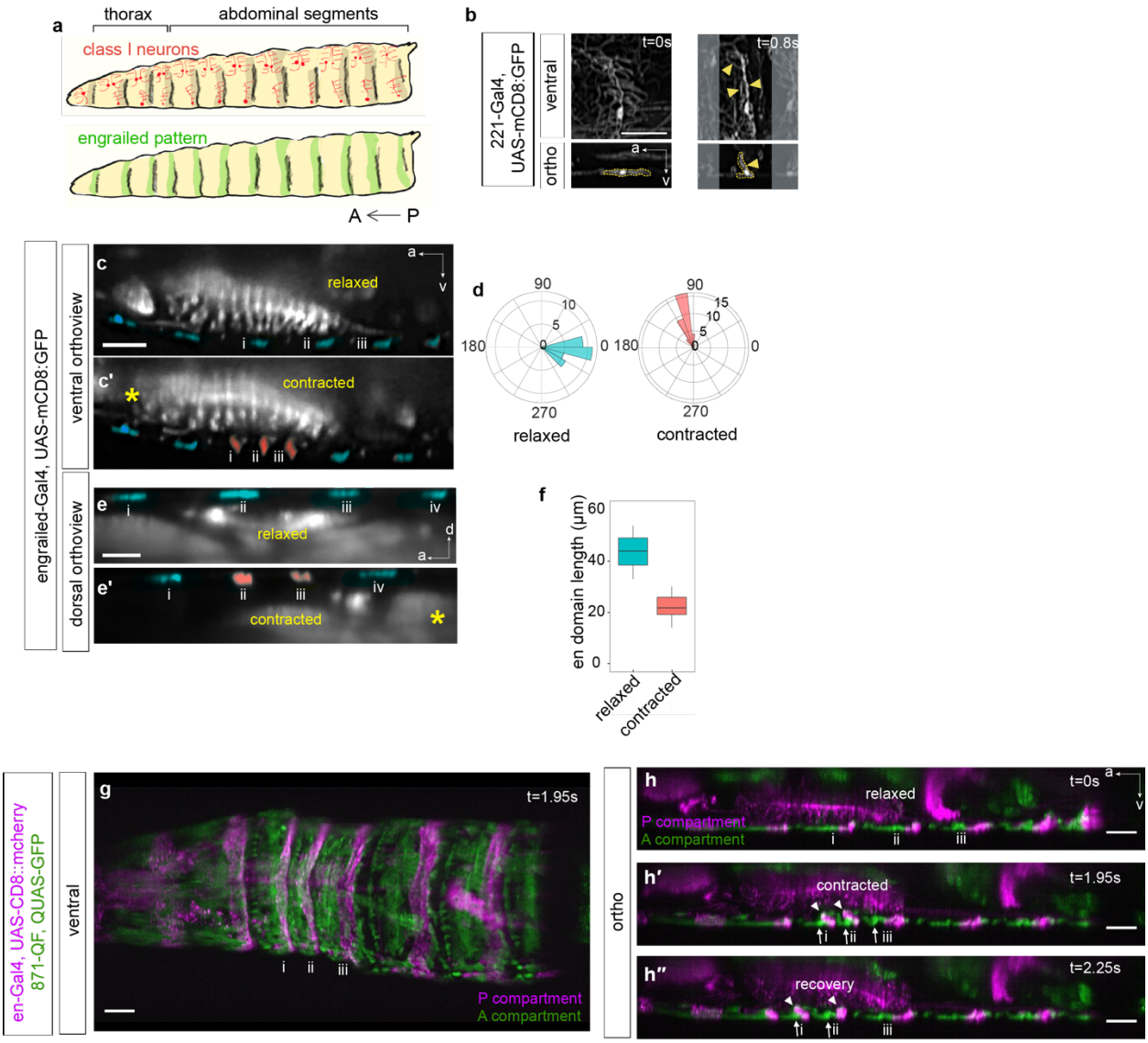

Figure 3.5. Analysis of epidermal deformation during locomotion using SCAPE
(a) Schematic of class I neuron distribution on body wall (top, red) and *engrailed*-positive compartments (bottom, green).
(b) SCAPE imaging of vpda dendrite dynamics seen in Chapter 2, reproduced here.
(c-c´) SCAPE imaging (orthogonal view) of the ventral body wall and CNS (asterisk) of a larva labeled by *en-Gal4, UAS-mCD8::GFP* at two time points during forward locomotion. Relaxed segments are artificially colored blue and contracted segments are red. The same segments are labeled i-iii in c and c´. During mid-body contraction *en-Gal4*-positive epidermis swings to a vertical arrangement (segments i, ii, iii in c´). This 90-degree folding of the epidermis is consistent with dendrite dynamics observed in (b).
(d) Distribution of epidermal angles, where 0˚ is a horizontal orientation, in relaxed segments (blue; n=31 relaxation phases in 6 segments from A2-A7, 1 animal) and contracted segments (red; n=33 contractions in 6 segments from A2-A7, 1 animal).
(e-e´) SCAPE imaging (orthogonal view) of the dorsal body wall of a larva labeled by *en-Gal4, UAS-mCD8::GFP* at two time points during forward locomotion. Extended segments are artificially colored blue and contracted segments are red. The same segments are labeled i-iv in e and e´. Note collapse of epidermis along horizontal axis (ii and iii segments in e´). Asterisk indicates gut fluorescence
(f) Quantification of engrailed domain (Posterior compartment) length on the dorsal side in relaxed (blue) and

contracted (red) segments (n= 20 contractions in 5 segments from A3-A7, 1 animal.) Horizontal line represents median, whiskers represent data range.
(g) Dual-color SCAPE imaging of ventral epidermis labeled with *en-Gal4, UAS-mCD8::mcherry* (magenta) and *871-QF, QUAS-GFP* (green).
(h-h´´) Orthogonal view of (g), across multiple time points. The same segments are labeled as i-iii across (g- h´´). Folding of posterior compartments (magenta) are highlighted with arrowheads, showing a sharp 90-degree fold. Different folding dynamics of anterior compartments (green), highlighted with arrows, show scrunching dynamics along horizontal axis.
a is anterior, d is dorsal, v is ventral.
Anterior is to the left in all images.
Scale bars = 50μm.

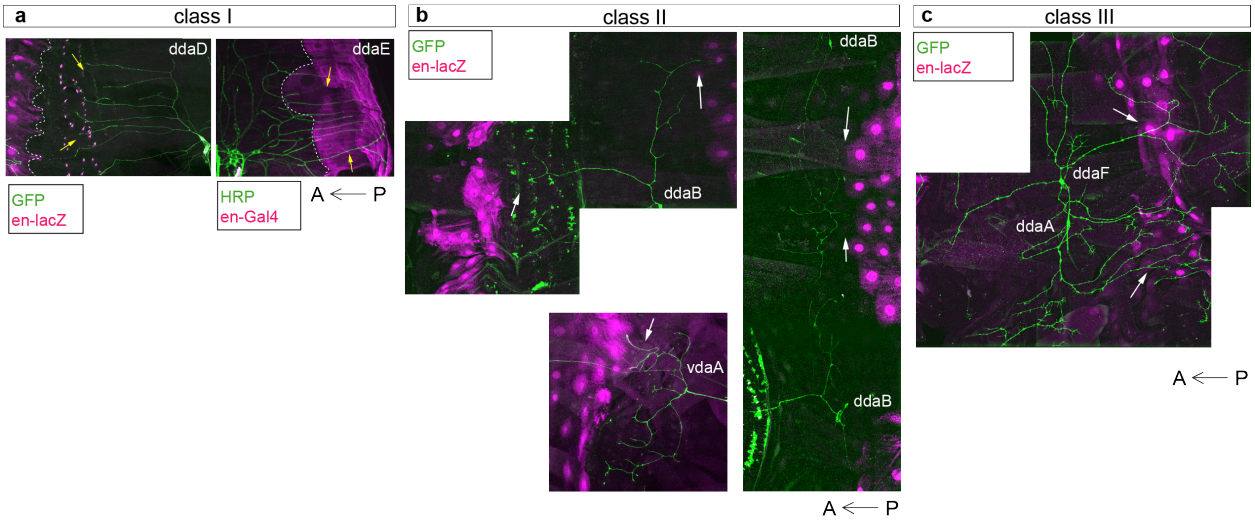

Figure 3.6. Characterization of dorsal class I-III dendritic boundaries relative to segmental compartments
(a) Labeling of dorsal class I (ddaD, left and ddaE, right) neurons (green) relative to the posterior (P) compartment (*en-lacZ* or *en-Gal4* labeling, magenta). ddaE dendrites (labeled with HRP stain) reside within the P compartment, similarly to vpda (see Fig. 3.2). ddaD dendrites (labeled with *221-Gal4*), reside within the A compartment.
(b) Labeling of dorsal (ddaB) and additional ventral (vdaA) class II neurons (green, labeled with *1112-Gal4*) relative to the P compartment (*en-lacZ*, magenta). All class II dendrites avoid the P compartment.
(c) Labeling of dorsal class III neurons (green, labeled with *nompC-Gal4*) relative to the P compartment (*en-lacZ*, magenta). Unlike vdaD (see Fig. 3.2), class III neurons in the dorsal cluster do not avoid the P compartment.
Anterior is to the left in all images.

Chapter 3 Movie Legends

Movie 3.1. SCAPE imaging of ventral posterior compartment during crawling. Compartment is labeled with *en-Gal4>UAS-mCD8::GFP*. Top panel shows ventral side maximum intensity projection (MIP) from full 180μm deep volume. Bottom panel shows a single slice orthogonal view through the midline of the animal. Anterior is to the left. SCAPE images are shown on a square-root grayscale to reduce dynamic range and permit visualization of both the ventral nerve cord and epidermis. Scale bars=100 μm.

Movie 3.2. Dual-Color SCAPE imaging of ventral body wall during crawling. The entire epidermis is labeled with *871-QF, QUAS-GFP* (green), and P compartment is labeled with *en-Gal4, UAS-mCD8::mcherry* (magenta). Top panel shows ventral side MIP substack. Bottom panel shows MIP substack orthogonal view through the midline of the animal. Anterior is to the left.

Movie 3.3. SCAPE imaging of dorsal posterior compartment during crawling. Compartment is labeled with *en-Gal4>UAS-mCD8::GFP*. Top panel shows dorsal side MIP over a 20 μm depth range from a 180μm deep volume. Bottom panel shows a single slice orthogonal view through the midline of the animal. Anterior is to the left. SCAPE images are shown on a square-root grayscale to reduce dynamic range. Scale bars=100 μm.

Chapter 4. Dissecting the role of substrate cues in regulating the compartmental organization of sensory dendrites

I am grateful to Siqian Feng, Ryan Loker, and Judith Kribelbauer for advice on RNA-sequencing protocols and for running the libraries on the Illumina sequencer. Thank you to Aomeng Cui for assistance with the RNAi screen.

Introduction

The development of dendritic territories is essential for determining a sensory neuron's receptive field or for regulating the exact information received by a downstream neuron within a larger circuit. The *Drosophila* larva somatosensory system is a useful model for studying the patterning of dendrite territories because the neurons are amenable to genetic manipulation, labeling, and imaging. A subset of somatosensory neurons, the dendritic arborization (da) neurons, have complex morphologies and can be delineated into four classes (cI-cIV), each with a different function and unique dendrite territory coverage (see Chapter 3) (Grueber et al 2002, Singhania & Grueber 2014). These da dendrites lie between the basal surface of the epidermis and the ECM (Han et al 2012, Kim et al 2012), and the dendritic territories of each neuron lie in a stereotypical region of the epidermis.

In Chapter 3, we show that proprioceptive (cI) and touch-sensing (cII-cIII) da neurons show a compartmental organization: in the ventral cluster, cII-III touch-sensing dendrites avoid the Posterior (P) compartment, while cI proprioceptive dendrites are biased to grow within the P compartment (schematic shown in Fig. 4.1a, see Chapter 3 for detailed description). A similar compartmental organization is observed for the dendrites of larval motor neurons in the central nervous system (Landgraf et al 2003), suggesting this organizing principle is relevant to neurons across systems. Compartmental organization could conceivably function to coordinate sensory

and motor systems in *Drosophila*. However, the mechanisms responsible for guiding the compartmental organization of motor or sensory dendrites have not been identified.

Our evidence in Chapter 3 suggests that compartmentalized cues within the epidermal substrate instruct the dendrite territory coverage of at least some da neurons, as genetic expansion of the P compartment leads to expansion of the ventral cI proprioceptive dendrites. However, the molecular identities of these compartmentalized cues are unknown. In this chapter, I investigate the role of substrate cues in regulating the compartmental organization of sensory dendrites. First, I describe knockdown and misexpression experiments performed to test molecular candidates that are known to be expressed within a specific epidermal compartment (e.g. Hedgehog and Spitz). To reveal additional candidates, I performed gene expression profiling of the P and A compartments to uncover molecules with differential expression. I report initial findings from a knockdown and misexpression screen testing the effect of selected differentially expressed cell surface and secreted (CSS) molecules on cI-cIII dendrite territories.

Results

Evidence that Hedgehog and EGFR pathways do not affect dendrite territory location

While compartment expansion experiments suggest that compartmentalized epidermal cues instruct ventral cI (vpda) dendrite targeting to the P compartment (see Chapter 3, Fig. 3.4), the molecular identity of these cues are unknown. Previous research has revealed multiple molecules that are expressed in a compartmental fashion (Sanson 2001). Hedgehog (Hh) is secreted from the P compartment, raising the possibility that vpda dendrites could be attracted by the Hh molecule (Fig. 4.1a-a′). Prior studies from the lab suggested that misexpression of Hh in the A compartment with a *wingless (wg)* driver caused the primary dendrite location to shift

posteriorly, but did not change the location or "footprint" of the vpda dendritic field (Singhania 2014). Since the location of the vpda dendrites were inferred indirectly, it was still possible that Hh had a more substantial effect on dendrite targeting to the P compartment.

To confirm and expand upon those results, I identified a *wg* driver (*16D01-Gal4*) that is specific to the epidermis and used this to drive Hh expression while marking the P-compartment with *en-LacZ* (Fig. 4.1b-c‴). I used a modified Sholl analysis to quantify the territory position of vpda relative to the A-P compartment boundary. I found no significant difference between vpda territories with and without Hh misexpression in the *wingless* domain (Fig. 4.1f, $p>0.45$ at all intervals), indicating that the location of the vpda dendritic field is unchanged. To quantify primary dendrite location, I measured the area between the primary dendrite and the A-P compartment boundary (normalized by primary dendrite length, see methods for details). Misexpression of Hh in the A compartment led to a significant posterior shift in primary dendrite position (Fig. 4.1d, *$p=0.022$), suggesting that high levels of Hh repel the primary dendrite of vpda. P compartment length was unaffected (Fig. 4.1e, $p=0.411$), suggesting a shift in the primary dendrite rather than an anterior expansion of the compartment. Previous work in the lab showed no effect on cIII vdaD dendrites with *hedgehog* gain of function mutants in the epidermis (Singhania 2014), and I did not further explore this question.

Another molecule that shows a compartmental organization is Spitz (Spi), an Epidermal Growth Factor Receptor (EGFR) ligand, which is secreted from the most anterior edge of the A compartment (O'Keefe et al 1997) (Fig. 4.2a). This zone of secretion is just posterior to vpda dendrites within the neighboring anterior segment. Therefore, we tested whether Spi could help set the stopping point of vpda dendrites at the segment boundary. This signal could hypothetically be a repulsive cue (to prevent growth into the next segment) or an attractive cue

(to encourage growth well into the P compartment). To test this hypothesis, I expressed an EGFR dominant negative construct to interfere with EGFR signaling in class I neurons (Fig. 4.2 b-c). If Spi is attractive, I would expect less coverage of vpda dendrites in the P compartment, and if Spi is repulsive, I would expect growth of vpda dendrites into the neighboring segment.

Vpda showed an overall increase in total dendrite length (Fig. 4.2e, **p=0.002), but no change in dendrite territory coverage, as measured by a modified Sholl analysis (Fig. 4.2d, p>0.20 at all intervals). Increase in total dendrite length was primarily driven by an increase in the number of anterior-oriented dendrites and an increase in posterior-oriented dendrite complexity (See Fig. 4.2f-g″ and legend for more details). These results suggest that EGFR signaling is important for limiting the number of secondary dendrites and branch points but does not regulate dendrite territory coverage.

Differential expression of cell surface and secreted molecules in the posterior vs. anterior compartments

There are likely to be many unknown genetic differences between the P and the A compartments. To reveal new candidates that could be important for regulating the compartmental organization of sensory dendrites, I performed RNA sequencing gene expression profiling of the P and A compartments to identify molecules with differential expression (Fig. 4.3a). To purify P and A compartment cells, I used Fluorescence Activated Cell Sorting (FACS) on dissociated cells from stage 12-14 embryos, which is after the generation of intrasegmental compartments (Sanson 2001). P compartment epidermal cells were sorted from embryos with *engrailed-Gal4* driving both *UAS-myr::GFP* and *UAS-nls-tdTomato. Elav-Gal80* was also included to eliminate nervous system expression (Fig. 4.3b). Double-labeling allowed for more

precise sorting of cell populations, as only cells with both high GFP and high tdTomato fluorescence were extracted from the sort (Fig. 4.3d). I sorted A compartment cells from a separate set of embryos containing *35A08-Gal4,* a Gal4 driven by an enhancer fragment near the *sloppy paired 1 (slp1)* locus (Manning et al 2012, Pfeiffer et al 2008) that labels a ventral/posterior portion of each A compartment (Fig. 4.3c). These embryos also contained *elav-Gal80* and the same *UAS-myr::GFP* and *UAS-nls-tdTomato* markers. Approximately 2-3% and 3-4% of all dissociated cells were extracted from the P compartment and A compartment sorts, respectively (Fig. 4.3 d-e).

To test the quality of the initial sorts, I performed quantitative reverse transcription PCR (qRT-PCR) to test for mRNA expression levels of *en, slp1,* and *wg* in the P versus A compartment cell populations. Patterns in expression differences were as expected. The P compartment showed an 8.75-fold increase in *en* expression relative to the A compartment, while the A compartment showed a 3.13- and 2.79-fold increase in *slp1* and *wg1* expression, respectively.

Following qRT-PCR quality control, two additional dissociations and sorting sessions were performed for each genotype to obtain three biological replicates for each cell type. RNA-sequencing (RNA-seq) of these cells and subsequent edgeR (Robinson et al 2010) differential expression analysis revealed 1169 genes differentially expressed between the P and the A compartments (500 enriched in P and 669 enriched in A, Fig. 4.4 a-b). *Hh*, *slp1*, *slp2*, *wg*, and *patched (ptc)* showed the expected pattern of expression differences (Fig. 4.4c). Expression levels of *en* (log counts per million) were very low (Fig. 4.4c, red text), and the fold change is not statistically significant and likely inaccurate.

I reasoned that substrate cues that guide dendrite territories are very likely to involve cell surface and secreted (CSS) proteins in order to facilitate communication between the cells. Recently, the Grishin Lab published a comprehensive database of CSS genes in *Drosophila* (FlyXCDB*)* (Pei et al 2018). 2509 genes were characterized as containing extracellular domains, using computational predictions of transmembrane segment, signal peptide, and GPI-anchor signal sequence, as well as profile-based sequence similarity searches, gene ontology, and literature. Of the 1169 genes differentially expressed between the P and the A compartments, 293 of these transcripts code for CSS proteins as defined by FlyXCDB (132 enriched in P and 161 enriched in A, Fig. 4.4b). These genes are listed in full in Appendix A, along with the log fold change, log counts per million, and adjusted P-value from the edgeR analysis.

Testing candidates from differential expression analysis

To test CSS candidate genes from the differential expression analysis, I performed a targeted RNAi and misexpression screen in collaboration with other lab members. We used *en-Gal4* along with UAS-RNAi lines to knock down expression of P-enriched genes in the P compartment. We also used publicly available UAS-misexpression lines to ectopically express A-enriched genes in the P-compartment. Animals were then evaluated for changes in cI vpda and cIII vdaD dendrite territories.

The logic of the screen is as follows. If a P-enriched molecule is attractive for cI dendrites, knockdown could lead to less vpda dendrite growth in the P compartment. If an A-enriched molecule is repulsive to cI dendrites, misexpression of this gene in the P compartment would also lead to less vpda dendrite growth in the compartment. Conversely, if a P-enriched molecule is repulsive to cIII dendrites, knockdown could lead to more vdaD dendrite growth in

the P compartment. If an A-enriched gene is attractive for cIII dendrites, misexpression of this gene in the P compartment could also lead to more vdaD dendrite growth in the P compartment.

While the eventual goal is to screen though all 293 CSS gene candidates, we aimed to first screen a group of high-priority genes. I selected a top group of ~30 P-enriched and ~30 A-enriched CSS gene candidates based on a combination of criteria (Tables 4.1-4.2). Top candidates had predicted extracellular domains likely involved in protein-protein interactions (e.g. Immunoglobulin (IG) or EGF-like domains) or signaling molecules (e.g. growth factors, morphogens), as defined by FlyXCDB (Pei et al 2018). A few additional top candidates had enzymatic domains that were likely peptidase or protease inhibitors, and could therefore potentially affect the gradient of a signaling molecule (e.g. *neprilysin1*, *serpin100A*). I also used *in situ* hybridization images of mRNA transcript expression patterns from the BDGP (insitu.fruitfly.org) and Fly-FISH (fly-fish.ccbr.utoronto.ca) databases to prioritize candidates: if *in situ* expression was available and did not show a segmental pattern, the gene was excluded from the top candidate list.

To date, we have performed a primary screen of 23 UAS-RNAi lines of the top P-enriched candidates (see Table 4.1) and 5 UAS-misexpression lines of the top A-enriched candidates (see Table 4.2). UAS lines were crossed with *en-Gal4* to cause expression changes within the P compartment. *UAS-mCD8::GFP* was used to visualize the compartment, anti-HRP antibody was used to visualize the cI dendrites, and *nompC-LexA, LexAop-mCD8::Cherry* was used to distinguish the more complex cIII dendrites. We have not found any LexA or QF lines that can distinguish the cII neurons for analysis, so despite their compartmental restriction we did not analyze these neurons. We dissected ~3 animals per cross and captured confocal images of at least 2-3 different neurons to document sensory dendrite territories. Initially, images were

inspected visually side-by-side with controls [*UAS-Luciferase.valium10* for RNAi screen and w^{1118} for misexpression screen]. Genes with potential effects on cI or cIII dendrite territory or P compartment size, by visual inspection, are noted in the final column of Tables 4.1 & 4.2.

Vpda and vdaD territories are variable in control animals. For example, control vdaD neurons sometimes extend one dendrite well into the P compartment (Fig. 4.5c′), and control vpda secondary dendrites vary in number and length (Fig. 4.5a-a′). Therefore, minor or partially penetrant effects on dendrite territories are difficult to distinguish without large sample sizes and careful quantification. With some knockdowns, vpda posterior-oriented dendrites appeared sparser than controls (*tsp-RNAi, dsd-RNAi, fj-RNAi, prc-RNAi*. Table 4.1), but secondary screening would be needed to conclusively verify such effects. See Fig. 4.5b-b′ for example images of a potential effect in vpda with *distracted(dsd)-RNAi*. It is possible that one of the molecules that was not part of our primary screen is the major cue or that multiple genes combine in a partially-redundant fashion to control dendrite territory pattering.

Similarly, expression of *mey-RNAi, spz6-RNAi, pyr-RNAi*, *UAS-toll6, UAS-wnt4* (Tables 4.1-4.2) appeared to lead to more extensive growth of vdaD dendrites into the P compartment and therefore should be the focus of more detailed secondary screening to evaluate if there are significant effects. See Fig. 4.5d-d′ for example images of vdaD dendrites with *morpheyus(mey)-RNAi* knockdown.

Misexpression of Wnt4 in the P compartment showed the most robust and noticeable qualitative effect. Therefore, I followed up by quantifying dendrite territory changes (Fig. 4.6). To quantify, I traced the total vdaD dendrite length within the P compartment (Fig. 4.6a-b). Total length trended larger in *UAS-wnt4* animals (Fig. 4.6c, p=0.08, w^{1118}, n=8, *UAS-wnt4,* n=5). Notably, in 2 out of 5 *UAS-wnt4* cells, some vdaD dendrites grew past the segment boundary at

the posterior edge of the P compartment, which has never been seen in controls or with any other manipulation. As Wnt4 antagonizes Wg signaling in the ventral epidermis of stage 11 embryos (Gieseler et al 1999), we predicted that P compartment size might be reduced in these animals. While P compartment size trends lower in Wnt4 misexpression animals, the effect is variable and the change was not significant (Fig. 4.6d, p=0.25).

While not the focus of this study, knockdown of Fasciclin 3 (Fas3), a cell adhesion molecule, showed obvious effects on dendrite branching and growth direction rather than on the dendrite territory location of vpda neurons. Aberrant branch patterns were observed in 1 out of 3 animals (Fig. 4.7b-b′). Fas3 could be a focus of future studies.

Knockdown of yellow-d and mthl9 shortens the P compartment

Some RNAi knockdowns resulted in a change in compartment size. Knockdown of *yellow-d,* which codes for a major royal jelly protein, and *methuselah-like 9 (mthl9),* a GPCR, resulted in narrower P compartments versus *luciferase-RNAi* controls (Fig. 4.8a-b, ***p<0.001 for both knockdowns versus controls). Additional experiments indicated that the anterior portion of the P compartment is lost upon *yellow-d* knockdown (Fig. 4.8c, **p=0.003), while the exact effect of *mthl9* on compartment size was not determined. The small size of the P compartment epidermal cells (Fig. 4.8a′-a″) suggests a potential growth defect. P compartment cell size was quantified in *yellow-d* knockdowns vs. controls, showing a significant effect: *yellow-d-RNAi* cell radius= 27.97 µm ± 2.88 s.d.; *luciferase-RNAi* cell radius= 64.39 µm ± 5.40 s.d. (***p<0.0001 by two-tailed, unpaired Student's t-Test).

Changes in compartment size provided a way to explore the effect of a narrower compartment on vpda and vdaD cells (Fig. 4.8d-d″, h-h′). With *yellow-d* knockdown, the primary

dendrite of vpda no longer resided along the A-P compartment boundary, but rather was located significantly anterior to the boundary (Fig. 4.8e, ***$p<0.001$). This result suggests that the primary dendrite is not migrating to the posterior-shifted A-P compartment boundary, but perhaps remaining in a similar location as controls. Supporting this idea, the average length of posterior-oriented vpda dendrites is not significantly different from controls (Fig. 4.8f, $p=0.938$). By contrast, the average length of anterior-oriented dendrites is significantly shorter with *yellow-d* knockdown (Fig. 4.8g, *$p=0.045$).

VdaD dendritic fields may also be affected by the compartment narrowing in *yellow-d* knockdown animals. Our current working hypothesis predicts repulsive cues in the P compartment and/or attractive cues in the A compartment near the A-P boundary guide vdaD dendrite territories. If this hypothesis is true, we would predict that vdaD dendrites may expand posteriorly to cover more territory due to a posterior shift in the A-P boundary. To evaluate vdaD territories, I performed two modified Sholl analyses: one in relation to the A-P compartment boundary and one in relation to a stereotyped anterior muscle attachment site, which likely remains stable during *yellow-d* knockdown (Fig 4.8h-j, proportion of dendrite crossings at intervals along the AP axis, see methods for details). The analysis relative to the stable muscle attachment site suggests a minor posterior shift of vdaD dendrite coverage with *yellow-d* knockdown. (Fig. 4.8j). If compartment cues are the sole regulators of vdaD dendrite boundary formation, then we would predict dendrites in *yellow-d* knockdowns would extend posteriorly all the way to the shifted A-P boundary. In contrast, the second modified Sholl analysis shows dendrites in *yellow-d-RNAi* animals are shifted anteriorly relative to the A-P boundary (Fig. 4.8i). Together, these results suggest that vdaD dendrites shift their coverage posteriorly, but do not extend all the way to the A-P boundary as is observed in wild type animals. We speculate that a

redundant repulsive cue from neighboring vpda dendrites prevents a larger expansion of vdaD coverage. Future experiments could test this scenario by evaluating whether the extended vdaD dendrites stop where they form a tiling boundary with vpda dendrites.

Discussion

In this chapter, I probe the role of cell surface and secreted molecules in the epidermal substrate in regulating the compartmental organization of proprioceptive (cI) and touch-sensing (cIII) dendrites. Our evidence suggests that compartment cues within the epidermal substrate instruct the territory coverage of ventral cI dendrites (see Chapter 3), but the molecular identities of these cues are unknown. Here, I show that CSS molecules previously known to be expressed in a compartmental manner do not affect the location of cI dendrite territories. To identify novel candidates, I performed gene expression profiling with RNA sequencing to reveal 290 CSS molecules that show differential expression in the P and A compartments. A primary knockdown and misexpression screen of ~30 prioritized candidates revealed a number of genes that appear to affect cI or cIII territory coverage. While none of these targets can alone fully explain compartmentalized dendrite targeting, several candidates emerged from the screen, and the results provide a foundation for future secondary screening efforts. Our list of differentially expressed molecules is an essential step towards identifying the molecular cues that specify the compartmental organization of sensory dendrites.

Hedgehog and EGFR pathways do not affect vpda dendrite territory location

Hedgehog (Hh) and Spitz (Spi) are known to be expressed compartmentally, but manipulation of either pathway did not affect the dendrite territory coverage of cI vpda neurons.

Hh is secreted from the P compartment, suggesting it is potentially attractive to vpda dendrites, but misexpression of Hh in the A compartment did not lead to ectopic expansion of vpda dendrites. Likewise, previous work from the Grueber lab also showed no effect on cIII vdaD dendrites with a *hedgehog* gain of function mutant (Singhania 2014). Spi, an EGFR ligand, is released from the anterior most section of the A compartment, but knockdown of EGFR signaling within vpda neurons did not change dendrite territory coverage. Our results are consistent with what was previously observed in the larval motor system, where the compartmental organization of dendrites is similarly not determined by classic compartment cues like Hedgehog (Landgraf et al 2003).

While we did not see an effect of Hh on vpda dendrite territory coverage, we did see a significant shift in the location of the primary dendrite, suggesting primary and secondary vpda dendrites can respond differently to compartmental cues. Since vpda primary dendrites normally grow along the A-P compartment boundary, they could be guided to an intermediate level of Hedgehog along the morphogen gradient, leading to a repulsive response when Hh is artificially high in the A compartment. One possibility is that the difference in Hh responsiveness between primary and secondary vpda dendrites is due to differences in the developmental timing of dendrite outgrowth.

Based on anatomical characterizations presented in Chapter 3, compartment cues may act redundantly with repulsive heterotypic dendrite-dendrite interactions to pattern sensory dendrites. In support of this possibility, where cI and cII/cIII dendrites co-innervate the ptc domain, their dendrites very infrequently cross each other. To test this possibility, future experiments could evaluate vpda territories upon Hedgehog misexpression or EGFR-signaling knockdown with simultaneous ablation of neighboring cII/cIII neurons.

Gene expression profiling reveals genes differentially expressed in the A and P compartments

To identify additional molecular candidates that may be involved in specifying the compartmental organization of dendrites, I performed FACS and RNA sequencing to reveal 290 CSS molecules that are differentially expressed between the P and A compartments (Appendix A). These CSS genes are a subset of a larger list of 1169 differentially expressed genes, and this entire list has implications for future studies investigating general principles of compartment patterning. Lineage-restricted compartments are an important feature of many tissues during early patterning: compartment boundaries prevent the mixing of cells fated for different structures and contain a signaling center that provides positional information to neighboring cell populations (Kiecker & Lumsden 2005). In vertebrates, similar compartments are formed during the development of tissues such as the limb bud and hindbrain.

In addition to the *Drosophila* embryo body wall, compartment specification has also been well-studied in *Drosophila* imaginal discs (Lawrence & Struhl 1996). To our knowledge, the only other profiling study of the A and P compartments is a microarray analysis of the wing disc (Ibrahim et al 2013). Future studies could compare gene expression of the embryonic epidermal compartments to imaginal disc compartments, which could provide insights into general principles of tissue compartment patterning. Of the 290 differentially expressed CSS genes revealed in our study, only 8 genes (in addition to *hh*) overlap with the previously reported CSS genes differentially expressed in the wing disc (Appendix A). These overlapping genes are good candidates for conserved mechanisms of compartment patterning across tissues.

Knockdown and misexpression screen of CSS genes differentially expressed between the P and A compartments

In an initial knockdown and misexpression screen of ~30 top candidates from our list of differentially expressed CSS genes, there were a few genes that appeared to affect vpda or vdaD territory coverage and should be the focus of a more detailed secondary screening to evaluate significance (Table 4.1-4.2, final column). If confirmed, an effect from multiple genes would suggest a combination of partially-redundant guidance cues are important for dendrite territory pattering. Future experiments should continue screening through the candidates revealed from the differential expression analysis.

One notable candidate for further analysis is Wnt4: misexpression of Wnt4 within the P compartment seems likely to increase vdaD dendrite growth into the compartment (Fig. 4.6, trending $p=0.08$), suggesting Wnt4 may be attractive to cIII dendrites. If Wnt4 is usually secreted from the A compartment, attraction to this molecule may guide vdaD dendrites away from the P compartment.

As discussed above, it is possible that compartment cues in the substrate act redundantly with repulsive heterotypic dendrite-dendrite interactions to pattern sensory dendrites. It would be interesting to evaluate if manipulation of promising compartment cues in combination with ablation of neighboring heterotypic neurons leads to a more robust change in dendrite territories.

We also found that knockdown of *yellow-d* or *mthl9* led to the narrowing of the P compartment. With *yellow-d* knockdown, it appears that an anterior portion of the P compartment is lost. These results may be relevant to understanding compartment specification since, to our knowledge, *yellow-d* and *mthl9* have not been characterized as important for the specification of the P compartment. Alternatively, it is possible that they act to maintain

compartment size as the animal grows. Future studies could look at P compartment size at different stages to determine this timeline. Yellow-d, a major royal jelly protein in the *yellow* gene family, is important for tissue growth in the wing disc (Liang et al 2014), suggesting the observed P compartment narrowing is due to a tissue growth defect. This idea is supported by the significantly smaller size of P compartment cells in the *yellow-d* knockdowns. Little is known about the function of Mthl9, a GPCR.

In Chapter 3, I describe experiments where a posterior expansion of the P compartment leads to expansion of posterior-oriented vpda dendrites, suggesting that compartment cues regulate vpda dendrite territories. Does narrowing of the P compartment with *yellow-d-RNAi* lead to decreased dendrite length? Notably, knockdown of *yellow-d* did not change the average length of posterior-oriented vpda dendrites. This is at least partially explained by the observation that the primary dendrite of vpda no longer resides along the A-P compartment boundary, but rather is located significantly anterior to the boundary, suggesting that the primary dendrite is remaining in a similar location as controls.

With our current data from *yellow-d* knockdown larvae, we do not know if the P compartment is initially narrow or narrows later in development. If the P compartment is narrow prior to the growth of sensory dendrites, our results would suggest that cues independent of the compartment (which may include a combination of substrate-dendrite and dendrite-dendrite cues) are sufficient to pattern dendrites. These independent cues may be redundant with the hypothesized compartment cues. If the P compartment narrows after the patterning of sensory dendrites (potentially due to a growth defect), then this timeline would be consistent with a model in which sensory dendrites are initially patterned by compartment cues and then relatively

robust to changes in those cues later in development. Future studies of the timeline of P compartment narrowing will clarify these models.

While there was no change in posterior-oriented dendrites, the average length of anterior-oriented dendrites is significantly shorter with *yellow-d* knockdown. How could a shorter compartment lead to a change in anterior-oriented dendrites? In wild type animals, the anterior dendrites of vpda are contained within the *ptc/wg* domain of the substrate, which is just to the anterior side of the A-P boundary (see Chapter 3, Fig. 3.2e). Our studies also indicate that overexpression of Hh does not affect vpda dendrite territory location. Taken together, these results suggest a hypothesis worth exploring: the narrow compartment caused by *yellow-d* knockdown could affect the location or size of the *ptc/wg* domain, which could restrict vpda dendrites to a narrower domain. Future studies could examine any potential changes to the *ptc/wg* domain with *yellow-d* knockdown.

In all, our novel list of differentially expressed molecules in the P and A compartments and our initial knockdown and misexpression screen provide important insights towards identifying the molecular cues essential for specifying the compartmental organization of the nervous system.

Additional future directions

Our RNA sequencing data also identified candidate molecules important for potential cuticle differences in the A and P compartments. As discussed in Chapter 3, SCAPE imaging revealed that on the ventral side, the P compartment is a robust marker for a major cuticle fold that occurs during crawling, consistent with the idea that ventral cI dendrites are targeted to this region to be tuned for proprioceptive stimuli. The epidermis secretes a cuticle that functions as

an exoskeleton, and preferential distortion of the P compartment could be due to a specialized protein composition that regulates the physical properties of the cuticle. Supporting this idea, our RNA sequencing analysis revealed 25 potentially cuticle-related genes that are differentially expressed between the P and the A compartments, 22 of which were enriched in the P compartment (Table 4.3). Since chitin, a polysaccharide, is the major building block of insect cuticle, molecules were considered potentially cuticle-related if they had chitin-binding or carbohydrate-binding motifs (as defined by FlyXCDB), or were part of a family of genes known to be important in the cuticle (e.g. *tweedle* gene family and *ectodermal)*. Future experiments could knock down or misexpress these genes and evaluate the effect on the physical properties of the cuticle.

Future work may be able to improve on our cell sorting. The *35A08-Gal4* line we used targets only the ventral/posterior portion of each A compartment, and the *elav-Gal80* line is not always completely effective, leading to potential contamination of neural cells in the sort. It is possible that the A compartment sorts had more neural contamination than the P compartment sorts, as many of the A-enriched genes are also known to be expressed in neurons (Table 4.2, Appendix A). If future tools are developed to more specifically target the entire A compartment, sorting results may be more accurate. Alternatively, a recently developed technique to profile cell-type-specific, cell-surface proteomes in intact tissues may reveal a narrower list of candidates that are confirmed to be expressed at the cell surface (Li et al 2020).

Class II neurons were not evaluated during the knockdown/misexpression screen, because to date, there are no LexA or QF lines that can easily distinguish the cII neurons for analysis. Future work should develop the appropriate tools to assess cII dendrites. Unlike cIII neurons, all four cII neurons within a hemisegment avoid the P compartment (see Chapter 3, Fig.

3.6), so studies of their territories may be more likely to reveal molecules important for guiding the compartmental organization of dendrites.

In the current study, we used a P compartment driver (*en-Gal4*) to knock down expression of P-enriched genes or ectopically express A-enriched genes. Future screens should use an A compartment Gal4 line (e.g. *35A08-Gal4*) to evaluate the effects of knocking down A-enriched genes or misexpressing P-enriched genes. Furthermore, while RNAi knockdown lines are currently more readily available than UAS-misexpression lines, we predict misexpression screens might be especially useful, as cues with redundant effects are more likely to be revealed. Recent development of a high-throughput CRISPR-based method allowed for quick production of UAS-ORF plasmids covering 83% of the *Drosophila* genome (Wei et al 2020). These plasmids hold the potential to generate a large library of transgenic overexpression lines. Targeted screening with such a library holds promise for revealing important molecules guiding the compartmental organization of sensory dendrites, and the nervous system more broadly.

Methods

Fly lines

All stocks were obtained from the Bloomington *Drosophila* Stock Center unless otherwise noted. *16D01-Gal4* driving *UAS-hh* (Gift from Dr. Gary Struhl) was used for Hh misexpression in the A compartment. *221-Gal4* (Grueber et al 2003a) driving *UAS-EGFR-DN* (Gift from Dr. Gary Struhl) was used to knockdown EGFR signaling in class I neurons. *En-LacZ* was used to mark the P compartment. W^{1118} crossed with the appropriate Gal4 lines was used for controls. *elav-Gal80; en-Gal4, UAS-myr::GFP; UAS-nls-tdTomato* was used for P compartment sorting and *elav-Gal80; 35A08-Gal4, UAS-myr::GFP; UAS-nls-tdTomato* was used for A compartment

sorting. Elav-gal80, *UAS-myr::GFP* (JFRC12) and *UAS-nls-tdTomato* (JFRC105) were a gifts from Dr. Richard Mann's lab. All RNAi and misexpression screen lines were crossed to: *en-Gal4, UAS-mCD8::GFP*; *nompC-LexA, LexAop-mCD8::Cherry*. All screen RNAi lines were obtained from Bloomington or from Vienna *Drosophila* Research center (VDRC) if a Bloomington line was unavailable (see Table 4.4 for all screen lines used). *UAS-Luciferase.valium10* (BL 35788) was used as a control for RNAi knockdowns.

Immunohistochemistry

Dissections and staining procedures were performed as described in Chapter 3. The following primary antibodies were used: Rabbit anti-dsRed (1:200, Clontech), goat anti-HRP (1:200, Jackson ImmunoResearch 123-005-021), chicken anti-GFP (1:1000, Abcam, Cambridge, MA), mouse anti-βgal (1:10, DSHB), rabbit anti-βgal (1:1000, Cappel), rat anti-de-cadherin (1:10, DSHB). Rhodamine Red-X, Alexa Fluor 647, Alexa Fluor 488, and Cy2-conjugated secondary antibodies were used against the appropriate species (1:200; Jackson ImmunoResearch). goat anti-HRP-RRX conjugated (1:200 Jackson ImmunoResearch) was used on occasion.

Confocal image acquisition and dendrite analysis

Static images were acquired on a Zeiss LSM 700 confocal microscope using a 25X glycerol-immersion lens. Confocal images were processed with Fiji (Schindelin et al 2012) or Zeiss confocal software (Carl Zeiss, Germany).

Investigator was blind to genotype during all image quantifications except for Wnt4 misexpression p compartment size and all data from *yellow-d* and *mthl9* RNAi animals. To

analyze vpda and vdaD dendrite territory coverage, a modified Sholl analysis was used, similar to what was described in (Singhania 2014), except the Sholl was relative to the A-P compartment boundary. The A-P compartment boundary was traced in Fiji and drawn onto the anti-HRP or nompC-LexA channel (draw tool in to ROI manager). This single channel image was loaded into Adobe Illustrator CS6. The A-P compartment boundary was traced and then placed at 10 μm (vpda) or 15 μm (vdaD) distances, using the blend tool. Dendrite crossings at each of the intervals were recorded. The total number of dendrite crossings was summed and then the proportion of dendrite crossings at each interval to the total number of crossings was calculated. An additional modified Sholl was used for vdaD analysis in *yellow-d-RNAi* animals due to the shift in the A-P compartment boundary: analysis was performed as described above, but using 10-micron intervals relative to the medial muscle attachment site just anterior to the AP compartment boundary

Fiji was used to quantify primary dendrite position of vpda neurons. Irregular shapes were drawn between the A-P compartment boundary and the primary dendrite, and the areas of these shapes were measured. If the primary dendrite was posterior to the compartment boundary, the measured area was considered negative, and if the dendrite was anterior the area was positive. A sum of all these areas, divided by the length of the primary dendrite (to normalize for changes in dendrite length), was our measure of dendrite position. More negative values indicate a more posterior primary dendrite. Additionally, the ROI tool in Fiji was used to trace neurons to calculate total dendrite length, dendrite number, branchpoint number, and average length of Posterior-oriented or Anterior-oriented secondary dendrites. Average dendrite length was normalized by the length of the entire segment, to control for animal size

Estimated P compartment size was measured by drawing a rectangle around the P compartment, approximately the width of the primary dendrite length. The area of this rectangle was divided by the width of the rectangle to acquire an estimated length of the P compartment in the vpda region. This length was normalized by the estimated length of the entire segment (which was measured in the same manner as the estimated P compartment length) to control for variability in animal size. Shift in the A-P compartment boundary in *yellow-d* and *mthl9* knockdowns was quantified by measuring the distance between a medial muscle attachment site just anterior to the AP compartment boundary.

Statistical methods

Statistical tests and data plotting were performed using Microsoft Excel, RStudio, and Prism 7 or 8. Modified Sholl experiments were evaluated by a mixed-effects model or Repeated-Measured ANOVA with post-hoc Sidak's multiple comparisons test for each interval. All other experiments were evaluated by a two-tailed Student's t-Test with two-sample unequal variance. P-values are represented as: * < 0.05, ** < 0.01, and *** < 0.001.

qRT-PCR

Total RNA was treated with TURBO DNA-free Kit (Invitrogen) to remove all residual DNA before qRT-PCR. 2.2ng/µL of total RNA per sample (one P compartment sample and one A compartment sample) was then treated with Superscript IV Reverse Transcriptase (Invitrogen) to make cDNA. For qPCR amplification, PowerUp™ SYBR™ Green Master Mix was used in a 96-well plate on a real-time PCR cycler (Eppendorf Mastercycler EP Realplex, we thank the Lomvardas lab for generous use of this machine). Each sample was tested for *en, slp1, and wg*

expression, and normalized to *rpl32* expression as a housekeeping gene (primers used listed in table below). Three technical replicates were pipetted for each sample/primer combination. PCR cycling parameters were as follows: 95°C for 2 minutes, then 40 cycles of 1) 95°C for 15 seconds, 2) 55°C for 30 seconds 3) 72°C for 45 seconds. Following the cycles, a dissociation melting curve was performed to confirm a sharp peak, indicating a single PCR product per reaction. Proper controls (no template control and no amplification control) were included. Comparative Ct method was used for quantification (Schmittgen & Livak 2008).

Primers used for qPCR

Gene	Forward primer	Reverse primer
en	CAGCTCAGGACCCCGCTAC	CGTCTCCGCTCGGTCAGATA
slp1	AACACCGCAACTCAACCCAT	GGCTGTCGAAATCCTCCGAA
wg	CAAAATCGTTGATCGAGGCTGC	GATCTCGACTGGTGGCTGTAG
rpl32	ATGCTAAGCTGTCGCACAAATG (Ponton et al 2011)	GTTCGATCCGTAACCGATGT (Ponton et al 2011)

Embryo collection

Embryo collection and dissociation protocol as adapted from a protocol graciously provided by the Kohwi lab. To collect sufficient numbers embryos for cell dissociation, I set up large population (pop) cages with adult flies from 2 trays of 25 bottles. Population cages consisted of large plastic cylinders with mesh fabric attached on either end with 6-inch duct clamps (Hydrofarm). Flies were kept with a large grape agar plate with yeast paste. Egg laying is regulated by circadian rhythms: females flies tend to lay eggs just after lights off. Therefore, pop cages entrained in an incubator with a 12-hour light dark cycle for at least 2 days before embryo collection. To collect stage 12-14 embryos, flies laid eggs for 4 hours at 25 degrees C, 30 minutes after lights off, on a fresh grape agar plate with yeast. Before this egg laying session, there was a 1 hour “pre-lay” on a fresh agar plate, which helps with embryo collection quality.

Embryos were then aged at 18 degrees C for 17.5 hours before embryo dissociation (example timeline: 2pm-6pm egg lay, 11:30am dissociation).

Cell dissociation and *sorting*

After aging, embryos were rinsed into collection bottles with mesh and dechorionated with 3% hypochlorite bleach and thoroughly rinsed. Some embryos were mounted with glycerol and checked with brightfield imaging to confirm appropriate e staging. Approximately 33%-50% of the embryos were placed in a 40 mL capacity Dounce homogenizer filled with ice cold C&G media [Chang and Gehring's Balanced Saline (Minoree Kohwi, personal communication)] + 2% Fetal Bovine Serum (FBS) and homogenized with a loose pestle for 12-14 strokes. This was repeated 2-3 times to homogenize all the embryos. Cell suspension was transferred to 50mL conical tubes and centrifuged twice at 40g for 5-10 min to pellet the tissue debris. Supernatant was then transferred by pipette to 15 mL tubes and centrifuged for 10 min at 380g to pellet the cells (discard supernatant). Cells in each 15 mL tube were resuspended in 335 µL of 1x PBS and then filtered through a 30 µm cell strainer. Cells were stained with Calcein Violet 450AM Viability dye (eBioscience, 5-10 µM) and LIVE/DEAD™ Fixable Far Red Dead Cell Stain (Invitrogen, 1 µL per 1 mL cell suspension) at room temperature for 30 minutes, protected from light. Then, cells were washed twice by pelleting at 380g for 5 min and resuspending in 2 µL C&G + 2% FBS 2X. 20 µL of DNAse (Worthington, 10 mg/mL in water) was added to prevent cell clumping. Cells were kept on ice and mixed once more by pipetting, and then immediately taken to the FACS facility. With one person, this embryo dissociation procedure required 2-2.5 hours.

Sorting was performed in the core facility at the Zuckerman Institute's JLG Science Center with Ira Schieren. Live single cells were gated by size, Calcein Violet signal and lack of LIVE/DEAD signal. Cells of interest were sorted for high expression of GFP and tdTomato. 30,000-150,000 cells were collected per session, which likely varied depending on the number of embryos collected for dissociated. Cells were sorted directly intro Trizol for RNA extraction. Three different dissociation and sorting sessions were performed for each genotype, resulting in three biological replicates for each cell type (P compartment and A compartment cells).

RNA sequencing

RNA was extracted from sorted cells with the Direct-Zol microprep kit from Zymo. RNA concentrations ranged from 12-25 ng/μL per sort, as measured with the Qubit™ RNA high sensitivity assay. An aliquot of diluted RNA was assessed on an Agilent Bioanalyzer using the RNA Pico chip (Molecular Biology Services at the Molecular Pathology core, CUIMC) to check RNA quality. Unlike mammalian ribosomal RNA, *Drosophila* 28S rRNA breaks into two similar-sized fragments that appear close to the 18S rRNA band. Quality was assessed by ensuring that only two rRNA bands are visible with no other bands from degraded RNA (Harzer et al 2013).

Sequencing libraries were prepared separately for each biological replicate. To isolate mRNA from total RNA samples, polyA pull-down was performed with oligo dT beads from the NEBNext® Poly(A) mRNA Magnetic Isolation Module, from at least 60 ng total RNA per sample. NEBNext® Ultra II Directional RNA Library Prep Kit for Illumina was used to make libraries, according to the included protocol, along with AMPure XP beads for PCR purification. 75-bp single-end sequencing was performed using the Illumina Nextseq 550 system at the JLG

Science Center, yielding 17-30 million reads per sample (one sample had 17 million, rest all had >25 million).

Basespace (Illumina) was used to convert sequencing results to FASTQ format. The Galaxy web platform and the public server at usegalaxy.org (Afgan et al 2016) was used for differential expression analysis (n=3 biological replicates for each cell type). Sample results from multiple lanes were concatenated and then trimmed with the trimmomatic tool, to cut adapter sequences from the read (Bolger et al 2014). HISAT2 was used to align reads to the *Drosophila* genome (dm6 from UCSC genome browser) (Kim et al 2019). FeatureCounts was used to count reads associated with genes, and then edgeR was used to statistically identify differentially expressed genes (Liao et al , Robinson et al 2010).

Chapter 4 Figures and Tables

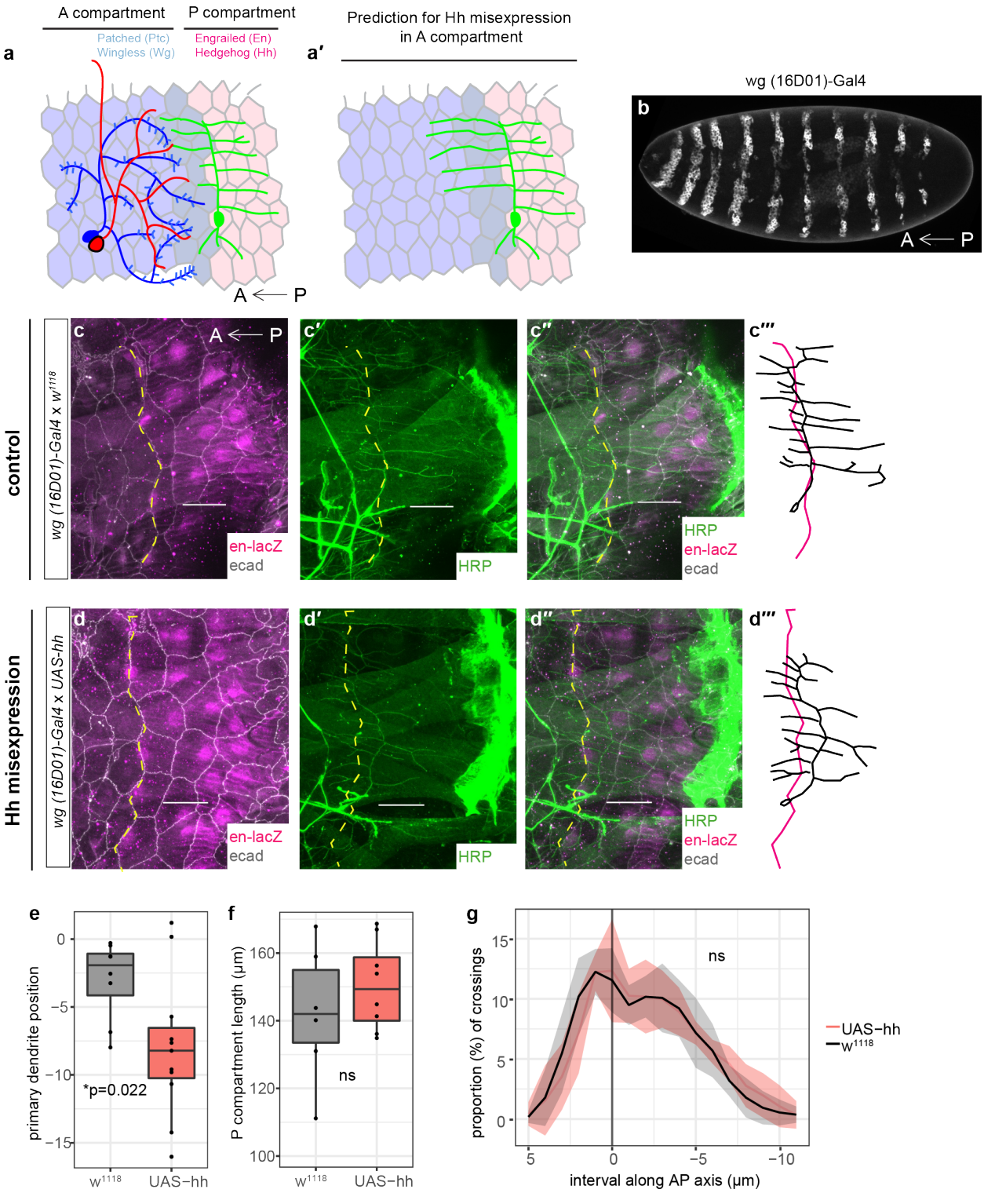

Figure 4.1. Hedgehog regulates vpda primary dendrite position, but not dendrite territory location
(a-a′) Schematic of the compartmental organization of dendrites and major known compartmental cues (a), and schematic of the prediction for changes in cI dendrites with Hedgehog (Hh) misexpression in the A compartment (a′). Hh is normally secreted from the Posterior (P) compartment. If Hh is attractive to cI dendrites, then we would expect misexpression in the A compartment to increase cI anterior-oriented dendrite length.
(**b**) Expression of *16D01(wg)-Gal4>UAS-mCD8::GFP* in a stage 12-14 embryo.
(c-c′′′) In a control animal, co-labeling of P compartment with *en-lacZ* (magenta), epidermal cell junctions with anti-de-cadherin (ecad) (grey), and vpda neurons with anti-HRP (green). (b) shows P compartment and ecad labeling, (b′) shows anti-HRP, and (b′′) shows merged image. (b′′′) shows vpda tracing, magenta line represents anterior-posterior compartment boundary.
(d-d′′′) Data shown as in (b-b′′′), for an animal with Hh $_{misexpression}$ in the A compartment [*16D01(wg)-Gal4>UAS-hh*].
(e) Quantification of primary dendrite position in w^{1118} control (n=7) and *16D01(wg)-Gal4>UAS-hh* (n=10) larvae. Dendrite position is quantified as the area between the primary dendrite and the A-P compartment boundary, normalized by the length of the primary dendrite. Negative values represent a posterior shift. Horizontal line represents median, whiskers represent data range, and points outside the box and whiskers represent outliers > 1.5 times the interquartile range. **p=0.022 by two-tailed, unpaired Student's t-Test.
(f) Quantification of P compartment length in w^{1118} control (n=9) and *16D01(wg)-Gal4>UAS-hh* (n=11) larvae. Boxplots plotted as in (d). Non-significant (ns): p=0.411 by two-tailed, unpaired Student's t-Test. No difference in compartment size indicates a movement of primary dendrite rather than the expansion of the P compartment.
(g) Modified sholl analysis of w^{1118} control (n=9) and *16D01(wg)-Gal4>UAS-hh* (n=11) larvae. Quantification of dendritic branch intersections at 10-micron intervals from the A-P compartment boundary, which is labeled as interval 0. Posterior intervals are negative, anterior intervals are positive. Plots represent mean ± s.d. Statistical significance was evaluated with a mixed-effects model with post-hoc Sidak's multiple comparisons test for each interval. p>0.45 (ns) at all intervals.
Anterior is to the left in all images.
Scale bars = 50 μm.

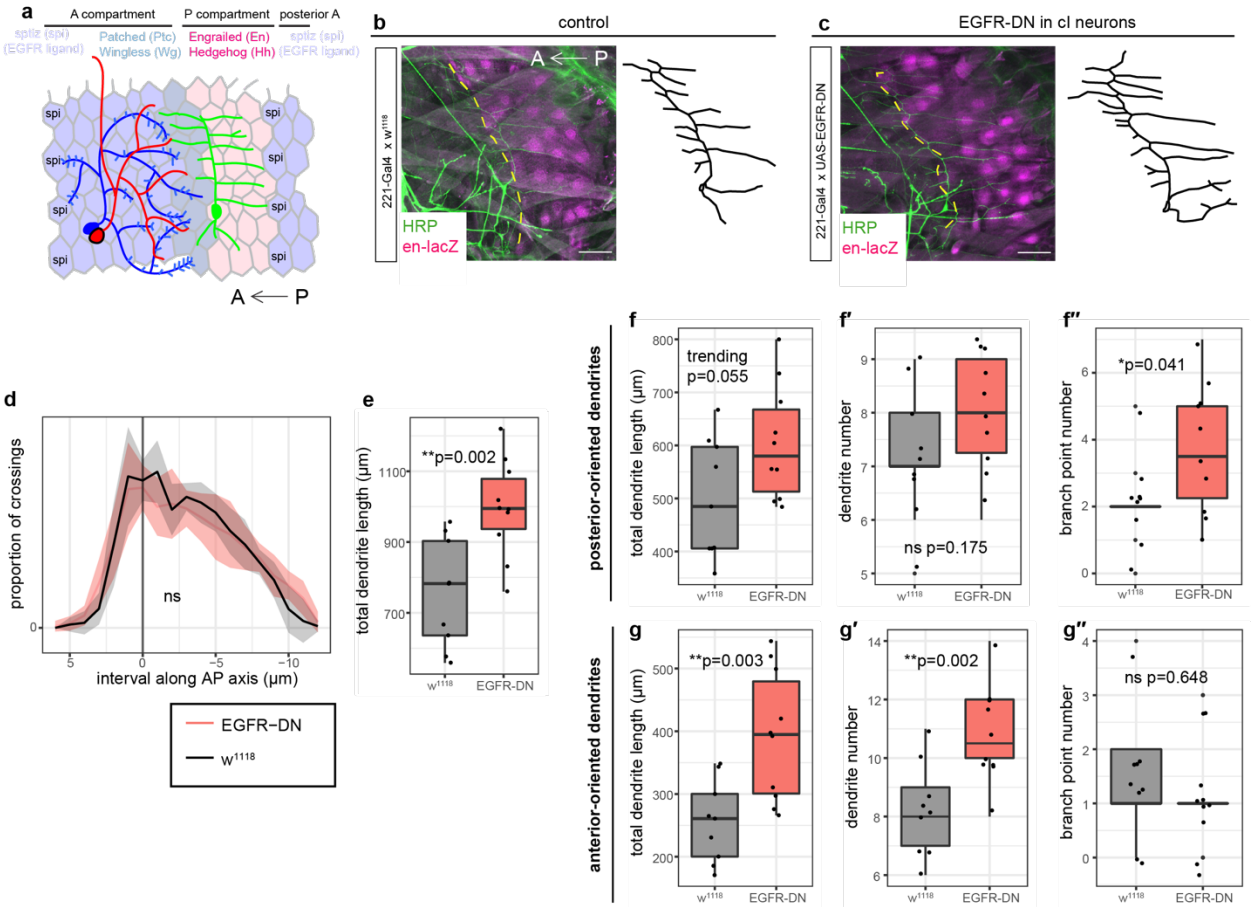

Figure 4.2. EGFR pathway regulates vpda total dendrite length, but not dendrite territory location
(a) Schematic of the compartmental organization of dendrites and major known compartmental cues. Spitz (Spi) an EGFR ligand, is secreted from the most anterior edge of the A compartment.
(b) In a control animal, co-labeling of P compartment with *en-lacZ* (magenta) and vpda neurons with anti-HRP (green). Class I tracing shown at right.
(c) Data shown as in (b) for an animal with EGFR dominant negative construct in class I neurons
(d) Modified sholl analysis of w^{1118} control (n=10) and *221-Gal4>UAS-EGFR-DN* (n=10) larvae. Quantification of dendritic branch intersections at 10-micron intervals from the A-P compartment boundary, which is labeled as interval 0. Posterior intervals are negative, anterior intervals are positive. Plots represent mean ± s.d. Statistical significance was evaluated with a mixed-effects model with post-hoc Sidak's multiple comparisons test for each interval. p>0.20 (ns) at all intervals.
(e) Quantification of total dendrite length of vpda in w^{1118} control (n=10) and *221-Gal4>UAS-EGFR-DN* (n=10) larvae. **p=0.002 by two-tailed, unpaired Student's t-Test.
(f-f′′′) Quantification of dendrite arbor morphology for posterior-oriented vpda dendrites in w^{1118} control (n=10) and *221-Gal4>UAS-EGFR-DN* (n=10) larvae. (f) total dendrite length, p=0.055 (trending but not significant). (f′) secondary dendrite number, not significant (ns) p=0.175. (f′′) number of branch points, *p=0.041. All p-values are evaluated by two-tailed, unpaired Student's t-Test. Trending increase in posterior total dendrite length is likely driven by significant increase in branch points.
(g-g′′′) Quantification of dendrite arbor morphology for anterior-oriented vpda dendrites in w^{1118} control (n=10) and *221-Gal4>UAS-EGFR-DN* (n=10) larvae. (g) total dendrite length, **p=0.003. (g′) secondary dendrite number, **p=0.002. (g′′) number of branch points, p=0.648. All p-values are evaluated by two-tailed, unpaired Student's t-Test. Significant increase in anterior total dendrite length is likely driven by significant increase in dendrite number.
For all boxplots, horizontal line represents median, whiskers represent data range, and points outside the box and whiskers represent outliers > 1.5 times the interquartile range.
Anterior is to the left in all images. Scale bars = 50 µm.

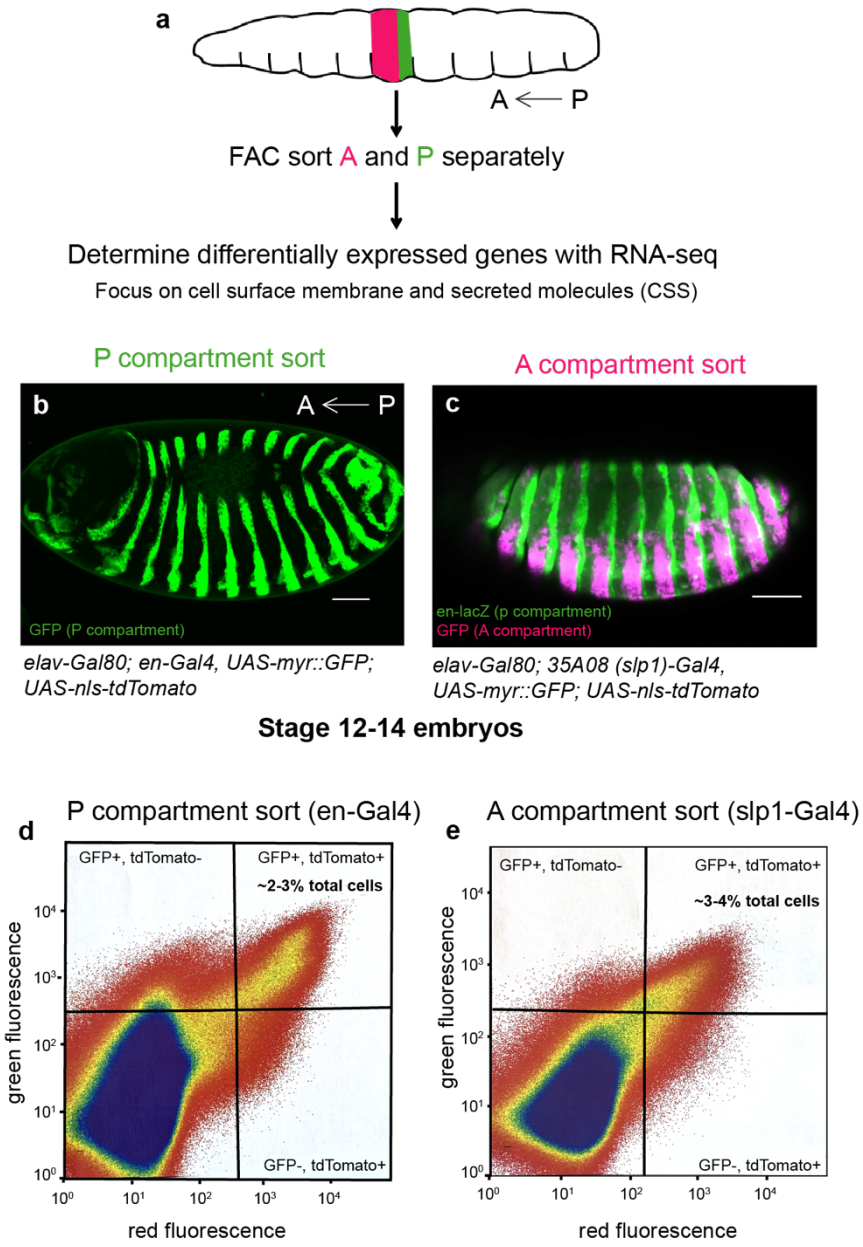

Figure 4.3. Purifying P compartment and A compartment epidermal cells from embryos
(a) Schematic of experimental strategy. P compartment is green and A compartment is magenta. FAC= Fluorescence Activated Cell.
(b) Confocal image of embryos dissociated for P compartment sorting. *Elav-Gal80; en-Gal4, UAS-myr::GFP; UAS-nls-tdTomato* embryos were sorted at stage 12-14. GFP channel is shown here in green. Anterior is to the left, dorsal is to the top.
(c) Confocal image of embryos dissociated for A compartment sorting. *Elav-Gal80; 35A08(slp1)-Gal4, UAS-myr::GFP;UAS-nls-tdTomato* embryos were sorted at stage 12-14. GFP channel is shown here in magenta, *en-lacZ* staining is shown in green as a reference. Anterior is to the left, dorsal is to the top.
(d) Example plot of green versus red fluorescence and gating parameters used to sort P compartment cells. Cells in the upper right quadrant, with both high GFP and tdTomato fluorescence, were sorted. This was ~2-2.75% of all cells in each sort (3 sorts performed).

(e) Example plot of green versus red fluorescence and gating parameters used to sort A compartment cells. Cells in the upper right quadrant, with both high GFP and tdTomato fluorescence, were sorted. This was ~3-4% of all cells in each sort (3 sorts performed).
Scale bars = 50 μm.

a

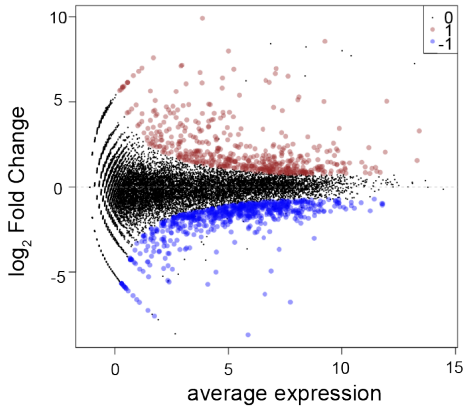

b

P vs A	Up	Flat	Down	
	500	33560	669	all genes
	132	1216	161	CSS genes

c

	Gene name (symbol)	Log_2 fold change	Log_2 counts per million	Adjusted p-value (FDR)
Knwon P genes	hedgehog (hh)	2.510	7.859	***7.550E-19
	engrailed (en)	0.276	-0.340*	1.000
Knwon A genes	sloppy paired 1 (slp1)	-1.481	8.821	***1.740E-07
	sloppy paired 2 (slp2)	-1.714	8.015	***2.990E-09
	wingless (wg)	-1.177	7.235	***3.962E-04
	patched (ptc)	-0.735	9.501	trend 0.051

Figure 4.4. RNA-seq differential expression analysis of P vs A compartment cells
(a) Mean-difference (MD) plots after edgeR analysis of 3 biological replicates of P compartment and A compartment cells. An MD plot visualizes the library size-adjusted log_2-fold change between two libraries (the difference) against the average log-expression across those libraries (the mean). Red dots indicate genes significantly enriched in the P compartment, blue dots indicate genes significantly enriched in the A compartment.
(b) Number of transcripts with significantly different expression between the P and A compartments. Upregulated genes are enriched in P, downregulated genes are enriched in A. Second row shows numbers for the subset of cell surface and secreted molecule (CSS) genes (see appendix A for complete list)
(c) EdgeR analysis results for genes previously known to be differentially expressed in the P and A compartments. All genes of interest showed expected expression patterns, except expression levels of *engrailed* (log counts per million) were very low (red text), so log-fold change is not significant and likely inaccurate. FDR=False Discovery Rate.

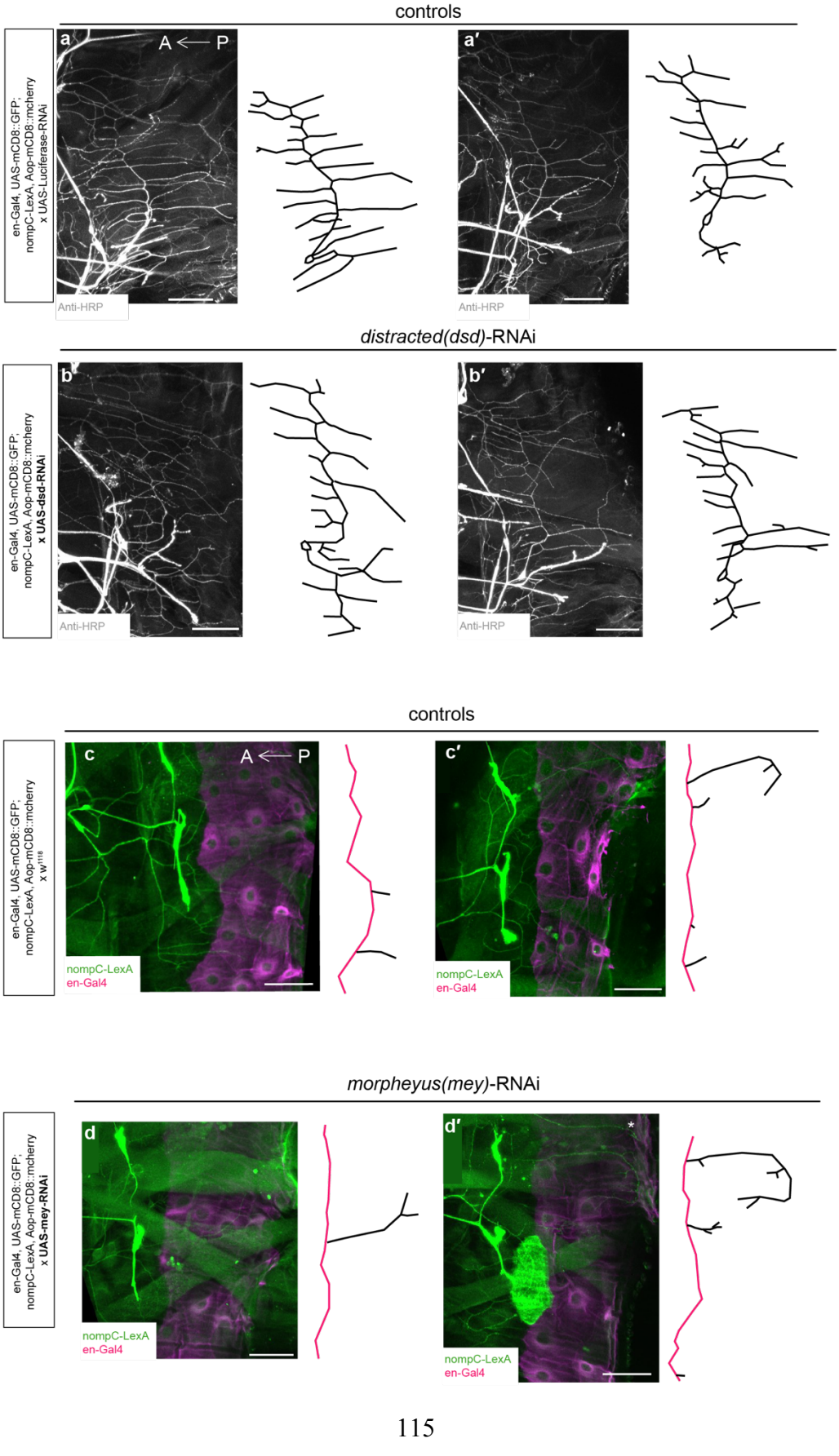
controls
en-Gal4, UAS-mCD8::GFP;
nompC-LexA, Aop-mCD8::mcherry
x UAS-Luciferase-RNAi
a
A ← P
a′
Anti-HRP
Anti-HRP
distracted(dsd)-RNAi
en-Gal4, UAS-mCD8::GFP;
nompC-LexA, Aop-mCD8::mcherry
x UAS-dsd-RNAi
b
b′
Anti-HRP
Anti-HRP
controls
en-Gal4, UAS-mCD8::GFP;
nompC-LexA, Aop-mCD8::mcherry
x w1118
c
A ← P
c′
nompC-LexA
en-Gal4
nompC-LexA
en-Gal4
morpheyus(mey)-RNAi
en-Gal4, UAS-mCD8::GFP;
nompC-LexA, Aop-mCD8::mcherry
x UAS-mey-RNAi
d
d′
*
nompC-LexA
en-Gal4
nompC-LexA
en-Gal4

Figure 4.5. Example images of sensory neurons showing potential effects from knockdown of CSS genes enriched in the P compartment

(a-a′) Confocal images of two control class I vpda neurons (screening line crossed with *luciferase-RNAi*, which is not present in *Drosophila* cells). Anti-HRP was used to label sensory neurons. Tracing of vpda to the right of each image. Note that control neurons show variability in number and length of secondary dendrites.

(b-b′) Confocal images of two class I vpda neurons with *distracted (dsd)* knocked down in the P compartment (screening line crossed with *dsd-RNAi*). Images and tracings shown as in (a-a′). Note that these vpda neurons may, on average, show fewer or shorter P-oriented dendrites, but a more detailed secondary screening is needed to evaluate any significant effects. Similar results were seen for *tsp-RNAi, fj-RNAi, and prc-RNAi.*

(c-c′) Confocal images of two control class III vdaD neurons (screening line crossed with w^{1118}). *NompC-LexA* (green) was used to label sensory neurons, *en-Gal4* (magenta) used to label the P compartment. Tracing of the A-P compartment boundary (magenta line) and the vdaD dendrites within the P compartment (black lines) are to the right of each image. Note that control neurons show variability, in that sometimes a single dendrite will grow well into the P compartment.

(d-d′) Confocal images of two class III vdaD neurons with *morpheyus (mey)* knocked down in the P compartment. (screening line crossed with *mey-RNAi*). Images and tracings shown as in (c-c′). Note that these vdaD dendrites may, on average, be more likely to grow into the P compartment, but a more detailed secondary screening is needed to evaluate any significant effects. Similar results were seen for *spz6-RNAi, pyr-RNAi*, and *UAS-toll6.*

Anterior is to the left in all images. Scale bars = 50 μm.

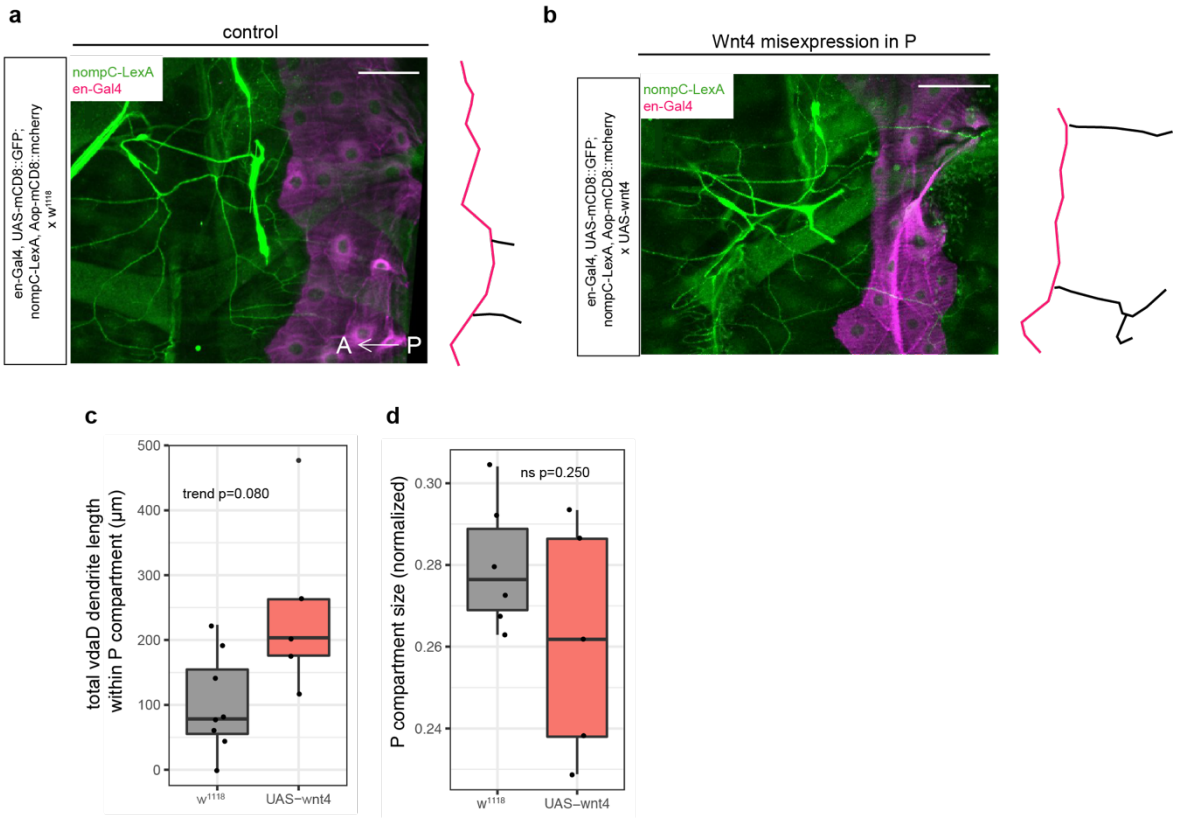

Figure 4.6. Misexpression of Wnt4 in the P compartment increases the likelihood of cIII vdaD dendrite growth into the compartment

(a) Confocal image of a control class III vdaD neuron. *NompC-LexA* (green) was used to label sensory neurons, *en-Gal4* (magenta) used to label the P compartment. Tracing of the A-P compartment boundary (magenta line) and the vdaD dendrites within the P compartment (black lines) are to the right of each image.

(b) Confocal image of a class III vdaD neuron in an animal where Wnt4 is misexpressed in the P compartment. Images and tracings are depicted as in (a). Note the increased dendrite growth within the P compartment.

(c) Quantification of total vdaD dendrite length within the P compartment (µm) in w^{1118} control (n=8) and *en-Gal4>UAS-wnt4* (n=5) animals. p=0.080 by two-tailed, unpaired Student's t-Test.

(d) Quantification of total P compartment size (normalized to segment size) in w^{1118} control (n=8) and *en-Gal4>UAS-wnt4* (n=5) animals. p=0.250 by two-tailed, unpaired Student's t-Test.

Anterior is to the left in all images. Scale bars = 50 µm.

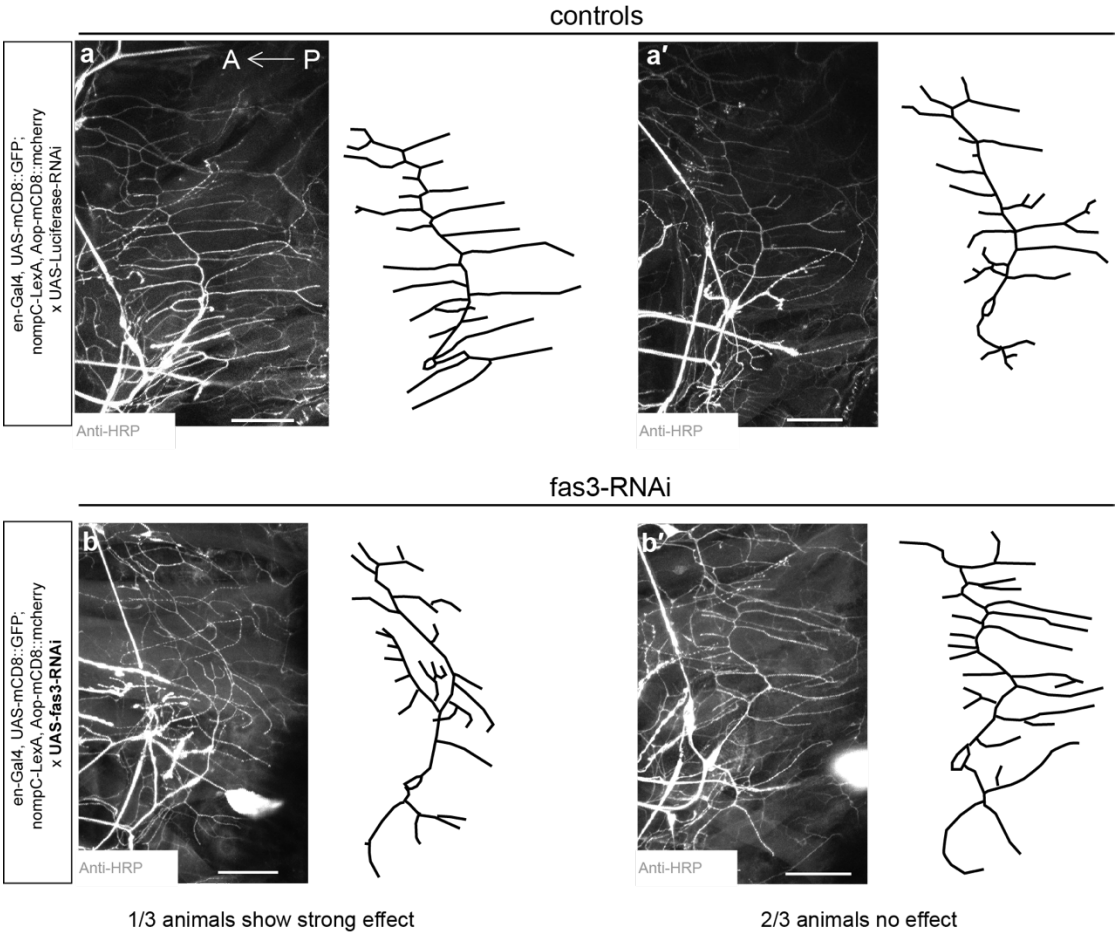

Figure 4.7. Example images of vpda neurons with *fas3* knockdown in the P compartment suggest occasional effect on dendrite branching and growth direction

(a-a′) Confocal images of two control class I vpda neurons (screening line crossed with *luciferase-RNAi*, which is not present in *Drosophila* cells). Anti-HRP was used to label sensory neurons. Tracing of vpda to the right of each image. Note that control neurons show variability in in number and length of secondary dendrites. Same images as in Figure 4.5.

(b-b′) Confocal images of two class I vpda neurons with *fasciclin 3 (fas3)* knocked down in the P compartment (screening line crossed with *fas3-RNAi*). Images and tracings shown as in (a-a′). 1 out of 3 animals showed neurons with aberrant dendrite branching.

Anterior is to the left in all images. Scale bars = 50 μm.

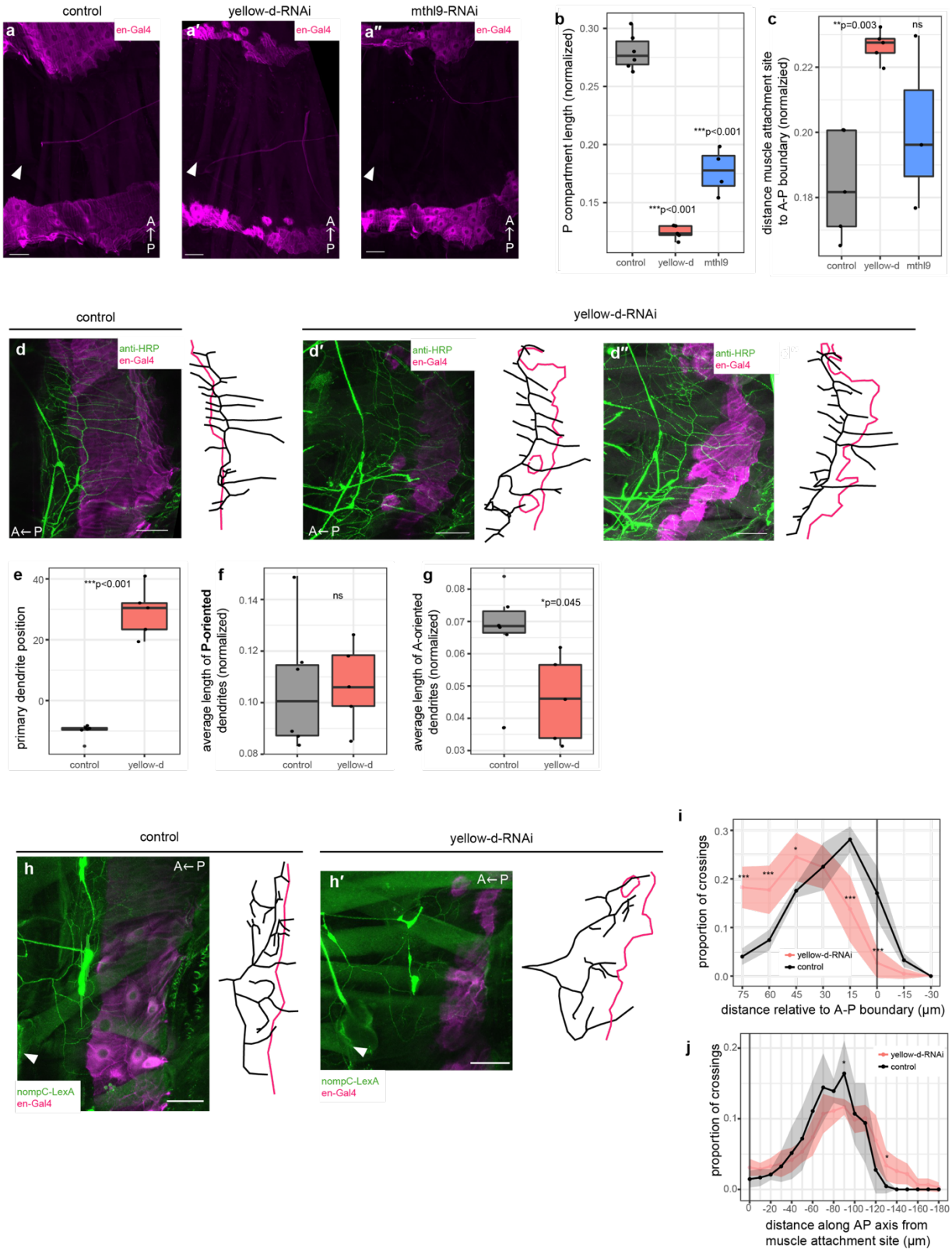
control
yellow-d-RNAi
mthl9-RNAi
a
a′
a″
en-Gal4
A
P
b
P compartment length (normalized)
***p<0.001
***p<0.001
control
yellow-d
mthl9
c
distance muscle attachment site to A-P boundary (normalzied)
**p=0.003
ns
control
yellow-d
mthl9
control
yellow-d-RNAi
d
d′
d″
anti-HRP
en-Gal4
A← P
e
primary dendrite position
***p<0.001
control
yellow-d
f
average length of P-oriented dendrites (normalized)
ns
control
yellow-d
g
average length of A-oriented dendrites (normalized)
*p=0.045
control
yellow-d
control
yellow-d-RNAi
h
h′
A← P
nompC-LexA
en-Gal4
i
proportion of crossings
yellow-d-RNAi
control
distance relative to A-P boundary (μm)
j
proportion of crossings
yellow-d-RNAi
control
distance along AP axis from muscle attachment site (μm)

Figure 4.8. Knockdown of *yellow-d* and *mthl9* shortens P compartment
(a-a″) Confocal images of the P compartment (magenta) in *luciferase-RNAi* controls (a) and with RNAi knockdown of *yellow-d* (a′) and *mthl9* (a″) in the P compartment with *en-Gal4*. Note the smaller size of the P compartment with RNAi knockdown. Anterior is to the top, lateral is to the right.
(b) Quantification of P compartment length, normalized to the size of the entire segment, for controls (n=6), *yellow-d-RNAi* (n=5), and *mthl9-RNAi* (n=4). ***p<0.001 for both *yellow-d-RNAi* vs. control and for *mthl9-RNAi* vs. control, by two-tailed, unpaired Student's t-Test.
(c) Distance from the medial muscle attachment site just anterior to the P compartment (see arrowheads in a- a″) to the A-P compartment boundary, normalized by segment length, for controls (n=5), *yellow-d-RNAi* (n=5), and *mthl9-RNAi* (n=3). **p=0.003 for *yellow-d-RNAi* and p=0.396 for *mthl9-RNAi* versus controls, by two-tailed, unpaired Student's t-Test.
(d-d″) Confocal images of vpda neurons (green) in controls (d) and with RNAi knockdown of *yellow-d* (d′-d″). Tracing of vpda (black) and the A-P compartment boundary (magenta) is to the right of each image. Anterior is to the left.
(e) Quantification of primary dendrite position in *luciferase-RNAi* controls (n=6) and with *yellow-d-RNAi* (n=5). Dendrite position is quantified as the area between the primary dendrite and the A-P compartment boundary, normalized by the length of the primary dendrite. Positive values represent an anterior shift. Note that while the P compartment is smaller with *yellow-d* knockdown, the primary dendrite no longer lies along the A-P compartment boundary, but anterior to it. ***p<0.001 by two-tailed, unpaired Student's t-Test.
(f) Quantification of average length of posterior-oriented dendrites (normalized by segment size) in *luciferase-RNAi* controls (n=6) and with *yellow-d-RNAi* (n=5). P=0.938 by two-tailed, unpaired, Student's t-Test. Location of primary dendrite seen in (d′-d″) seems to prevent development of shorter dendrites with a shorter compartment.
(g) Quantification of average length of anterior-oriented dendrites (normalized by segment size) in *luciferase-RNAi* controls (n=6) and with *yellow-d-RNAi* (n=5). *p=0.045 by two-tailed, unpaired, Student's t-Test.
(h-h′) Confocal images of class III vdaD neurons in *luciferase-RNAi* control (h) and with *yellow-d-RNAi* (h′). *NompC-LexA* (green) was used to label cIII neurons. Tracing of the A-P compartment boundary (magenta line) and the vdaD dendrites within the P compartment (black lines) are to the right of each image. Anterior is to the left.
(i-j) Modified sholl analyses of vdaD cells from *luciferase-RNAi control* (n=6) and *yellow-d-RNAi* (n=5) animals. (i) Dendritic branch intersections at 15-micron intervals from the A-P compartment boundary. Proportion of total crossings are plotted at each interval. (j) Dendritic branch intersections at 10-micron intervals along the A-P axis, starting with the medial muscle attachment site just anterior to the P compartment (see arrowheads in (h-h′)). Plots represent mean ± s.d. Statistical significance was evaluated with a Repeated Measured ANOVA with post-hoc Sidak's multiple comparisons test for each interval. * represents intervals with p<0.05, *** represents p<0.001.
For all box plots: horizontal line represents median, whiskers represent data range, and points outside the box and whiskers represent outliers > 1.5 times the interquartile range.
Scale bars = 50 μm.
A= anterior. P= posterior

Table 4.1. Top CSS gene candidates significantly enriched in the P compartment

Top CSS gene candidates significantly enriched in the P compartment						
Gene symbol	**Log2 fold change**	**Adjusted p-value (FDR)**	**In situ image available*?**	**Segmental expression**?**	**Tested in RNAi screen§?**	**Potential territory effects noticed†?**
LpR1	6.66	2.23E-27	yes	yes	yes	no
prc	5.02	3.21E-67	yes	yes, restricted laterally	yes	yes-cl
mthl6	4.33	2.37E-18	no		yes	no
mthl9	2.98	9.53E-25	yes	yes	yes	yes-compartment size
dyl	2.91	0.0163	yes	yes	yes	no
Nep1	2.73	0.0065	yes	yes, but lateral/dorsal	yes	no
hh	2.51	7.55E-19	yes	yes		
Tsp	2.32	8.79E-10	yes	yes	yes	yes-cl
C901	2.19	7.12E-14	no		yes	no
mey	2.16	0.0042	yes	yes	yes	yes-clII
dsd	2.10	7.54E-06	yes	yes	yes	yes-cl
Cad89D	2.07	7.33E-13	no		no	
Osi7	2.05	1.92E-15	yes	yes	yes	no
Ptp52F	1.97	1.81E-06	no		yes	no
Osi6	1.93	2.32E-11	yes	yes	yes	no
upd2	1.90	1.23E-04	no		no	
Spn100A	1.85	8.98E-12	yes	yes	yes	no
dpp	1.85	1.30E-08	yes	yes	yes	no
pyr	1.56	4.53E-08	no		yes	yes-clII
slow	1.41	0.0177	yes	yes	yes	no
spz6	1.36	1.36E-06	yes	yes. broad expression but some segmental pattern	yes	yes-clII
Osi14	1.33	0.0019	yes	yes, but mostly in trachea	no	
mthl2	1.30	0.0303	no		yes	no
yellow-d	1.23	0.0183	no		yes	yes-compartment size
Cys	1.14	6.14E-05	yes	yes	no	
yellow-e2	1.11	0.0008	no		no	
fj	1.09	0.0004	yes	yes	yes	yes-cl
Osi24	1.08	0.0031	yes	yes	no	
Tsp42Ef	1.04	0.0020	yes	yes	yes	no
Fas3	1.03	0.0006	yes	yes	yes	no††
spz4	0.87	0.0447	no		no	
ft	0.79	0.0227	yes	yes	yes	no

* Indicates if in situ expression pattern image available at BDGP (insitu.fruitfly.org) or Fly-FISH (fly-fish.ccbr.utoronto.ca)

** Indicates if the available in situ images show a segmental expression pattern

§ Indicates if we have screened animals with this gene knocked down in the P compartment

† Indicates if potential effects were noticed by eye

†† No territory effects noticed, but other dendrite effects seen (see chapter text)

Blue highlight indicate strongest effects noticed by eye

Table 4.2. Top CSS gene candidates significantly enriched in the A compartment

Top CSS gene candidates significantly enriched in the A compartment						
Gene symbol	**Log2 fold change**	**Adjusted p-value (FDR)**	**In situ image available*?**	**Segmental expression**?**	**Tested in misexpression screen§?**	**Potential territory effects noticed†?**
frac	-4.84	9.75E-09	yes	yes		
Nlg1	-3.79	0.0005	yes	yes		
Nrx-1	-3.59	3.79E-08	no			
Con	-3.02	1.77E-28	no			
SP1029	-2.72	2.13E-05	yes	yes		
beat-IV	-2.35	0.0013	no			
Nlg3	-2.28	0.0077	no			
Tsp5D	-2.23	0.0003	no			
Drl-2	-2.07	5.49E-10	no			
beat-VII	-1.88	0.0002	no			
grk	-1.86	8.64E-05	no		yes	no
Cubn	-1.71	2.78E-09	no			
nord	-1.62	0.0020	yes	no		
kek2	-1.60	8.78E-08	no			
dpr4	-1.59	0.0003	no			
beat-VI	-1.52	0.0011	no			
SP2353	-1.48	4.49E-06	no		yes	no
gogo	-1.45	2.83E-07	no			
Fas2	-1.31	5.13E-06	yes	yes		
tld	-1.27	0.0045	yes	yes		
Wnt4	-1.18	0.0004	yes	yes	yes	yes- cIII
wg	-1.18	0.0004	yes	yes		
Toll-6	-1.17	0.0036	yes	yes	yes	yes- cIII
klg	-1.16	7.51E-05	no			
DIP-epsilon	-1.12	0.0045	no			
Sema2b	-1.08	0.0013	no		yes	no
Cad88C	-1.01	0.0073	no			
Ptp99A	-0.94	0.0127	no			
kirre	-0.88	0.0364	no			
tutl	-0.87	0.0375	yes	no		

* Indicates if in situ expression pattern image available at BDGP (insitu.fruitfly.org) or Fly-FISH (fly-fish.ccbr.utoronto.ca)

** Indicates if the available in situ images show a segmental expression pattern

§ Indicates if we have imaged animals with this gene mixexpressed in the P compartment

† Indicates if potential effects were noticed by eye

Blue highlight indicate strongest effects noticed by eye

Table 4.3. Cuticle-related gene candidates

Cuticle-related genes significantly enriched in the P compartment			
Gene symbol	**Gene name**	**Log2 fold change**	**Adjusted p-value (FDR)**
CG32302		**6.71**	2.40E-22
TwdlO	TweedleO	**6.54**	0.0007
CG1136		**4.74**	4.09E-09
CG11584		**4.58**	0.0109
TwdlN	TweedleN	**4.35**	2.02E-08
Cpr66Cb	Cuticular protein 66Cb	**3.91**	0.0004
Cpr65Ea	Cuticular protein 65Ea	**3.72**	6.71E-08
CG13297		**2.96**	2.16E-10
TwdlD	TweedleD	**2.94**	4.36E-07
TwdlM	TweedleM	**2.83**	0.0088
Cpr51A	Cuticular protein 51A	**2.22**	8.18E-07
CG5756		**1.98**	0.0010
Cda4	Chitin deacetylase-like 4	**1.77**	3.24E-07
CG12009		**1.68**	0.0406
TwdlF	TweedleF	**1.54**	0.0021
obst-B	obstructor-B	**1.51**	4.46E-07
verm	vermiform	**1.50**	2.34E-05
ect	ectodermal	**1.41**	3.17E-07
Gasp	Gasp	**1.39**	4.53E-06
Cht7	Chitinase 7	**1.20**	4.86E-05
Cht5	Chitinase 5	**1.20**	0.0006
obst-A	obstructor-A	**0.94**	0.0086
Cuticle-related genes significantly enriched in the A compartment			
CG10140		**-4.29**	0.0304
Cht10	Chitinase 3	**-4.29**	0.0305
CG42367		**-2.09**	0.0431

Table 4.4. List of all RNAi and misexpression lines used for screening

Overexpression lines	
Gene symbol	**Line identifier BL=Bloomngton VDRC=Vienna**
grk	BL 58417
SP2353	Grueber lab stocks
Wnt4	BL 80070
Toll-6	BL 64074
Sema2b	BL 65748
RNAi lines	
LpR1	BL 50737
prc	BL 65898
mthl6	BL 44497
mthl9	BL 62896
dyl	VDRC 102166
Nep1	BL 65960
Tsp	BL 44116
C901	VDRC 103450
mey	VDRC 106568
dsd	BL 53318
Osi7	VDRC 100174
Ptp52F	BL 64940
Osi6	BL 58127
Spn100A	BL 62416
pyr	BL 63547
slow	VDRC 106464
spz6	BL 57510
mthl2	BL 65041
yellow-d	BL 62366
fj	BL 60011
Tsp42Ef	VDRC 8712
Fas3	BL 77396
ft	BL 34970

Chapter 5. Summary and future directions

Across the diversity of neuronal types, dendritic fields vary considerably in their shape, size, territory, and branching pattern. Neural function and circuit wiring depend critically on these features. In sensory neurons, dendritic field shape determines the shape of the receptive field, and the exact placement of the field determines the sensory input that is sampled. In this thesis, I used the *Drosophila* larva peripheral nervous system (PNS) as a model to investigate the relationship between dendritic arbor territories and sensory function, and the developmental mechanisms that properly pattern these arbors. As part of this study, I used a recently-developed live imaging technique to monitor body-wide proprioceptive activity dynamics, which revealed a strong relationship between activity timing and dendritic field targeting. Furthermore, I found evidence for an instructive role for compartment cues within the epidermal substrate in patterning dendritic fields of different sensory modalities to functionally appropriate positions on the body wall. I identified the suite of genes expressed in epidermal compartments and made progress towards identifying the molecular cues that may act upon dendrites during their development.

Characterization of proprioceptive system dynamics in behaving Drosophila larvae

To examine the relationship between dendritic fields and sensory activity, I focused on the larval proprioceptive system. Proprioceptors show diverse dendrite morphologies and territories, including bipolar dendrite (bd), dmd1, and class I dendritic arborization (cI da) neurons in each segment. In collaboration with Elizabeth Hillman's lab, we used high-speed, volumetric, Swept Confocally Aligned Planar Excitation (SCAPE) microscopy (Bouchard et al

2015, Hillman et al 2018) to simultaneously monitor the dendrite deformation dynamics and sensory activity of these cells in a crawling animal.

Imaging revealed that each neuron subtype responds in sequence, and the activity timing of each cell correlates with its dendrite deformation dynamics [see Chapter 2 and (Vaadia et al 2019)]. Dbd neurons show two dendrite bundles that span each segment from anterior to posterior, and these are the only imaged neurons that increase activity during segment stretch. Dmd1 neurons have one large dendrite bundle that targets the internal intersegmental nerve [ISN; (Corty et al 2016)], which lies along the muscle layer, and this organization likely supports the observed response from dmd1 at the start of segment contraction. Within a segment, each of the three cI da arbors target selective areas of the epidermis (Grueber et al 2002), and the location of each neuron arbor correlates with activity timing as the contraction moves from posterior to anterior through the segment. These results suggest that arbor shape and targeting endow each proprioceptor with a specific role in monitoring body wall deformation. Furthermore, our data provide new insights into the body-wide dynamics of the proprioceptive system, which inform models of sensory feedback during locomotion.

These findings and the development of this technique open up a number of promising avenues for future experiments. The current results show a correlation between dendritic arbor morphology/targeting and sensory activity timing. It would be interesting to adjust arbor targeting and then evaluate changes in sensory activity patterns with SCAPE. The genetic pathways required for targeting of these cells are largely unknown, but they may become available as investigation of patterning mechanisms continues. How would activity change if the dmd1 bundle was mistargeted to the epidermis, or if a cI neuron's territory coverage was shifted or expanded? Would a change in activity affect crawling behavior? These types of experiments

could also be extended to other sensory modalities to investigate the relationship between dendrite arbor patterning and touch-sensing or nociceptive function in cIII-cIV neurons.

More is known about the molecular pathways that regulate da neuron attachment to the extracellular matrix (ECM) at the basal surface of the epidermis, so currently tools exist to investigate the relationship between ECM attachment and sensory function (Kim et al 2012). Previous work on the role of ECM attachment has focused on its importance for dendrite self-avoidance and field patterning (Han et al 2012, Kim et al 2012, Meltzer et al 2016, Tenenbaum et al 2017, Yang et al 2019) [see Chapter 1 for details], but a recent study suggests that a wild-type balance of cIV arbor attachment versus epidermal enclosure is important for nociceptive sensitivity (Jiang et al 2019). Nearly all cI arbors show a near complete attachment to the extracellular matrix (ECM), which is maintained by integrin expression (Kim et al 2012). Class II dendrites show similar levels of attachment as cI dendrites, while cIII dendrites are mostly attached to the ECM but show some dendrite enclosures. It would be interesting to investigate if there is a change in activity patterns or signal strength after disrupting this attachment.

In addition to dendrite targeting and morphology, mechanosensory channels also play an important role for determining cell activity. Responses in cI neurons rely on the mechanosensory channel TMC (He et al 2019). In a reduced prep, stretch-activated mechanotransduction in dbd neurons relies on Piezo channels (Suslak et al 2015), but the role of Piezo for dbd activity in a crawling animal is unclear. While dbd and vbd neurons show similar dendrite morphologies, they show opposite responses to segment stretch in crawling animals, suggesting these differences may be due to differences in mechanosensory channel expression [see Chapter 2 and (Vaadia et al 2019)]. As additional important mechanosensory molecules are discovered, SCAPE could be used to image activity in proprioceptors with mutated channels, or with ectopic

expression of channels characteristic of a different subtype. These studies could reveal how different mechanosensory channels regulate sensory activity patterns.

While previous silencing experiments indicated that feedback from cI, bd, and dmd1 neurons is essential for regulating locomotion (Hughes & Thomas 2007), it is unclear what the specific role is for each individual cell type. Future studies could develop genetic tools to target individual cell types, or even individual cells within segments. These tools could be used to suppress the activity of specific cells with optogenetics and evaluate the effect on behavior. Behavior can be monitored with frustrated total internal reflection (FTIR) imaging and changes to behavior can be evaluated with automatic behavioral tracking software (Risse et al 2017, Risse et al 2014).

Proprioceptive feedback is also likely to affect behaviors beyond crawling, such as turning, nocifensive rolling (Burgos et al 2018, Hwang et al 2007), self-righting, and general posture (Heckscher et al 2015). It would be interesting to investigate whether proprioceptor subtypes have specific functional roles during these behaviors. In our work, we revealed that class I neuronal responses can encode simultaneous head turning and retraction behavior [see Chapter 2 and (Vaadia et al 2019)]. It would be interesting to use SCAPE to monitor the activity of the entire proprioceptive system during diverse behaviors, and to determine if optogenetic silencing of specific subtypes affects these behaviors.

Future studies could also investigate how proprioceptive feedback affects downstream circuits. An electron microscopic reconstruction of the larval CNS is almost complete (Eichler et al 2017, Schneider-Mizell et al 2016), and has revealed the connections between sensory inputs, interneurons, and motor outputs. Additionally, functional studies have implicated roles for different subsets of interneurons in controlling the pattern of motor activity within and between

segments during crawling. For example, Period-Positive Median Segmental Interneurons (PMSIs) promote segment relaxation and anterior wave propagation (Kohsaka et al 2014). Connectome data indicates that ddaD, vbd, and dmd1 proprioceptors synapse directly onto these PMSI neurons (Schneider-Mizell et al 2016), suggesting at least one role for these contraction-sensing proprioceptor subtypes may be to signal successful segment contraction and promote forward locomotion. In another circuit, A27h interneurons act through GDL interneurons to inhibit contraction in neighboring anterior segments, thereby preventing premature wave propagation (Fushiki et al 2016). Connectome data indicates that vpda neurons provide input onto A27h, suggesting feedback from vpda could contribute to proper timing of contraction in anterior segments during forward crawling. SCAPE imaging could be used to test these models of proprioceptive feedback by monitoring the relationship between sensory activity and downstream interneuron activity in crawling animals. Furthermore, an optogenetic set up within the SCAPE system could be used to perturb the activity of sensory cells and evaluate changes in interneurons and behavior. These types of experiments could reveal how proprioceptive feedback affects the larval crawling central pattern generator (CPG).

Substrate cues regulate the compartmental organization of sensory dendrites

In proprioceptive and other sensory neurons, dendritic field shape and location determines the sensory input that is sampled. How is dendrite territory coverage specified during development, and how does coverage support a specific sensory function? To investigate these questions, I focused on proprioceptive (cI) and touch-sensing (cII-cIII) da neurons, which tend to cover non-overlapping, neighboring, areas of the body wall, especially in the ventral cluster. In contrast to prior studies of tiling cIV da neurons, ablation studies indicate that repulsive

interactions between heterotypic dendrites are not required for specifying territory coverage. Instead, dendrite boundaries correlate with Anterior (A)-Posterior (P) compartment boundaries in the underlying epidermal substrate: proprioceptive cI dendrites target the P compartment (as defined by Engrailed expression), while touch-sensing dendrites are mostly contained within the A compartment. Genetic expansion of the P compartment leads to expansion of cI dendrites, suggesting that compartment cues in the epidermal substrate instruct dendrite targeting.

SCAPE imaging revealed that the ventral P compartment correlates with a major cuticle fold that occurs during crawling. These results suggest that proprioceptive dendrites target areas that bend predictably during crawling, while touch-sensing dendrites could be avoiding those areas to be tuned for external mechanosensory stimuli instead. In all, these results support a model in which dendrite targeting by compartment cues is a reliable and robust strategy for tuning sensory neurons for appropriate, predictable, stimuli on the body wall.

Interestingly, both body wall dynamics and sensory organization are different in the dorsal body wall. While cI ddaE dendrites target the P compartment in a similar manner to cI vpda, cI ddaD dendrites arborize within the dorsal A compartment. This dendrite organization corresponds to body wall dynamics: in contrast with the ventral side, dorsal cuticle folding is distributed across the segment. Furthermore, cIII dendrites do not avoid the P compartment on the dorsal side. If compartment cues are an important regulator of class-specific dendrite targeting, one important question is how some cells escape this restriction.

I performed further experiments to investigate the molecular identity of the substrate cues guiding the compartmental organization of sensory dendrites. I tested cues that are already known to be expressed in a compartment-restricted fashion (Hedgehog and EGFR pathways), however the main dendrite territory footprint of ventral cI proprioceptive cells was unaffected by

these cues. To find new candidates, I developed an approach for cell sorting and RNA sequencing of epidermal cells in different compartments. I identified 290 cell surface and secreted (CSS) molecules differentially expressed between the A and P compartments. I performed an initial knockdown and misexpression screen with ~30 of these genes to test for roles in cI and cIII territory formation. While none of these targets can alone fully explain compartmentalized dendrite targeting, several candidates emerged from the screen, and the results provide a foundation for future secondary screening efforts. Taken together, these results reveal important advances in our understanding of how dendritic fields are patterned to support proper sensory function.

In the future, it would be interesting to complete the knockdown and misexpression screen of the 290 identified compartmentally-expressed CSS genes. While the current study focused on manipulating the P compartment by knocking down P-enriched genes or misexpressing A-enriched genes, an ideal screen would also manipulate the A compartment by knocking down A-enriched genes and misexpressing P-enriched genes. Additionally, an ideal screen would develop a QF or LexA line to easily distinguish cII dendrite territories, so these cells can be evaluated in addition to the cI and cIII neurons evaluated in this study. Furthermore, future studies could aim to develop semi-automated pipelines to analyze the dendrite territory coverage of all screen images, thereby more easily identifying screen hits.

Our findings open up a number of possibilities for future experiments. To test our model of the sensory function of compartmental organization, the ideal experiments would manipulate territory coverage and then test sensory activity with SCAPE imaging. Our model predicts that growth of ventral cII or cIII dendrites into the P compartment would lead to increased activity of these neurons during crawling. Conversely, we predict that loss of cI dendrite targeting to the P

compartment would diminish their robust responses during the contraction phase of crawling. As we investigate the developmental mechanisms that target these dendrites, we may reveal genetic manipulations that will allow us to perform these functional investigations.

It is possible that compartment cues in the substrate act redundantly with repulsive, heterotypic dendrite-dendrite interactions to pattern proprioceptive and touch sensing dendrites. To test this possibility, future experiments could simultaneously ablate neurons and misexpress or knock down promising compartment cues. For example, the territory footprint of ventral cI (vpda) proprioceptive cells remained unchanged with ablation of neighboring cII/cIII neurons or with misexpression of Hedgehog in the A compartment. It would be interesting to evaluate vpda territories with simultaneous ablation and Hedgehog misexpression. Furthermore, manipulation of some candidates (e.g. *mey* knockdown, *wnt4* misexpression, see Chapter 4) caused a minor increase in cIII territory growth into the P compartment. It will be important to determine whether manipulation of those substrate cues in combination with ablation of neighboring vpda neurons leads to a stronger effect on territory expansion.

If specific compartment cues are identified as important for patterning sensory dendrites, these molecules may be relevant to a wide range of systems. The dendrites of the *Drosophila* larval motor system also show a compartment organization: dendrites of motor neurons that target internal muscles are restricted to the *engrailed* domain of the ventral nerve cord, while dendrites of motor neurons that project to external muscles arborize in a complementary region. Similar to what was observed with da neurons, this organization is not due to repulsive interactions between neighboring dendrites and is unaffected by knockdown of classic compartment cues such as Hedgehog (Landgraf et al 2003). Since compartment specification is important for both body wall and nervous system patterning in *Drosophila,* an appealing model

is one in which compartment cues coordinate the patterning of the body wall, PNS, and CNS. In vertebrates, the hindbrain is segmented into seven lineage-restricted compartments, known as a rhombomeres, along the AP axis (Kiecker & Lumsden 2005). While it is unknown if there are dendrites that show a compartmental organization in the vertebrate brain, the importance of compartments for nervous system patterning suggests that mechanisms that target neurites within specific compartments may be conserved across species.

Our list of differentially expressed genes in the P versus A compartments is relevant for diverse future studies. For example, our dataset revealed candidate molecules that could underlie potential cuticle differences in the A and P compartments. The epidermis secretes a cuticle that functions as an exoskeleton, and the observed preferential distortion of the P compartment during crawling could be related to a specialized protein composition that regulates the physical properties of the cuticle. Supporting this idea, 25 potentially cuticle-related genes are differentially expressed between the P and the A compartments (see Chapter 4, Table 4.3). Future experiments could knock down or misexpress these genes and evaluate the effect on the physical properties of the cuticle and body wall dynamics with SCAPE imaging. Compartmental organization of both dendrites and cuticle composition could be an efficient mechanism to coordinate the patterning of sensory dendrite territories with the development of the appropriate properties of the underlying substrate (e.g. matching proprioceptive dendrite targeting to a flexible cuticle region).

Additionally, future studies could compare gene expression of the embryonic epidermal compartments to imaginal disc compartments, which could help reveal general principles of compartment specification within tissues. General mechanisms include those that mediate

adhesion between homotypic epithelial cells and repulsion between heterotypic cells to form a sharp compartment boundary.

Conclusion

The shape, size, and territory of dendritic fields is a critical determinant of neural function. The work presented here reveals important advances in our understanding of how diverse dendritic arbors are built and how the morphologies and territories of these arbors support diverse sensory functions. We developed an imaging platform to simultaneously monitor sensory activity and dendrite deformation in crawling animals. Each proprioceptor type shows unique activity patterns, which correlate with the unique dendrite targeting and deformation dynamics of each cell type. This technique can be extended to further explore the relationship between dendrite structure and function and to examine the function of sensory feedback for modulating a locomotor CPG. I also show evidence for an instructive role for compartment cues within the epidermal substrate for targeting dendritic fields to functionally appropriate locations on the body wall, while making progress towards identifying the essential molecular cues. These mechanisms should be relevant to a wide range of systems for linking nervous system and body plan organization. Taken together, our results reveal new insights into how dendritic fields are patterned to support proper neural function.

References

Afgan E, Baker D, van den Beek M, Blankenberg D, Bouvier D, et al. 2016. The Galaxy platform for accessible, reproducible and collaborative biomedical analyses: 2016 update. *Nucleic Acids Res* 44: W3-W10

Alivisatos AP, Chun M, Church GM, Greenspan RJ, Roukes ML, Yuste R. 2012. The brain activity map project and the challenge of functional connectomics. *Neuron* 74: 970-4

Bhat KM. 1999. Segment polarity genes in neuroblast formation and identity specification during Drosophila neurogenesis. *Bioessays* 21: 472-85

Blair SS. 1997. Limb development: marginal fringe benefits. *Current biology : CB* 7: R686-90

Bodmer R, Jan YN. 1987a. Morphological differentiation of the embryonic peripheral neurons in Drosophila. *Roux Arch Dev Biol* 196: 69-77

Bodmer R, Jan YN. 1987b. Morphological differentiation of the embryonic peripheral neurons in Drosophila. *Roux's Archives of Developmental Biology* 196: 69-77

Bolger AM, Lohse M, Usadel B. 2014. Trimmomatic: a flexible trimmer for Illumina sequence data. *Bioinformatics* 30: 2114-20

Bouchard MB, Voleti V, Mendes CS, Lacefield C, Grueber WB, et al. 2015. Swept confocally-aligned planar excitation (SCAPE) microscopy for high speed volumetric imaging of behaving organisms. *Nature photonics* 9: 113-19

Brunet I, Weinl C, Piper M, Trembleau A, Volovitch M, et al. 2005. The transcription factor Engrailed-2 guides retinal axons. *Nature* 438: 94-8

Burgos A, Honjo K, Ohyama T, Qian CS, Shin GJ, et al. 2018. Nociceptive interneurons control modular motor pathways to promote escape behavior in Drosophila. *eLife* 7

Burke RE. 2007. Sir Charles Sherrington's the integrative action of the nervous system: a centenary appreciation. *Brain* 130: 887-94

Calhoun AJ, Murthy M. 2017. Quantifying behavior to solve sensorimotor transformations: advances from worms and flies. *Curr Opin Neurobiol* 46: 90-98

Chen TW, Wardill TJ, Sun Y, Pulver SR, Renninger SL, et al. 2013. Ultrasensitive fluorescent proteins for imaging neuronal activity. *Nature* 499: 295-300

Cheng LE, Song W, Looger LL, Jan LY, Jan YN. 2010. The role of the TRP channel NompC in Drosophila larval and adult locomotion. *Neuron* 67: 373-80

Chhetri RK, Amat F, Wan Y, Hockendorf B, Lemon WC, Keller PJ. 2015. Whole-animal functional and developmental imaging with isotropic spatial resolution. *Nat Methods* 12: 1171-8

Clark MQ, Zarin AA, Carreira-Rosario A, Doe CQ. 2018. Neural circuits driving larval locomotion in Drosophila. *Neural Dev* 13: 6

Corty MM, Tam J, Grueber WB. 2016. Dendritic diversification through transcription factor-mediated suppression of alternative morphologies. *Development (Cambridge, England)* 143: 1351-62

Couton L, Mauss AS, Yunusov T, Diegelmann S, Evers JF, Landgraf M. 2015. Development of connectivity in a motoneuronal network in Drosophila larvae. *Current biology : CB* 25: 568-76

Crisp S, Evers JF, Fiala A, Bate M. 2008. The development of motor coordination in Drosophila embryos. *Development (Cambridge, England)* 135: 3707-17

Cubelos B, Sebastian-Serrano A, Beccari L, Calcagnotto ME, Cisneros E, et al. 2010. Cux1 and Cux2 regulate dendritic branching, spine morphology, and synapses of the upper layer neurons of the cortex. *Neuron* 66: 523-35

da Silva S, Wang F. 2011. Retrograde neural circuit specification by target-derived neurotrophins and growth factors. *Curr Opin Neurobiol* 21: 61-7

Danielian PS, McMahon AP. 1996. Engrailed-1 as a target of the Wnt-1 signalling pathway in vertebrate midbrain development. *Nature* 383: 332-4

DiNardo S, Heemskerk J, Dougan S, O'Farrell PH. 1994. The making of a maggot: patterning the Drosophila embryonic epidermis. *Curr Opin Genet Dev* 4: 529-34

Dong X, Liu OW, Howell AS, Shen K. 2013. An extracellular adhesion molecule complex patterns dendritic branching and morphogenesis. *Cell* 155: 296-307

Dong X, Shen K, Bulow HE. 2015. Intrinsic and extrinsic mechanisms of dendritic morphogenesis. *Annu Rev Physiol* 77: 271-300

Dunsby C. 2008. Optically sectioned imaging by oblique plane microscopy. *Opt Express* 16: 20306-16

Eichler K, Li F, Litwin-Kumar A, Park Y, Andrade I, et al. 2017. The complete connectome of a learning and memory centre in an insect brain. *Nature* 548: 175-82

Finlayson LH, Lowenstein O. 1958. The structure and function of abdominal stretch receptors in insects. *Proc R Soc Lond B Biol Sci* 148: 433-49

Fushiki A, Zwart MF, Kohsaka H, Fetter RD, Cardona A, Nose A. 2016. A circuit mechanism for the propagation of waves of muscle contraction in Drosophila. *eLife* 5

Ghannad-Rezaie M, Wang X, Mishra B, Collins C, Chronis N. 2012. Microfluidic chips for in vivo imaging of cellular responses to neural injury in Drosophila larvae. *PLoS One* 7: e29869

Gieseler K, Graba Y, Mariol MC, Wilder EL, Martinez-Arias A, et al. 1999. Antagonist activity of DWnt-4 and wingless in the Drosophila embryonic ventral ectoderm and in heterologous Xenopus assays. *Mech Dev* 85: 123-31

Grueber WB, Jan LY, Jan YN. 2002. Tiling of the Drosophila epidermis by multidendritic sensory neurons. *Development (Cambridge, England)* 129: 2867-78

Grueber WB, Jan LY, Jan YN. 2003a. Different levels of the homeodomain protein cut regulate distinct dendrite branching patterns of Drosophila multidendritic neurons. *Cell* 112: 805-18

Grueber WB, Sagasti A. 2010. Self-avoidance and tiling: Mechanisms of dendrite and axon spacing. *Cold Spring Harbor perspectives in biology* 2: a001750

Grueber WB, Ye B, Moore AW, Jan LY, Jan YN. 2003b. Dendrites of distinct classes of Drosophila sensory neurons show different capacities for homotypic repulsion. *Current biology : CB* 13: 618-26

Grueber WB, Ye B, Yang CH, Younger S, Borden K, et al. 2007. Projections of Drosophila multidendritic neurons in the central nervous system: links with peripheral dendrite morphology. *Development (Cambridge, England)* 134: 55-64

Han C, Wang D, Soba P, Zhu S, Lin X, et al. 2012. Integrins regulate repulsion-mediated dendritic patterning of drosophila sensory neurons by restricting dendrites in a 2D space. *Neuron* 73: 64-78

Harzer H, Berger C, Conder R, Schmauss G, Knoblich JA. 2013. FACS purification of Drosophila larval neuroblasts for next-generation sequencing. *Nat Protoc* 8: 1088-99

Hattori Y, Usui T, Satoh D, Moriyama S, Shimono K, et al. 2013. Sensory-neuron subtype-specific transcriptional programs controlling dendrite morphogenesis: genome-wide analysis of Abrupt and Knot/Collier. *Dev Cell* 27: 530-44

He L, Gulyanon S, Mihovilovic Skanata M, Karagyozov D, Heckscher ES, et al. 2019. Direction Selectivity in Drosophila Proprioceptors Requires the Mechanosensory Channel Tmc. *Current biology : CB* 29: 945-56 e3

Heckscher ES, Lockery SR, Doe CQ. 2012. Characterization of Drosophila larval crawling at the level of organism, segment, and somatic body wall musculature. *The Journal of neuroscience : the official journal of the Society for Neuroscience* 32: 12460-71

Heckscher ES, Zarin AA, Faumont S, Clark MQ, Manning L, et al. 2015. Even-Skipped(+) Interneurons Are Core Components of a Sensorimotor Circuit that Maintains Left-Right Symmetric Muscle Contraction Amplitude. *Neuron* 88: 314-29

Hillman EM, Voleti V, Patel K, Li W, Yu H, et al. 2018. High-speed 3D imaging of cellular activity in the brain using axially-extended beams and light sheets. *Curr Opin Neurobiol* 50: 190-200

Hong W, Mosca TJ, Luo L. 2012. Teneurins instruct synaptic partner matching in an olfactory map. *Nature* 484: 201-7

Hughes CL, Thomas JB. 2007. A sensory feedback circuit coordinates muscle activity in Drosophila. *Mol Cell Neurosci* 35: 383-96

Hughes ME, Bortnick R, Tsubouchi A, Baumer P, Kondo M, et al. 2007. Homophilic Dscam interactions control complex dendrite morphogenesis. *Neuron* 54: 417-27

Hwang RY, Zhong L, Xu Y, Johnson T, Zhang F, et al. 2007. Nociceptive neurons protect Drosophila larvae from parasitoid wasps. *Current biology : CB* 17: 2105-16

Ibrahim DM, Biehs B, Kornberg TB, Klebes A. 2013. Microarray comparison of anterior and posterior Drosophila wing imaginal disc cells identifies novel wing genes. *G3 (Bethesda)* 3: 1353-62

Jiang N, Rasmussen JP, Clanton JA, Rosenberg MF, Luedke KP, et al. 2019. A conserved morphogenetic mechanism for epidermal ensheathment of nociceptive sensory neurites. *eLife* 8

Jinushi-Nakao S, Arvind R, Amikura R, Kinameri E, Liu AW, Moore AW. 2007. Knot/Collier and cut control different aspects of dendrite cytoskeleton and synergize to define final arbor shape. *Neuron* 56: 963-78

Kerr JN, Nimmerjahn A. 2012. Functional imaging in freely moving animals. *Curr Opin Neurobiol* 22: 45-53

Kiecker C, Lumsden A. 2005. Compartments and their boundaries in vertebrate brain development. *Nat Rev Neurosci* 6: 553-64

Kim D, Paggi JM, Park C, Bennett C, Salzberg SL. 2019. Graph-based genome alignment and genotyping with HISAT2 and HISAT-genotype. *Nat Biotechnol* 37: 907-15

Kim ME, Shrestha BR, Blazeski R, Mason CA, Grueber WB. 2012. Integrins Establish Dendrite-Substrate Relationships that Promote Dendritic Self-Avoidance and Patterning in Drosophila Sensory Neurons. *Neuron* 73: 79-91

Kohsaka H, Guertin PA, Nose A. 2017. Neural Circuits Underlying Fly Larval Locomotion. *Curr Pharm Des* 23: 1722-33

Kohsaka H, Takasu E, Morimoto T, Nose A. 2014. A group of segmental premotor interneurons regulates the speed of axial locomotion in Drosophila larvae. *Current biology : CB* 24: 2632-42

Kolodkin AL, Tessier-Lavigne M. 2011. Mechanisms and molecules of neuronal wiring: a primer. *Cold Spring Harbor perspectives in biology* 3

Kuehn ED, Meltzer S, Abraira VE, Ho CY, Ginty DD. 2019. Tiling and somatotopic alignment of mammalian low-threshold mechanoreceptors. *Proc Natl Acad Sci U S A* 116: 9168-77

Landgraf M, Jeffrey V, Fujioka M, Jaynes JB, Bate M. 2003. Embryonic origins of a motor system: motor dendrites form a myotopic map in Drosophila. *PLoS Biol* 1: E41

Lawrence PA, Struhl G. 1996. Morphogens, compartments, and pattern: lessons from drosophila? *Cell* 85: 951-61

Ledda F, Paratcha G. 2017. Mechanisms regulating dendritic arbor patterning. *Cell Mol Life Sci* 74: 4511-37

Lefebvre JL, Sanes JR, Kay JN. 2015. Development of dendritic form and function. *Annu Rev Cell Dev Biol* 31: 741-77

Lemon WC, Pulver SR, Hockendorf B, McDole K, Branson K, et al. 2015. Whole-central nervous system functional imaging in larval Drosophila. *Nat Commun* 6: 7924

Li H, Li T, Horns F, Li J, Xie Q, et al. 2020. Single-Cell Transcriptomes Reveal Diverse Regulatory Strategies for Olfactory Receptor Expression and Axon Targeting. *Current biology : CB*

Liang L, Haug JS, Seidel CW, Gibson MC. 2014. Functional genomic analysis of the periodic transcriptome in the developing Drosophila wing. *Dev Cell* 29: 112-27

Liao Y, Smyth GK, Shi W. 2014. featureCounts: an efficient general purpose program for assigning sequence reads to genomic features. *Bioinformatics* 30: 923-30

Manning L, Heckscher ES, Purice MD, Roberts J, Bennett AL, et al. 2012. A resource for manipulating gene expression and analyzing cis-regulatory modules in the Drosophila CNS. *Cell Rep* 2: 1002-13

Matsuoka RL, Nguyen-Ba-Charvet KT, Parray A, Badea TC, Chedotal A, Kolodkin AL. 2011. Transmembrane semaphorin signalling controls laminar stratification in the mammalian retina. *Nature* 470: 259-63

Matthews BJ, Grueber WB. 2011. Dscam1-mediated self-avoidance counters netrin-dependent targeting of dendrites in Drosophila. *Current biology : CB* 21: 1480-7

Matthews BJ, Kim ME, Flanagan JJ, Hattori D, Clemens JC, et al. 2007. Dendrite self-avoidance is controlled by Dscam. *Cell* 129: 593-604

Mauss A, Tripodi M, Evers JF, Landgraf M. 2009. Midline signalling systems direct the formation of a neural map by dendritic targeting in the Drosophila motor system. *PLoS Biol* 7: e1000200

Meltzer S, Yadav S, Lee J, Soba P, Younger SH, et al. 2016. Epidermis-Derived Semaphorin Promotes Dendrite Self-Avoidance by Regulating Dendrite-Substrate Adhesion in Drosophila Sensory Neurons. *Neuron* 89: 741-55

Merritt DJ, Whitington PM. 1995. Central projections of sensory neurons in the Drosophila embryo correlate with sensory modality, soma position, and proneural gene function. *The Journal of neuroscience : the official journal of the Society for Neuroscience* 15: 1755-67

Miura SK, Martins A, Zhang KX, Graveley BR, Zipursky SL. 2013. Probabilistic splicing of Dscam1 establishes identity at the level of single neurons. *Cell* 155: 1166-77

Moussian B. 2010. Recent advances in understanding mechanisms of insect cuticle differentiation. *Insect Biochem Mol Biol* 40: 363-75

O'Keefe L, Dougan ST, Gabay L, Raz E, Shilo BZ, DiNardo S. 1997. Spitz and Wingless, emanating from distinct borders, cooperate to establish cell fate across the Engrailed domain in the Drosophila epidermis. *Development (Cambridge, England)* 124: 4837-45

Ohyama T, Schneider-Mizell CM, Fetter RD, Aleman JV, Franconville R, et al. 2015. A multilevel multimodal circuit enhances action selection in Drosophila. *Nature* 520: 633-9

Orgogozo V, Grueber WB. 2005. FlyPNS, a database of the Drosophila embryonic and larval peripheral nervous system. *BMC Dev Biol* 5: 4

Parrish JZ, Xu P, Kim CC, Jan LY, Jan YN. 2009. The microRNA bantam functions in epithelial cells to regulate scaling growth of dendrite arbors in drosophila sensory neurons. *Neuron* 63: 788-802

Payre F. 2004. Genetic control of epidermis differentiation in Drosophila. *Int J Dev Biol* 48: 207-15

Pei J, Kinch LN, Grishin NV. 2018. FlyXCDB-A Resource for Drosophila Cell Surface and Secreted Proteins and Their Extracellular Domains. *J Mol Biol* 430: 3353-411

Pfeiffer BD, Jenett A, Hammonds AS, Ngo TT, Misra S, et al. 2008. Tools for neuroanatomy and neurogenetics in Drosophila. *Proc Natl Acad Sci U S A* 105: 9715-20

Poe AR, Tang L, Wang B, Li Y, Sapar ML, Han C. 2017. Dendritic space-filling requires a neuronal type-specific extracellular permissive signal in Drosophila. *Proc Natl Acad Sci U S A* 114: E8062-E71

Polleux F, Morrow T, Ghosh A. 2000. Semaphorin 3A is a chemoattractant for cortical apical dendrites. *Nature* 404: 567-73

Ponton F, Chapuis MP, Pernice M, Sword GA, Simpson SJ. 2011. Evaluation of potential reference genes for reverse transcription-qPCR studies of physiological responses in Drosophila melanogaster. *J Insect Physiol* 57: 840-50

Prochiantz A, Di Nardo AA. 2015. Homeoprotein signaling in the developing and adult nervous system. *Neuron* 85: 911-25

Proske U, Gandevia SC. 2012. The proprioceptive senses: their roles in signaling body shape, body position and movement, and muscle force. *Physiol Rev* 92: 1651-97

Pulver SR, Bayley TG, Taylor AL, Berni J, Bate M, Hedwig B. 2015. Imaging fictive locomotor patterns in larval Drosophila. *J Neurophysiol* 114: 2564-77

Qian CS. 2018. *Internal tracheal sensory neuron wiring and function in Drosophila larvae*. Columbia University

Qian CS, Kaplow M, Lee JK, Grueber WB. 2018. Diversity of Internal Sensory Neuron Axon Projection Patterns Is Controlled by the POU-Domain Protein Pdm3 in Drosophila Larvae. *The Journal of neuroscience : the official journal of the Society for Neuroscience* 38: 2081-93

Riley BB, Chiang MY, Storch EM, Heck R, Buckles GR, Lekven AC. 2004. Rhombomere boundaries are Wnt signaling centers that regulate metameric patterning in the zebrafish hindbrain. *Dev Dyn* 231: 278-91

Risse B, Berh D, Otto N, Klambt C, Jiang X. 2017. FIMTrack: An open source tracking and locomotion analysis software for small animals. *PLoS Comput Biol* 13: e1005530

Risse B, Otto N, Berh D, Jiang X, Klambt C. 2014. FIM imaging and FIMtrack: two new tools allowing high-throughput and cost effective locomotion analysis. *J Vis Exp*

Robinson MD, McCarthy DJ, Smyth GK. 2010. edgeR: a Bioconductor package for differential expression analysis of digital gene expression data. *Bioinformatics* 26: 139-40

Royer LA, Lemon WC, Chhetri RK, Wan Y, Coleman M, et al. 2016. Adaptive light-sheet microscopy for long-term, high-resolution imaging in living organisms. *Nat Biotechnol* 34: 1267-78

Salie R, Niederkofler V, Arber S. 2005. Patterning molecules; multitasking in the nervous system. *Neuron* 45: 189-92

Salinas PC, Zou Y. 2008. Wnt signaling in neural circuit assembly. *Annual review of neuroscience* 31: 339-58

Salzberg Y, Diaz-Balzac CA, Ramirez-Suarez NJ, Attreed M, Tecle E, et al. 2013. Skin-derived cues control arborization of sensory dendrites in Caenorhabditis elegans. *Cell* 155: 308-20

Sanson B. 2001. Generating patterns from fields of cells. Examples from Drosophila segmentation. *EMBO reports* 2: 1083-8

Schindelin J, Arganda-Carreras I, Frise E, Kaynig V, Longair M, et al. 2012. Fiji: an open-source platform for biological-image analysis. *Nat Methods* 9: 676-82

Schmittgen TD, Livak KJ. 2008. Analyzing real-time PCR data by the comparative C(T) method. *Nat Protoc* 3: 1101-8

Schneider-Mizell CM, Gerhard S, Longair M, Kazimiers T, Li F, et al. 2016. Quantitative neuroanatomy for connectomics in Drosophila. *eLife* 5

Schrader S, Merritt DJ. 2000. Central projections of Drosophila sensory neurons in the transition from embryo to larva. *J Comp Neurol* 425: 34-44

Schrader S, Merritt DJ. 2007. Dorsal longitudinal stretch receptor of Drosophila melanogaster larva - fine structure and maturation. *Arthropod Struct Dev* 36: 157-69

Sherrington CS. 1913. Reflex inhibition as a factor in the co-ordination of movements and postures. *Q J Exp Physiol* 6: 251-310

Singhania A. 2014. *Patterning of dendritic territories by dendrite-dendrite and dendrite-substrate interactions*. Columbia University

Singhania A, Grueber WB. 2014. Development of the embryonic and larval peripheral nervous system of Drosophila. *Wiley interdisciplinary reviews. Developmental biology* 3: 193-210

Soba P, Zhu S, Emoto K, Younger S, Yang SJ, et al. 2007. Drosophila sensory neurons require Dscam for dendritic self-avoidance and proper dendritic field organization. *Neuron* 54: 403-16

Sugimura K, Satoh D, Estes P, Crews S, Uemura T. 2004. Development of morphological diversity of dendrites in Drosophila by the BTB-zinc finger protein abrupt. *Neuron* 43: 809-22

Sun LO, Jiang Z, Rivlin-Etzion M, Hand R, Brady CM, et al. 2013. On and off retinal circuit assembly by divergent molecular mechanisms. *Science* 342: 1241974

Suslak TJ, Watson S, Thompson KJ, Shenton FC, Bewick GS, et al. 2015. Piezo Is Essential for Amiloride-Sensitive Stretch-Activated Mechanotransduction in Larval Drosophila Dorsal Bipolar Dendritic Sensory Neurons. *PLoS One* 10: e0130969

Tenenbaum CM, Misra M, Alizzi RA, Gavis ER. 2017. Enclosure of Dendrites by Epidermal Cells Restricts Branching and Permits Coordinated Development of Spatially Overlapping Sensory Neurons. *Cell Rep* 20: 3043-56

Tsubouchi A, Caldwell JC, Tracey WD. 2012. Dendritic filopodia, Ripped Pocket, NOMPC, and NMDARs contribute to the sense of touch in Drosophila larvae. *Current biology : CB* 22: 2124-34

Tuthill JC, Azim E. 2018. Proprioception. *Current biology : CB* 28: R194-R203

Vaadia RD, Li W, Voleti V, Singhania A, Hillman EMC, Grueber WB. 2019. Characterization of Proprioceptive System Dynamics in Behaving Drosophila Larvae Using High-Speed Volumetric Microscopy. *Current biology : CB* 29: 935-44.e4

Voleti V, Patel KB, Li W, Perez Campos C, Bharadwaj S, et al. 2019. Real-time volumetric microscopy of in vivo dynamics and large-scale samples with SCAPE 2.0. *Nat Methods* 16: 1054-62

Wei P, Xue W, Zhao Y, Ning G, Wang J. 2020. CRISPR-based modular assembly of a UAS-cDNA/ORF plasmid library for more than 5500 Drosophila genes conserved in humans. *Genome Res* 30: 95-106

Wizenmann A, Brunet I, Lam J, Sonnier L, Beurdeley M, et al. 2009. Extracellular Engrailed participates in the topographic guidance of retinal axons in vivo. *Neuron* 64: 355-66

Wong DC, Pearson RD, Elvin CM, Merritt DJ. 2012. Expression of the rubber-like protein, resilin, in developing and functional insect cuticle determined using a Drosophila anti-Rec 1 resilin antibody. *Dev Dyn* 241: 333-9

Wurst W, Auerbach AB, Joyner AL. 1994. Multiple developmental defects in Engrailed-1 mutant mice: an early mid-hindbrain deletion and patterning defects in forelimbs and sternum. *Development (Cambridge, England)* 120: 2065-75

Yan Z, Zhang W, He Y, Gorczyca D, Xiang Y, et al. 2013. Drosophila NOMPC is a mechanotransduction channel subunit for gentle-touch sensation. *Nature* 493: 221-5

Yang WK, Chueh YR, Cheng YJ, Siegenthaler D, Pielage J, Chien CT. 2019. Epidermis-Derived L1CAM Homolog Neuroglian Mediates Dendrite Enclosure and Blocks Heteroneuronal Dendrite Bundling. *Current biology : CB* 29: 1445-59 e3

Yasunaga K, Tezuka A, Ishikawa N, Dairyo Y, Togashi K, et al. 2015. Adult Drosophila sensory neurons specify dendritic territories independently of dendritic contacts through the Wnt5-Drl signaling pathway. *Genes Dev* 29: 1763-75

Appendix A

List of all cell surface and secreted molecule (CSS) genes [as defined by FlyXCDB resource] significantly differentially expressed in the P vs A compartment [as determined by edgeR analysis on n=3 biological replicates]. Positive fold change indicates enriched in P compartment, negative fold change indicates enriched in A compartment. Genes that overlap with P- or A-enriched genes from wing disc also noted.

CSS genes significantly enriched in the P compartment				
Gene symbol	**Gene name**	**Log2 fold change**	**Log2 counts per million (CPM)**	**Adjusted p-value (FDR)**
CG17404		6.78	1.05	0.0001
CG32302		6.71	3.76	2.4000E-22
LpR1	Lipophorin receptor 1	6.66	7.08	2.2300E-27
TwdlO	TweedleO	6.54	0.82	0.0007
prc	pericardin	5.02	9.22	3.2100E-67
CAH2	Carbonic anhydrase 2	4.87	4.13	3.4700E-19
CG1136	CG1136	4.74	2.56	4.0900E-09
CG11584	CG11584	4.58	0.75	0.0109
Osi20	Osiris 20	4.39	5.05	2.8800E-24
ppk13	pickpocket 13	4.38	4.75	9.6200E-22
TwdlN	TweedleN	4.35	2.60	2.0200E-08
mthl6	methuselah-like 6	4.33	4.37	2.3700E-18
Jon65Aiii	Jonah 65Aiii	4.30	1.20	0.0025
CG16799		3.93	3.17	1.0800E-09
Cpr66Cb	Cuticular protein 66Cb	3.91	1.57	0.0004
CG17738		3.80	2.16	1.3500E-05
Cpr65Ea	Cuticular protein 65Ea	3.72	2.89	6.7100E-08
CG15358		3.59	1.01	0.0163
CG7406		3.56	4.13	1.7200E-12
CG1368		3.52	4.12	3.1900E-12
Osi18	Osiris 18	3.48	3.10	6.7300E-08
CG5250		3.44	1.46	0.0030
Osi15	Osiris 15	3.39	6.52	7.7400E-26
CG10592		3.32	3.82	5.4900E-10
sona	sol narae	3.29	2.27	0.0001
spz5	spatzle 5	3.27	3.75	1.7300E-09
CG6753		3.18	4.80	3.1400E-13
mthl9	methuselah-like 9	2.98	7.54	9.5300E-25
CG13297		2.96	4.42	2.1600E-10
TwdlD	TweedleD	2.94	3.45	4.3600E-07
dyl	dusky-like	2.91	1.43	0.0163
TwdlM	TweedleM	2.83	1.67	0.0088
Osi9	Osiris 9	2.75	4.46	2.5500E-09
Nep1	Neprilysin 1	2.73	1.84	0.0065
CG13857		2.67	2.84	0.0001
CG4382		2.66	2.89	0.0001
CG4386		2.65	4.03	2.0300E-07
CG7695		2.64	1.67	0.0161
lambdaTry	lambdaTry	2.61	3.86	8.8100E-07
Obp56a	Odorant-binding protein 56a	2.56	9.64	3.0600E-22
CG8066		2.55	4.12	3.6200E-07
CG1986		2.52	2.80	0.0003

hh	hedgehog	2.51	7.86	7.5500E-19
Obp46a	Odorant-binding protein 46a	2.47	1.77	0.0211
Obp28a	Odorant-binding protein 28a	2.40	1.70	0.0332
CG4115		2.39	9.02	5.6700E-19
CG2962		2.38	5.78	2.7100E-11
Spn53F	Serpin 53F	2.35	1.85	0.0260
CG17290		2.33	2.82	0.0011
Tsp	Thrombospondin	2.32	5.45	8.7900E-10
Spn43Aa	Serpin 43Aa	2.23	9.77	3.2100E-17
Cpr51A	Cuticular protein 51A	2.22	4.64	8.1800E-07
C901	C901	2.19	7.41	7.1200E-14
mey	morpheyus	2.16	2.71	0.0042
CG15239		2.15	8.94	4.6800E-15
CG9411		2.12	6.64	1.6900E-11
dsd	distracted	2.10	4.49	7.5400E-06
TM4SF	Transmembrane 4 superfamily	2.09	4.52	7.1200E-06
Cad89D	Cadherin 89D	2.07	7.73	7.3300E-13
CG18641		2.06	2.49	0.0141
Osi7	Osiris 7	2.05	11.91	1.9200E-15
CG9822		2.02	2.19	0.0372
CG5756		1.98	3.55	0.0010
Ptp52F	Protein tyrosine phosphatase 52F	1.97	5.10	1.8100E-06
SPE	Spatzle-Processing Enzyme	1.96	7.38	3.3100E-11
Osi6	Osiris 6	1.93	7.77	2.3200E-11
Lip3	lipase3	1.92	3.47	0.0019
upd2	unpaired 2	1.90	4.35	0.0001
Timp	Tissue inhibitor of metalloproteases	1.85	5.73	4.7900E-07
Spn100A	Serpin 100A	1.85	9.68	8.9800E-12
dpp	decapentaplegic	1.85	6.53	1.3000E-08
CG43333		1.84	7.36	6.8900E-10
CG7173		1.81	8.20	1.7000E-10
yellow-e3	yellow-e3	1.81	8.15	2.0200E-10
dyl	dusky-like	1.80	3.12	0.0113
geko	geko	1.79	7.03	7.6800E-09
Cda4	Chitin deacetylase-like 4	1.77	6.10	3.2400E-07
CG17919		1.75	6.98	1.3000E-08
m	miniature	1.72	8.22	1.7100E-09
CG15615		1.72	3.85	0.0030
CG4914		1.71	7.04	2.8500E-08
CG12009		1.68	2.83	0.0406
CG3097		1.64	6.63	4.6200E-07
CG10469		1.61	3.19	0.0303

pyr	pyramus	1.56	8.56	4.5300E-08
TwdlF	TweedleF	1.54	4.58	0.0021
CG31823		1.52	3.56	0.0243
tfc	triforce	1.52	5.29	0.0003
obst-B	obstructor-B	1.51	7.72	4.4600E-07
verm	vermiform	1.50	6.23	2.3400E-05
Spn42Dd	Serpin 42Dd	1.49	5.28	0.0005
CG30413		1.46	7.03	4.0000E-06
CG2016		1.46	4.86	0.0022
TM4SF	Transmembrane 4 superfamily	1.45	4.41	0.0072
CG11836		1.43	3.61	0.0395
CG4096		1.41	3.60	0.0447
ect	ectodermal	1.41	10.34	3.1700E-07
slow	slowdown	1.41	4.14	0.0177
Gasp	Gasp	1.39	7.80	4.5300E-06
CG2016		1.37	6.56	0.0001
spz6	spatzle 6	1.36	9.68	1.3600E-06
Osi14	Osiris 14	1.33	5.42	0.0019
Tsp42Eg	Tetraspanin 42Eg	1.33	4.93	0.0064
mthl2	methuselah-like 2	1.30	4.28	0.0303
CG3108		1.27	6.81	0.0002
CG32750		1.26	4.23	0.0423
yellow-d	yellow-d	1.23	4.85	0.0183
Cht7	Chitinase 7	1.20	9.01	4.8600E-05
Cht5	Chitinase 5	1.20	6.73	0.0006
CG12880		1.20	4.98	0.0183
CG32473		1.19	5.83	0.0039
Tsf3	Transferrin 3	1.14	6.64	0.0016
Cys	Cystatin-like	1.14	11.48	0.0001
Osi8	Osiris 8	1.13	5.37	0.0179
yellow-e2	yellow-e2	1.11	7.57	0.0008
fj	four-jointed	1.09	8.95	0.0004
Osi24	Osiris 24	1.08	6.73	0.0031
Tsp42Ef	Tetraspanin 42Ef	1.04	7.71	0.0020
CG10005		1.03	6.28	0.0105
Fas3	Fasciclin 3	1.03	10.15	0.0006
GNBP3	Gram-negative bacteria binding protein 3	0.99	6.79	0.0091
cysu	Curly Su	0.98	9.17	0.0019
obst-A	obstructor-A	0.94	7.55	0.0086
ImpL2	Ecdysone-inducible gene L2	0.91	11.54	0.0032
CG17985		0.91	6.31	0.0374
26-29-p	26-29kD-proteinase	0.89	8.34	0.0108
Npc2a	Niemann-Pick type C-2a	0.88	7.84	0.0177
spz4	spatzle 4	0.87	6.56	0.0447

GILT1	Gamma-interferon-inducible lysosomal thiol reductase 1	0.85	11.69	0.0078
CG17672		0.85	8.66	0.0158
Tsp42El	Tetraspanin 42El	0.81	7.88	0.0348
ft	fat	0.79	11.24	0.0227
Overlap with P-enriched from wing disc microarray (Ibrahim et al. 2013)				
hh				
CG7173				
yellow-e3				
Gasp				
CSS genes significantly enriched in the A compartment				
Gene symbol	**Gene name**	**Log2 fold change**	**Log2 counts per million (CPM)**	**Adjusted p-value (FDR)**
CG31445		-7.59	1.75	1.6800E-07
kappaTry	kappaTry	-7.25	1.46	4.4300E-06
CG14120		-6.78	1.08	0.0014
CG16713		-6.38	0.80	0.0019
CG1304		-6.11	0.59	0.0082
Dscam1	Down syndrome cell adhesion molecule 1	-5.99	0.51	0.0136
DIP-iota	Dpr-interacting protein iota	-5.68	0.31	0.0449
ppk26	pickpocket 26	-5.57	2.39	3.5900E-09
CG42821		-5.49	2.33	1.0500E-08
CG4053		-5.28	1.49	0.0003
GILT3	Gamma-interferon-inducible lysosomal thiol reductase 3	-4.94	6.90	2.2300E-50
frac	faulty attraction	-4.84	2.54	9.7500E-09
CG44014		-4.79	2.15	5.5100E-07
CG10140		-4.29	0.69	0.0304
Cht10	Chitinase 3	-4.29	0.69	0.0305
stj	straightjacket	-4.24	0.73	0.0310
CG13323		-3.91	1.11	0.0092
Pdf	Pigment-dispersing factor	-3.91	2.39	2.2500E-06
Nlg1	Neuroligin 1	-3.79	1.71	0.0005
CG42255		-3.67	7.25	0.0325
Nrx-1	Neurexin 1	-3.59	3.15	3.7900E-08
CG13905		-3.58	3.29	1.1100E-08
Ir7g	Ionotropic receptor 7g	-3.54	1.73	0.0009
CG15065		-3.49	1.46	0.0041
CG6048		-3.36	1.86	0.0009
CG31760		-3.20	1.68	0.0032
CG33127		-3.09	1.58	0.0071
Con	Connectin	-3.02	8.79	0.0000
CG30280		-2.91	1.25	0.0393

apolpp	apolipophorin	-2.77	3.15	1.5100E-05
SP1029	SP1029	-2.72	3.20	2.1300E-05
Con	Connectin	-2.64	5.12	6.0000E-11
IM1	Immune induced molecule 1	-2.57	3.80	2.3000E-06
GluRIIE	Glutamate receptor IIE	-2.36	5.88	5.0100E-08
beat-IV	beaten path IV	-2.35	2.80	0.0013
CG10663		-2.30	2.19	0.0149
CG4653		-2.29	2.05	0.0225
Nlg3	Neuroligin 3	-2.28	2.43	0.0077
CG10116		-2.27	2.14	0.0177
Tsp5D	Tetraspanin 5D	-2.23	3.34	0.0003
Ir56d	Ionotropic receptor 56d	-2.18	2.13	0.0351
CG6927		-2.17	2.13	0.0303
GluRIID	Glutamate receptor IID	-2.15	6.62	9.8900E-12
CG30281		-2.10	2.05	0.0434
CG42367		-2.09	2.10	0.0431
Drl-2	Derailed 2	-2.07	6.27	5.4900E-10
Ir93a	Ionotropic receptor 93a	-2.07	4.83	2.5700E-06
CG30002		-2.05	2.55	0.0146
mspo	M-spondin	-2.03	5.07	0.0000
Dh44-R1	Diuretic hormone 44 receptor 1	-1.99	3.37	0.0019
Teh4	tipE homolog 4	-1.98	8.03	3.3200E-12
CG9593		-1.95	5.68	1.6500E-07
CG2233		-1.94	5.81	8.9100E-08
Victoria	Victoria	-1.90	3.79	0.0010
nrm	neuromusculin	-1.89	3.45	0.0031
beat-VII	beaten path VII	-1.88	4.34	0.0002
grk	gurken	-1.86	4.58	0.0001
dpr1	defective proboscis extension response 1	-1.85	3.71	0.0018
PGRP-SD	Peptidoglycan recognition protein SD	-1.85	3.01	0.0121
dpr9	defective proboscis extension response 9	-1.82	5.42	3.6500E-06
CG14529		-1.82	3.01	0.0170
stan	starry night	-1.81	4.47	0.0002
CG3556		-1.81	5.93	4.2100E-07
Dscam1	Down syndrome cell adhesion molecule 1	-1.78	8.37	2.6700E-10
Mid1	Mid1	-1.78	8.21	3.9500E-10

nAChRbeta1	nicotinic Acetylcholine Receptor beta1	-1.78	3.49	0.0060
CheA75a	Chemosensory protein A 75a	-1.75	3.29	0.0126
GABA-B-R1	metabotropic GABA-B receptor subtype 1	-1.75	5.11	3.6800E-05
CG14321		-1.75	6.99	1.4800E-08
GluRIIB	Glutamate receptor IIB	-1.75	6.36	1.9500E-07
clos	closca	-1.72	5.55	9.6500E-06
CG2736		-1.72	5.88	2.2500E-06
CG45263		-1.71	5.89	2.4700E-06
Cubn	Cubilin	-1.71	8.19	2.7800E-09
GluRIB	Glutamate receptor IB	-1.70	3.69	0.0056
Idgf5	Imaginal disc growth factor 5	-1.69	2.86	0.0396
NetB	Netrin-B	-1.69	8.81	1.1500E-09
CG1402		-1.69	5.83	4.4900E-06
Cow	Carrier of Wingless	-1.64	7.52	4.5400E-08
CG17097		-1.64	3.22	0.0275
nord	nord	-1.62	4.35	0.0020
dpr12	defective proboscis extension response 12	-1.61	4.64	0.0009
Tsp42En	Tetraspanin 42En	-1.61	3.28	0.0273
nrm	neuromusculin	-1.61	4.12	0.0041
CG30288		-1.61	3.03	0.0425
kek2	kekkon-2	-1.60	7.63	8.7800E-08
dpr4	defective proboscis extension response 4	-1.59	5.01	0.0003
amon	amontillado	-1.58	5.77	2.8500E-05
CG1773		-1.58	3.44	0.0230
GluRIIA	Glutamate receptor IIA	-1.54	6.17	1.3500E-05
Nmdar2	NMDA receptor 2	-1.54	5.55	0.0001
CG15169		-1.53	3.58	0.0249
beat-VI		-1.52	4.89	0.0011
GluRIA	Glutamate receptor IA	-1.51	4.90	0.0012
CG31675		-1.51	5.16	0.0006
CG9780		-1.50	5.10	0.0007
ppk	pickpocket	-1.50	3.93	0.0141
sca	scabrous	-1.49	5.38	0.0004
SP2353		-1.48	6.84	4.4900E-06
dpr20	defective proboscis extension response 20	-1.48	3.40	0.0440

CG43742		-1.48	4.76	0.0048
SP2353		-1.47	3.58	0.0348
ssp7	short spindle 7	-1.47	3.71	0.0279
Nrg	Neuroglian	-1.46	7.29	2.9000E-06
gogo	golden goal	-1.45	9.20	2.8300E-07
wrapper	wrapper	-1.43	9.51	3.0200E-07
CG4467		-1.40	5.87	0.0003
CG6024		-1.40	8.97	9.7300E-07
eys	eyes shut	-1.39	5.77	0.0004
CG42817		-1.38	5.48	0.0010
CG6867		-1.38	7.02	1.9200E-05
CG42613		-1.37	6.81	3.3300E-05
nAChRbeta1	nicotinic Acetylcholine Receptor beta1	-1.34	8.79	3.9100E-06
Actbeta	Activin-beta	-1.33	7.98	1.0900E-05
CG6329		-1.33	7.55	2.0300E-05
CG4306		-1.33	5.33	0.0026
CG17111		-1.33	4.34	0.0232
CG11670		-1.32	6.17	0.0003
nAChRalpha5	nicotinic Acetylcholine Receptor alpha5	-1.32	4.64	0.0134
CG11155		-1.32	5.55	0.0017
Fas2	Fasciclin 2	-1.31	9.11	5.1300E-06
smog	smog	-1.31	6.49	0.0002
Nep3	Neprilysin 3	-1.30	5.74	0.0013
CG8738		-1.29	4.31	0.0308
nAChRalpha1	nicotinic Acetylcholine Receptor alpha1	-1.29	7.00	0.0001
CG12374		-1.28	4.80	0.0137
CG14528		-1.28	4.77	0.0146
tld	tolloid	-1.27	5.38	0.0045
CG4467		-1.26	5.92	0.0014
CG6495		-1.25	7.03	0.0002
nrm	neuromusculin	-1.23	5.20	0.0099
Teh2	tipE homolog 2	-1.22	4.87	0.0194
twit	target of wit	-1.22	5.29	0.0088
CG3822		-1.21	8.20	0.0001
CG15765		-1.21	4.59	0.0351
Apoltp	Apolipoprotein lipid transfer particle	-1.19	10.09	3.6200E-05
Wnt4	Wnt oncogene analog 4	-1.18	7.16	0.0004
wg	wingless	-1.18	7.24	0.0004
Toll-6	Toll-6	-1.17	5.96	0.0036
CG6024		-1.16	5.60	0.0087
klg	klingon	-1.16	9.92	0.0001

CG7166		-1.15	6.09	0.0035
Lcch3	Ligand-gated chloride channel homolog 3	-1.15	5.56	0.0106
DIP-epsilon	Dpr-interacting protein epsilon	-1.12	6.17	0.0045
CG5597		-1.11	5.05	0.0360
Ror	Ror	-1.10	8.83	0.0003
CG7509		-1.09	5.49	0.0215
phu	phurba tashi	-1.08	5.77	0.0144
Sema2b	Semaphorin 2b	-1.08	7.50	0.0013
nAChRbeta2	nicotinic Acetylcholine Receptor beta2	-1.08	5.23	0.0374
CG13404		-1.06	5.78	0.0176
Nrk	Neurospecific receptor kinase	-1.03	9.09	0.0010
Cad88C	Cadherin 88C	-1.01	6.75	0.0073
Nrt	Neurotactin	-1.00	8.27	0.0023
fz2	frizzled 2	-0.94	8.14	0.0059
Ptp99A	Protein tyrosine phosphatase 99A	-0.94	7.09	0.0127
CG7565		-0.91	8.04	0.0094
sli	slit	-0.91	7.57	0.0127
kirre	kin of irre	-0.88	6.65	0.0364
tutl	turtle	-0.87	6.70	0.0375
Dl	Delta	-0.84	7.38	0.0324
Overlap with A-enriched from wing disc microarray (Ibrahim et al. 2013)				
SP1029				
CG9593				
Idgf5				
nord				
CG11155				